Coreless Planar Magnetic Winding Structures for Power Converters: Track-Width-Ratio

by

Samuel Robert Cove

M. Eng., Memorial University, 2011
B. Eng., Memorial University, 2009

A THESIS SUBMITTED IN PARTIAL FULFILLMENT OF
THE REQUIREMENTS FOR THE DEGREE OF

DOCTOR OF PHILOSOPHY

in

The Faculty of Graduate and Postdoctoral Studies

(Electrical & Computer Engineering)

THE UNIVERSITY OF BRITISH COLUMBIA

(Vancouver)

October 2016

Abstract

With the accelerated growth of slim consumer electronics has come the need to reduce the profile of all electronic components. Planar magnetics provide an excellent solution to this problem, where copper strip conductors and flattened planar magnetic cores allow for the height of the components to be severely decreased compared to traditional wire-wound components. Planar magnetics also provide more repeatable characteristics and easier manufacturability.

The major design goals for planar windings are low resistance, predictable inductance, and acceptable capacitance. This work investigates the application of a constant ratio between turn widths, called the Track-Width-Ratio (TWR) as a technique to attain these qualities in planar spiral windings.

This work introduces the generalized racetrack planar spiral winding, whose low-frequency analysis can be applied to a variety of common winding shapes while accommodating changing track widths. The accompanying dimensional system provides the specification of the novel winding arrangements, including predicting their inductance and resistance. A design example demonstrates an 18% increase in low-frequency performance.

The second part investigates the AC resistance from TWR. The proposed technique provides a correction factor based on the most recent models for ac resistance. A winding technique which combines hollow windings with TWR is proposed to increase the quality factor of planar spiral windings at high frequency operation. A design example highlights a change in efficiency from 70% to 90% within a 5W Wireless Power Transfer system.

Finally TWR is employed to reduce planar spiral capacitance. Through an inverse TWR winding structure, a significant decrease in capacitance is observed with a moderate reduction in resistance and inductance. A quasi-analytical approach with finite element analysis is employed to determine the winding capacitance. These windings show a 50% decrease in capacitance and a 20% decrease in resistance compared to traditional windings.

All results from this work have been confirmed experimentally and highlight the exceptional flexibility which is provided when the turn widths are included in the design of planar spiral windings.

Preface

This work is based on research performed at the Electrical and Computer Engineering department of the University of British Columbia by Samuel Robert Cove, under the supervision of Dr. Martin Ordonez. Some experimental validation work was done in collaboration with Navid Shafiei.

Chapter 1 contains modified portions of text from all below-listed publications, as well as some modified text from my master's thesis [1]:

- S. R. Cove, "Design methodology for the control of planar transformer parasitics, Masters thesis, Memorial University, 2011

Portions of chapters 2 and 3 have been published at the IEEE Energy Conversion Congress and Expo (ECCE) and IEEE Transactions on Industry Applications [2, 3]:

- S. R. Cove, M. Ordonez, "Practical inductance calculation for planar magnetics with track-width-ratio," in *Energy Conversion Congress and Exposition (ECCE)*, 2013, pp. 3733–3737.

- S. R. Cove, M. Ordonez, "Wireless-power-transfer planar spiral winding design applying track width ratio," *IEEE Trans. Ind. Appl.*, vol. 51, no. 3, pp. 2423–2433, May 2015.

A portion of chapter 3 has been published with the IEEE Transactions on Power Electronics [4]:

- S. R. Cove, M. Ordonez, N. Shafiei, J. Zhu, "Improving Wireless Power Transfer Efficiency Using Hollow Windings with Track-Width-Ratio," *IEEE Trans. Power Electron.*, vol. 31, no. 9, pp. 6524–6533, Sept. 2016.

A portion of chapter 4 has been accepted for publication at IEEE ECCE 2016 [5]:

- S. R. Cove and M. Ordonez, "Low-Capacitance Planar Spiral Windings Employing Inverse Track-Width-Ratio", accepted for publication in *IEEE Energy Conversion Congress and Expo. (ECCE)*, 2016.

As first author of the above-mentioned publications, the author of this thesis developed the theoretical concepts and wrote the manuscripts, receiving advice and technical support from Dr. Martin Ordonez, and developed simulation and experimental platforms, receiving contributions from Dr. Ordonez's research team, in particular from the Ph.D. student Navid Shafiei who developed some specific experimental tasks.

Table of Contents

List of Tables

List of Figures

Acknowledgements

I would like to sincerely thank my supervisor Dr. Martin Ordonez for accepting me as part of his research team. His support, dedication and technical advice during my program are greatly appreciated.

I would also like to acknowledge our research team, for graciously sharing their experience and knowledge with me, and for making these years a series of enjoyable experiences. Special thanks go to Navid Shafiei and Federico Luchino for developing the experimental platforms that were used to confirm the validity of this work.

I must thank the University of British Columbia and the Natural Sciences and Engineering Research Council of Canada (NSERC) for funding this research.

A special thank-you is extended to Delta-Q Technologies for their collaboration with UBC, which allowed me to further develop my research ideas while experiencing the practical side of electronics development.

Finally, it is my pleasure to be able to thank my fiancée, Deanne Drover, for her incredible patience, constant understanding, and unwavering support throughout the entirety of this process.

Chapter 1

Introduction[1]

1.1 Motivation

With the research surge in slim portable electronics and and viability of high-frequency electronic power conversion, there has been a pressing need to decrease the profile and increase the power density of magnetic components, which have traditionally been the bulkiest and heaviest components in electronic systems. Increasing research in the area has demonstrated that planar magnetic components are viable in a variety of applications, including Wireless Power Transfer (WPT), isolated power converters, resonant power converters, radio-frequency circuits, and micro-film inductors and transformers.

Planar winding layout optimization is a challenging task due to the variety of possible winding techniques and geometries which can be employed. The ideal planar spiral winding shape is application-specific and depends on the trade-off between efficiency and power density as well the physical constraints such as maximum footprint, design complexity, and manufacturability. Even the most basic planar spiral winding requires an exorbitant number

[1]Portions of this chapter have been modified from the following publications, including my master's thesis from Memorial University: [S. R. Cove, "Design methodology for the control of planar transformer parasitics, Masters thesis, Memorial University, 2011.], [S. R. Cove, M. Ordonez, F. Luchino, J. Quaicoe, "Applying Response Surface Methodology to Small Planar Transformer Winding Design," *IEEE Trans. Ind. Electron.*, vol. 60, no. 2, pp. 483–493, Feb. 2013.], [S. R. Cove, M. Ordonez, "Practical inductance calculation for planar magnetics with track-width-ratio," in *Energy Conversion Congress and Exposition (ECCE)*, 2013, pp. 3733–3737.], [S. R. Cove, M. Ordonez, "Wireless-power-transfer planar spiral winding design applying track width ratio," *IEEE Trans. Ind. Appl.*, vol. 51, no. 3, pp. 2423–2433, May 2015.], [S. R. Cove, M. Ordonez, N. Shafiei, J. Zhu, "Improving Wireless Power Transfer Efficiency Using Hollow Windings with Track-Width-Ratio," *IEEE Trans. Power Electron.*, vol. 31, no. 9, pp. 6524–6533, Sept. 2016.], and [S. R. Cove and M. Ordonez, "Low-Capacitance Planar Spiral Windings Employing Inverse Track-Width-Ratio", accepted for publication in *IEEE Energy Conversion Congress and Expo. (ECCE)*, 2016.].

of decisions before it can be manufactured. Some of the decisions that must be made, include:

- winding shape
- inner dimensions
- outer dimensions
- number of turns
- spacing between conductors
- number of layers
- conductor thickness
- conductor width

where each choice affects the spirals inductive, resistive, and capacitive behaviour. This situation is compounded with high-frequency operation where closed-form analytical solutions do not exist, or when some of the factors are not kept constant throughout each turn of the spiral, such as the conductor width.

In order to push the power density of planar magnetic technology to the limit, novel winding techniques need to be developed to reduce resistance, control inductance, and reduce winding capacitance. The final point is particularly important since it is a major drawback of planar technology when compared to wire-wound alternatives. To analyze these novel techniques and facilitate the proliferation of planar magnetic components in future electronic systems, a consolidated approach to planar spiral winding specification and analysis is required. One which can account for the majority of winding design choices and can adapt to future winding techniques and developments.

This work introduces the technique of changing track widths of each turn of planar spiral windings with a constant ratio, the Track-Width-Ratio (TWR). This technique will be proven

to be beneficial in the design of planar spiral windings in that it can decrease resistance, tune inductance, and when strategically arranged it can reduce capacitance. This work is accompanied with the introduction of the generalized racetrack planar spiral winding which is the parent winding shape to multiple of the most popular winding shape. This winding shape includes TWR and can be analyzed through the use of a proposed unified dimensional system which is flexible enough to represent circular, rectangular, octagonal, and traditional racetrack winding shapes.

1.2 Literature Review

There has been an vast amount of research into improving the performance of planar magnetic devices, and it is an extremely active topic in power electronics research today. Common research goals include the reduction of resistance, the maximization of quality factor, and the minimization of capacitance. When high-frequency excitations are considered, the most recent research in the field must rely on finite element simulation as a design tool, because the analytical models do not have any closed form solutions. In addition, each work presents their results for a limited number of winding shapes, mostly just one. Each work defines its own dimensional system, which is often a subset of a larger and more general dimensional system.

Important applications for planar magnetics include resonant and traditional power conversion [6–9], power supply on chip (PwrSoC) [10–12], and wireless power transfer [13–18]. The low profile, manufacturing repeatability, and ease of integration have established planar magnetics as a viable option to traditional wire-wound magnetics. As electronics get smaller, and frequencies increase, planar spiral windings will be the preferred choice for inductors and transformers, as they have been with radio frequency applications [19–22].

1.2.1 Planar Spiral Winding Modeling

The practical modeling of the inductance of planar spiral windings has been approached in various forms [23–34]. The fundamental theories on the self and mutual inductances of a variety of winding shapes were summarized with various experimentally-fit equations and tables [23]. Curve-fitting solutions for circular [24, 25], square [26], and rectangular [27, 28] were later developed. Greenhouse later developed a technique for rectangular spiral windings which derives from the work of Grover [29] which provided exceptional accuracy for single-layer windings. Mohan later employed curve-fitting to establish quick equations for a variety of winding shapes which was a compromise between the accuracy of Greenhouse's technique and the quickness of previous curve-fitting results [30]. When two planar windings are considered to be sandwiched between two layers of magnetic material, the self and mutual inductances were also modeled [31–34]. These exceptional advances in inductance prediction of planar spirals are extremely elegant because they employ various dimensional systems, and do not consider advanced winding design techniques such as varied track widths for each turn of the spiral.

Previous work has aimed to model the effect of high frequency winding resistance and losses in planar spirals [35–38]. A 1-D model provided an approximation for wire-wound magnetics [35], which was later improved to include edge effects with a series of 2-D models for rectangular [36] and arbitrary [37] cross section conductors. This work was later expanded to include concentric planar spiral windings by employing a model based on Finite Element Analysis [38]. These works have expanded the ability to predict the behavior of traditional planar and wire-wound windings, but the tools are not readily available to observe the effect of advanced winding techniques such as employing a variety of track widths within one winding.

This work develops models for the inductance, low-frequency resistance, and high-frequency resistance for the generalized racetrack planar spiral winding. This winding is analyzed as the

parent of the circular, rectangular, octagonal, and traditional racetrack planar spiral windings. The proposed unified dimensional system that accompanies it can include the specification of turn widths which change with a constant ratio, the Track-Width-Ratio (TWR). These models are confirmed to be accurate with the use of finite element simulations and experimental measurements. The TWR technique is confirmed to decrease inductance as it decreases from unity, while the resistance decreases to a minimum and then increases as the TWR is decreased further. An experimental design example confirms that the ratio of the inductance to the resistance, $\frac{L}{R}$ actually increases to a peak and then decreases as TWR decreases further from unity.

1.2.2 Planar Spiral Design and Track-Width-Ratio

There has been interesting research into methods in order to improve the design of planar spiral windings [39–45]. A method of improving the performance of circular planar spirals through removing the inner turns has been proposed [39, 40]. A resistance calculation method for circular and rectangular spiral windings with varying track widths has also been presented [41]. Preliminary work has been completed on characterizing parasitic effects for specific spiral geometries for interlocking-square [42] and circular [43] spiral windings for planar transformers. Track width variations have also been demonstrated to improve the Q of square integrated inductors for radio frequency (RF) applications [44, 45] for square spirals. These important contributions use various dimensioning systems, resistance models, and width-varying techniques to improve particular cases of a more general planar spiral winding structure.

These improvements to the modeling and performance of planar spiral windings is particularly important in resonant inductive Wireless Power Transfer (WPT) systems, where high-quality windings are required to optimize the power transfer. Planar spiral windings have been the choice for many recent WPT systems without any spiral optimization tech-

niques [13–18]. In these systems, the value of the inductance is important in order to design the resonant network, while the quality factor ($Q = \omega L/R$) has a significant impact on the efficiency of power transfer [46–51]. By increasing the Q factor of the inductor, lower losses can be achieved in transmission, improving the overall efficiency of the WPT system.

This work presents the hollow planar spiral winding with TWR as a technique of improving Q in planar spiral windings while allowing for a stable inductance value. An accurate high frequency resistance technique is developed and confirmed to be accurate through simulation and experimental measurements. Design of Experiments (DoE) methodology is employed to develop 3-D plots of R, L, and Q for a subset of planar spiral windings to highlight the trends for each. These models are employed to design a planar spiral winding for use in a 5 W WPT setup, for which the transfer efficiency is measured to be much higher than the traditional winding, or the case of removing internal turns.

1.2.3 Capacitance Minimization in Planar Spiral Windings

One of the documented drawbacks to planar transformer design is the additional capacitance between turns, layers, and windings [52]. The combination of large planar conductors overlapping with a high voltage differential between layers creates high capacitive energy storage in the PCB material, which can cause waveform distortion, reduction in self-resonance frequency, and high shoot-through currents in the presence of high $\frac{dV}{dt}$. Previous attempts have been made to minimize capacitance in planar magnetics [53–58]. Preliminary work has been performed on predicting capacitance in planar transformers for 2-layer coreless planar spiral windings [53] and for multi-layer planar transformers when an equal-voltage-drop model is employed between each turn [54]. Improved shielding techniques have been proposed to mitigate the impact of planar transformer capacitance [55] and a method of alternating PCB layers has shown promise for extending PCB spiral winding operating frequency [56]. Recently an approach which removes the overlapping copper from the winding window has been

proposed [57] and was later improved to include a connection to ground in the open space to reduce the capacitance and serve as an EMI filter [58].

This work presents the planar spiral winding structure with inverse TWR, which alternates between a TWR less than unity with the next layer being greater than unity to decrease the amount of overlapping copper between layers. In addition to decreasing overlapping conductors, this technique also reduces the overall voltage gradient between layers, successfully reducing the overall capacitive energy that the spiral winding can store. The voltage distribution across each turn is established and employed in finite element simulations to confirm a significant reduction in winding capacitance, with the potential to reduce low-frequency resistance. A prototype planar spiral winding is designed and its R, L, and C characteristics are compared to both the traditional planar spiral winding and the case of no overlapping conductors and the proposed technique demonstrated a similar reduction in capacitance but a significant reduction in resistance.

1.2.4 Design of Experiments Methodology

When modeling the effects of systems that either have many input factors or have highly nonlinear behaviour, it can be very beneficial to develop statistical meta-models in order to observe trends and investigate areas where optimization can occur. Design of Experiments (DoE) methodology analyzes specific datasets using a combination of hypothesis testing and ANOVA regression to identify relationships between system inputs and outputs. It has been applied to a variety of nonlinear systems where accurate and insightful models are required [59–61]. Response Surface Methodology (RSM) is a powerful technique within DoE that has been applied to the design of a C-core actuator [59], magnetic levitation systems [60], high temperature superconducting transformers [61], and planar transformer parasitics [43]. The methodology is general as it can be applied to a variety of applications and designs, and powerful as it can provide accurate results for optimization applications [62]. The existing

literature provides a basis for the use of DoE techniques to analyze the effect of nonlinear systems. This work applies RSM to eliminate the need for finite element simulations when predicting the high-frequency resistance in planar spiral windings that apply TWR, which is an applications which has not previously been investigated.

1.3 Contribution of the Work

The goal of this work is to introduce the concept of Track-Width-Ratio in the design of planar spiral windings and to prove that it can be an effective tool in improving the performance of planar spiral windings. The important contributions of the work include:

- First, the generalized racetrack planar spiral winding and the unified dimensional system are proposed as a technique for the analysis of planar spiral windings of a variety of winding shapes and designs. These concepts allow for the analysis of planar spiral windings with varied track widths for circular, rectangular, octagonal, and traditional racetrack windings, which is not currently possible with any other winding shape or dimensional system. Models for the DC resistance and inductance are derived and confirmed with finite element analysis and experimental measurements. The resistance model is derived in order to find the optimal Track-Width-Ratio (TWR) which minimizes the overall winding resistance. This technique is employed on many previously presented windings to highlight that this technique is capable of improving the performance of windings in a variety of applications. Finally, a design procedure is presented in order to design a generalized racetrack planar spiral winding for its highest performance, when the ratio of $\frac{L}{R}$ is maximized. The successful design employed a TWR of 0.85 and improved $\frac{L}{R}$ by 18%.

- Second, the concept of the hollow planar spiral winding with TWR is introduced to improve the high-frequency performance of planar spiral windings. An ac resistance

model for the proposed structure is developed based on a quasi-analytical technique previously employed for windings with equal track widths. In order to demonstrate the effectiveness of this technique, Design of Experiments (DoE) methodology is employed to develop parametric equations for a subset of winding dimensions in order to prove that for a desired inductance and footprint, the hollow planar spiral winding with TWR can greatly improve the ac quality factor of a multi-layer planar spiral winding for a high-frequency 5W WPT setup. The power transfer efficiency is measured and compared to traditional winding design, and a design with turns removed. The proposed structure improved the transfer efficiency from 70% to 90%, while the design with turns removed could only reach 80%.

- Third, a planar spiral winding structure with inverse TWR is proposed in order to reduce inter-layer capacitance. Track widths for each turn will be reduced by a constant ratio from the outside to the inside of one layer of turns, then the reverse is performed on the next layer. The amount of overlapping copper is greatly reduced, and the voltage difference between the largest overlapping areas is greatly reduced. The stored electrical energy will be investigated via Finite Element simulations, and meta-models will be developed based on the winding dimensions and layer separation. In a design example it is demonstrated that capacitance can be reduced by 50% while reducing ac resistance by upwards of 20%.

In the area of planar spiral winding characterization, this work makes great strides through the proposed generalized racetrack planar spiral winding and associated unified dimensional system through which the dc resistance and inductance are derived. The characterization is strengthened through the ac resistance which is based off a quasi-analytical model, and finally the capacitance which requires finite element simulation. With regard to the performance of planar spiral windings, the solid windings with TWR, hollow windings with TWR, and

windings with inverse TWR have proven to have particular niche uses, depending on the design criteria.

1.4 Dissertation Outline

This work is organized in the following manner:

- In Chapter 2, the generalized racetrack planar spiral winding and the unified dimensional system are proposed as a technique for the analysis of planar spiral windings of a variety of winding shapes and designs. The inductance of the structure is derived from the work of Grover and Greenhouse while the low-frequency resistance is derived from the relationship between the length to the width of each turn. These models are confirmed through finite element simulations and experimental measurements, and a design procedure is presented to illustrate how the performance at low frequency can be optimized through increasing the ratio of inductance to resistance ($\frac{L}{R}$).

- In Chapter 3, the concept of the hollow planar spiral winding with TWR is introduced to improve the high-frequency performance of planar spiral windings. The effects which cause high frequency resistance in planar spiral windings are investigated, and a model is created to predict this resistance. In order to investigate the effect of increasing the internal radius and employing TWR, high-accuracy meta-models employing Design of Experiments methodology are presented. The resultant models are employed to demonstrate that the quality factor of a planar spiral winding can be improved for a constant inductance. The proposed winding structure is employed in a 5 W, 105-200 kHz WPT setup and compared to the traditional winding case and the case of removing inner spiral turns.

- In Chapter 4, a planar spiral winding structure with inverse TWR is proposed in order to reduce inter-layer capacitance. The conditions which cause capacitance in planar spiral windings are investigated, and a model for the voltage profile of the planar spiral winding structure with inverse TWR is developed and employed to perform finite element simulations to determine spiral capacitance. The trends in capacitance and resistance are investigated with respect to changing the TWR employed in the proposed structure and an experimental prototype is compared to the case of the traditional planar spiral winding, and a winding which removes overlapping copper.

- Chapter 5 contains the relevant conclusions, contributions, and planned areas of future work. The work contributed significantly to the modeling and design of planar spiral winding, which is highlighted in eight relevant publications in international conferences or IEEE Transactions journals.

Chapter 2

Low-Frequency Resistance and Inductance Modeling of Planar Spiral Windings[2]

As discussed in the introduction, there are no tools available for a magnetics designer to specify or analyze the resistance or inductance of planar spiral windings in which the winding turn widths change with a constant ratio - the Track-Width-Ratio (TWR). The change in track widths provides a factor for which previous techniques cannot account for, and there is no literature available which can predict the performance of these windings over a variety of winding shapes.

It is the aim of this chapter to define the generalized racetrack planar spiral winding and provide the necessary tools to analyze its inductance and low-frequency resistance. The analysis is provided using a proposed unified dimensional system which can transfer the dimensions from the generalized racetrack winding to the specific cases of circular, rectangular, octagonal, and traditional racetrack windings. The analysis is applicable at DC and also any frequency at which the current density remains approximately constant over a cross-section of the conductor. While the current across a planar spiral is not 100% constant at DC, it

[2]Portions of this chapter have been published in [S. R. Cove, M. Ordonez, "Practical inductance calculation for planar magnetics with track-width-ratio," in *Energy Conversion Congress and Exposition (ECCE)*, 2013, pp. 3733–3737.] and [S. R. Cove, M. Ordonez, "Wireless-power-transfer planar spiral winding design applying track width ratio," *IEEE Trans. Ind. Appl.*, vol. 51, no. 3, pp. 2423–2433, May 2015.]

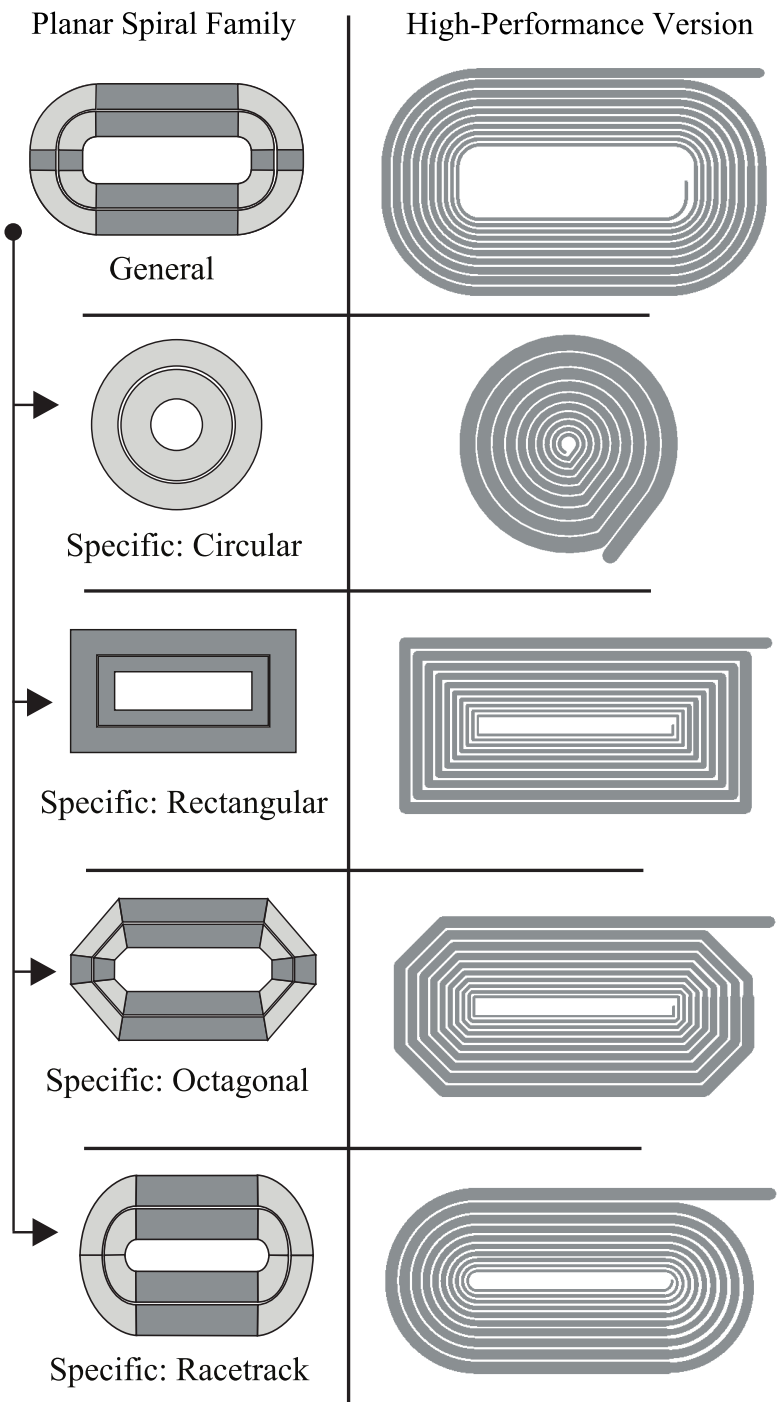

Figure 2.1: The generalized racetrack planar spiral winding and its specific subsets of windings: circular, rectangular, octagonal, and traditional racetrack along with their resultant high performance windings after applying Track-Width-Ratio.

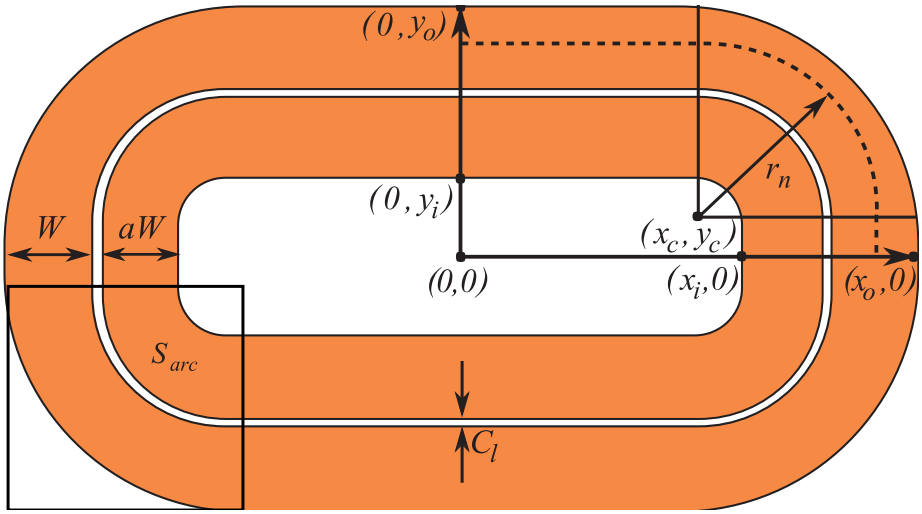

Figure 2.2: Proposed set of dimensions for a generalized racetrack planar spiral winding with a Track-Width-Ratio (TWR = a) applied.

is close enough for this analysis to provide a practical and otherwise completely accurate representation of the spiral inductance and resistance.

The resistance and inductance models are confirmed using finite element analysis and experimental validation, and then a design example is performed in which a winding shape is chosen and designed such that the maximum ratio of inductance to resistance can be attained. This ratio ($\frac{L}{R}$) is analogous to the quality factor of the winding at a frequency of 1 $\frac{rad}{s}$, which is a suitably low frequency for the models derived in this chapter. The conclusion from this example is a winding with an 18% higher $\frac{L}{R}$ value than the case with equal turn widths.

Fig. 2.1 demonstrates the generalized racetrack planar spiral winding, all of it's sub-winding shapes, and schematics for examples of high performance versions of each shape after employing TWR.

2.1 Generalized Racetrack Planar Spiral Winding

A simplified generalized racetrack structure with high accuracy is shown in Fig. 2.2 with no interconnects between turns. The generalized racetrack winding is characterized by a rectangular-shaped winding with 90° circular arcs at each corner, and a constant ratio (a) between each turn width referred to as the Track-Width-Ratio (TWR). This shape is the parent shape of many sub-winding shapes when the physical dimensions change, most notably circular (when the straight edges reduce to zero length), rectangular (when the corners contain zero radius), octagonal (when the corners are centered at an infinite distance from the corner) and the traditional racetrack spiral (when only two opposite straight edges have zero length). This shape will be analyzed employing a novel unified dimensional system in order to attain the DC inductance and resistance values. An important constraint on the shape is that it must be symmetric in both x and y axes, so meander-type windings cannot be characterized in this fashion.

2.1.1 Unified Dimensional System

As will be seen, the proposed unified dimensional system will successfully characterize the generalized racetrack winding. The dimensions, highlighted in Figs. 2.2 and 2.3, represent: the distance from the center of the spiral to the inner edge of the inner turn in the x and y directions (x_i and y_i); the distances from the center of the spiral to the outer edge of the outer turn (x_o and y_o); the distances from the center of the spiral to the center of the concentric circular arcs (x_c and y_c); the number of turns (N); the clearance distance between conductors (C_l); the thickness of the conductor (t); the corner arc shape (S_{arc} = circ for circular arcs, oct for octagonal arcs, and rect for rectangular); and the Track-Width-Ratio (a) which represents the ratio of the width of one turn to its adjacent outer turn. It is interesting to note that the dimension W, highlighted in Fig. 2.2 is defined once the winding is fully designed. Using the

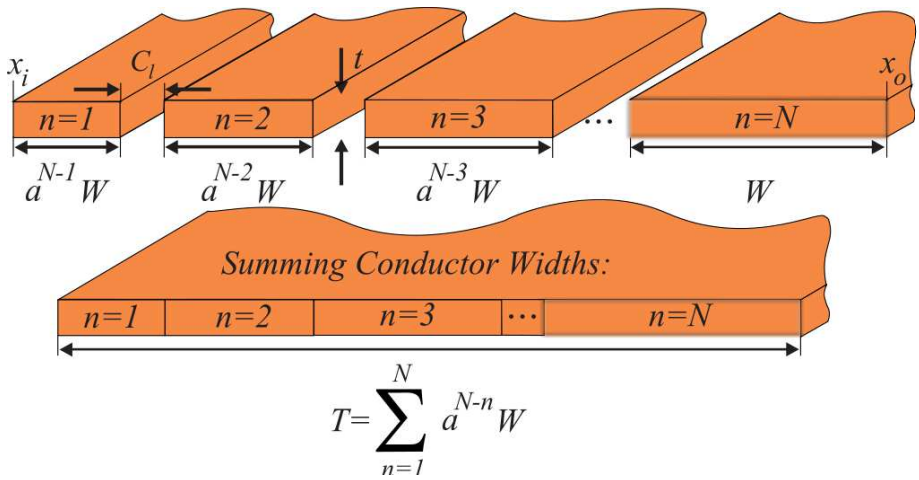

Figure 2.3: Cross-section of a generalized racetrack planar spiral winding with TWR applied. Definition of T is the total width of copper in one layer which stays the same for a given footprint and number of turns (for a constant x_i, x_o, and C_l).

required dimensions, the generalized racetrack shape can be reduced to the following specific winding shapes:

- Circular: set x_c and y_c to 0, S_{arc} = circ.
- Traditional racetrack: either x_c or y_c are 0, S_{arc} = circ.
- Rectangular: set (x_c,y_c) = (x_i,y_i), S_{arc} = rect.
- Generalized octagonal: observe Fig. 2.8 for (x_c,y_c) placement, S_{arc} = oct.

Since the winding cross section is equal in the x and y directions, $x_o - x_i$ is equal to $y_o - y_i$, so only three of the four of those dimensions are required. In this work, y_o is considered redundant. Similarly $x_i - x_c$ is equal to $y_i - y_c$ such that y_i is considered to be redundant. Therefore, the proposed dimensional system can successfully cover the general and specific geometries and will serve as the foundation for the analysis.

The TWR is the proposed method to improve performance and is indicated by the variable a in Fig. 2.2. The outer conductor will always be referred to as having a width given by W

and the inner conductor widths are given by the TWR (a) multiplied by the previous turn's width.

2.1.2 Turn Lengths and Conductor Width

The unified dimensional system provides a foundation to effectively derive physical and electrical characteristics. Most importantly, the length and width of each turn (l_n and w_n) are required for the calculation of the inductance and resistance values. The dotted line in Fig. 2.2 highlights one quarter of the length of one turn. This line is divided into three sections: one horizontal, one 90° arc, and one vertical section. In terms of the unified dimensional system, this gives:

$$l_n = 4x_c + 4y_c + 4(\frac{\pi}{2}r_n) \tag{2.1}$$

where n is defined in Fig. 2.3 as the turn number, referenced to the inner turn. The radius from (x_c,y_c) to the center of the conductor of the nth turn (r_n) is defined as:

$$r_n = x_i - x_c + (n-1)C_l + \frac{a^{N-n}}{2}W + \sum_{k=1}^{n-1} a^{N-k}W \tag{2.2}$$

The individual turn lengths can be calculated from substituting (2.2) into (2.1) under the assumption that W is known. In many situations, this is not the case, and instead the overall footprint of the winding is known (x_i,x_o,y_i, y_o, and C_l). To calculate the length without W, the total copper cross-section of the layer is defined as T, which is highlighted in Fig. 2.3 and is given by:

$$T = \sum_{n=1}^{N} a^{N-n}W = \frac{1-a^N}{1-a}W = x_o - x_i - (N-1)C_l \tag{2.3}$$

Rearranging (2.3) to solve for W and substituting into (2.2), a more applicable equation for the corner radius of the nth turn is then given by:

$$r_n = x_i - x_c + (n-1)C_l + (x_o - x_i - (N-1)C_l)\left[\frac{a^{N-n}}{2} + \sum_{k=1}^{n-1} a^{N-k}\right] \tag{2.4}$$

Substituting (2.4) into (2.1) defines the length of the nth turn of the generalized racetrack planar spiral winding in the condition where W is unknown. This is the case analyzed by this work. The individual track-widths (w_n) are defined using (2.3):

$$w_n = a^{N-n}W = (x_o - x_i - (N-1)C_l)\frac{a^{N-n}(1-a)}{1-a^N} \tag{2.5}$$

It can be concluded that the unified dimensional system for the racetrack planar spiral winding provides a strong basis for calculating winding parameters such as length and track width, which are essential for winding manufacturing and the analysis of electrical parameters such as inductance and low frequency resistance.

2.2 Inductance Modeling of the Generalized Racetrack Planar Spiral Winding

Now that the fundamental characteristics of the generalized racetrack planar spiral winding have been developed, the unified dimensional system will be employed to find equations to calculate its inductance. This will be attained by approximating the circular arcs with three specific straight planar conductors as described in Fig. 2.4, which provides an accurate representation of the self inductance of the circular corners as well as their mutual inductances with the other winding components. The lengths of the three straight conductors are determined in such a way that the overall conductor length of the corner is the same as the

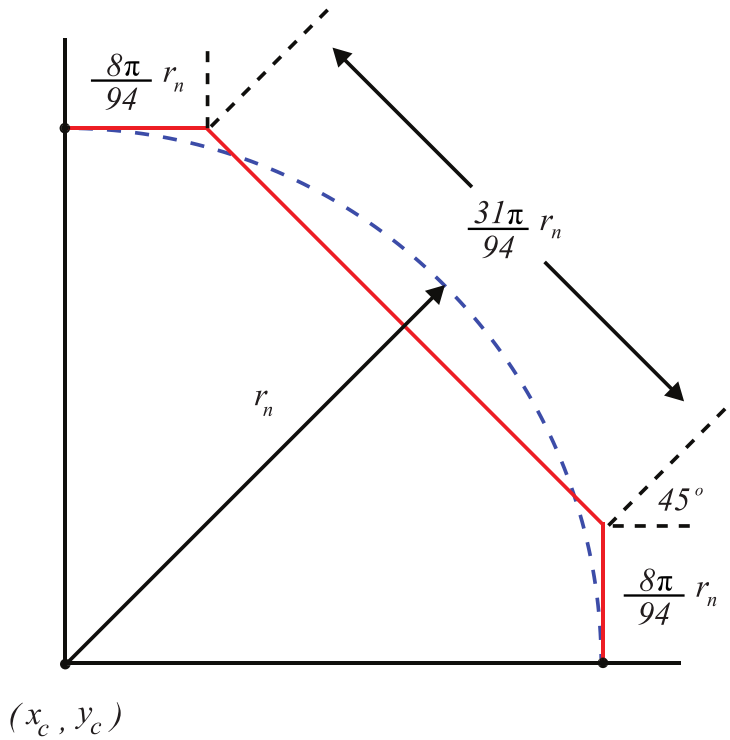

Figure 2.4: Schematic highlighting the relationship between the length of a circular racetrack corner (blue) and the radius of an octagonal approximation (red) for the nth turn of an N turn winding.

circular arc (adding to $\frac{\pi}{2}r_n$) for the nth corner of an N turn spiral as in Fig. 2.4. All self and mutual inductance calculations will consider this efficient approach.

2.2.1 Self Inductance

The self inductance (L_{s_N}) of the generalized racetrack planar spiral winding with a non-unity Track-Width-Ratio is the sum of the self inductances of all straight planar conductors of the octagonal approximated winding. Applying the unified dimensional system to Grover's self inductance formula [23], it is defined by

$$L_{s_N}(\mu H) = \sum_{n=1}^{N} 0.002 l_n \left[log_e \left(\frac{2l_n}{t + a^{N-n}W} \right) + 0.50049 + \left(\frac{t + a^{N-n}W}{3l_n} \right) \right] \tag{2.6}$$

where l_n is defined in (2.1), W is defined intrinsically within (2.3), and all dimensions are in cm. This interesting equation (2.6) shows the versatility of the generalized dimensional system to obtain self inductance.

2.2.2 Mutual Inductance

The total inductance of an N turn generalized racetrack planar spiral winding (L_{T_N}) is the addition of its self and mutual inductances (L_{s_N} and M_N):

$$L_{T_N} = L_{s_N} + M_N \tag{2.7}$$

where:

$$M_N = 2\sum_{j \neq k} M_{jk} \tag{2.8}$$

and M_{jk} is the mutual inductance between conductors j and k. Two particular cases of mutual inductance calculations are used to calculate the mutual inductances of a generalized racetrack planar spiral winding as observed in Fig. 2.5: two uneven length planar conductors oriented (a) parallel to each other with uneven width and (b) connected on one end forming a 135° angle. All other cases of mutual inductance within the generalized racetrack planar spiral winding are considered to be negligible and can be disregarded without adding significant error.

The mutual inductance of two equal-length parallel planar conductors is [29]:

$$M_l(\mu H) = 2l\left[log_e\left\{\frac{l}{GMD} + \left(1 + \frac{l^2}{GMD^2}\right)^{\frac{1}{2}}\right\} - \left(1 + \frac{GMD^2}{l^2}\right)^{\frac{1}{2}} + \frac{GMD}{l}\right] \tag{2.9}$$

where l is the length of the conductors and GMD is the geometric mean distance between the two conductors. The GMD for our case is assumed to be the distance between the centers

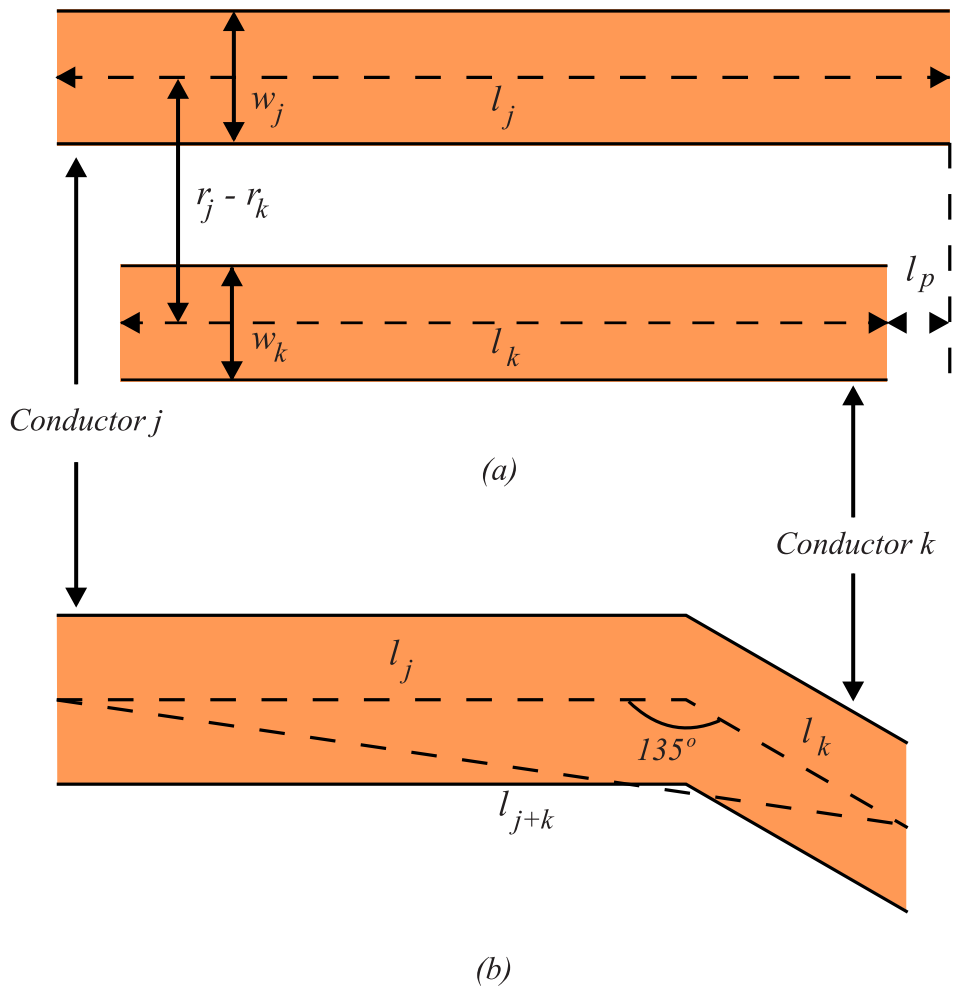

Figure 2.5: Two important cases for mutual inductance calculations with important dimensions: (a) two parallel conductors of uneven length and width centered on a vertical axis (b) two uneven length conductors of even width connected at one end subtending an angle of 135°.

of the two parallel conductors without significant error. The mutual inductance between two uneven parallel planar conductors as presented in Fig. 2.5 is given by [29]:

$$M_{jk} = M_{k+p} - M_p \tag{2.10}$$

where M_{k+p} is the mutual inductance calculated in (2.9) for $l = l_k + l_p$ and M_p is the same with $l = l_p$. Both cases use $GMD = r_j - r_k$ which is easily calculated using (2.2) given

that it is known which turn each component belongs to. Mutual inductances are positive for parallel conductors whose currents are traveling in the same direction, and are negative for conductors whose currents are traveling in opposite directions.

The mutual inductance of the case presented in Fig. 2.5 is calculated using an equation presented by Grover simplified by the fact that the angle is always 135° [23]:

$$M_{jk}(\mu H) = 0.001(\frac{\sqrt{2}}{2})l_j \left[log_e \frac{1 + \frac{l_k}{l_j} + \frac{l_{j+k}}{l_j}}{1 - \frac{l_k}{l_j} + \frac{l_{j+k}}{l_j}} + \frac{l_k}{l_j} log_e \frac{\frac{l_k}{l_j} + \frac{l_{j+k}}{l_j} + 1}{\frac{l_k}{l_j} + \frac{l_{j+k}}{l_j} - 1} \right] \tag{2.11}$$

where l_j is represented by either (2.12) or (2.13) for the case of the generalized racetrack planar spiral winding:

$$l_j = x_c + \frac{16\pi}{94} \tag{2.12}$$

$$l_j = y_c + \frac{16\pi}{94} \tag{2.13}$$

depending upon whether it is a vertical (2.12) or horizontal 2.13 conductor. Equation (2.2) is used to calculate r_n, given that the turn number (n) is known. The distance l_{j+k} is calculated using the law of cosines:

$$l_{j+k}^2 = l_j^2 + l_k^2 - \sqrt{2} l_j l_k \tag{2.14}$$

By summing up all components of the mutual inductance, M_N, in the planar spiral and combining it with the self-inductance, L_s within (2.7), the total inductance of the generalized racetrack planar spiral winding is calculated for a single layer winding. When multiple layers are involved, further analysis of the GMD is required.

2.2.3 Multiple Layer Windings

All of the preceding discussion assumed a single layer winding, but in practice a single-layer spiral winding poses problems for the return path. A much more common scenario would be a two-layer winding which spirals towards the middle, then enters an adjacent layer through vias, and spirals back to the outer turn. The self inductance of the new layer would be calculated employing (2.6), and the mutual inductance components would have to be recalculated considering the addition of the new turns. It is assumed that the inductance contribution from the via(s) is negligible compared to the total.

The new dimensions added to the unified dimensional system from the addition of further layers include the number of layers (N_L) and the distance between the centers of conductors on adjacent layers (s). The choice of using the centers of the conductors becomes clear when observing the mutual inductance calculations. Fig. 2.6 highlights the new GMDs required to be placed into (2.9) for the case of equal length conductors and (2.10) when the conductors are of unequal length. For the case of directly overlapping conductors of the same length, the mutual inductance is defined by

$$M_l(\mu H) = 2l\left[log_e\left\{\frac{l}{s} + \left(1 + \frac{l^2}{s^2}\right)^{\frac{1}{2}}\right\} - \left(1 + \frac{s^2}{l^2}\right)^{\frac{1}{2}} + \frac{s}{l}\right] \tag{2.15}$$

where s is the GMD between the conductors. When the turn components do not overlap, the GMD is represented as:

$$GMD = \sqrt{s^2 + (r_n - r_{n-i})} \tag{2.16}$$

where r_n and r_{n-i} are determined by (2.2) and i represents how many turns closer to the center the inner turn is, with respect to the outer turn being considered. This concept is represented in Fig. 2.6.

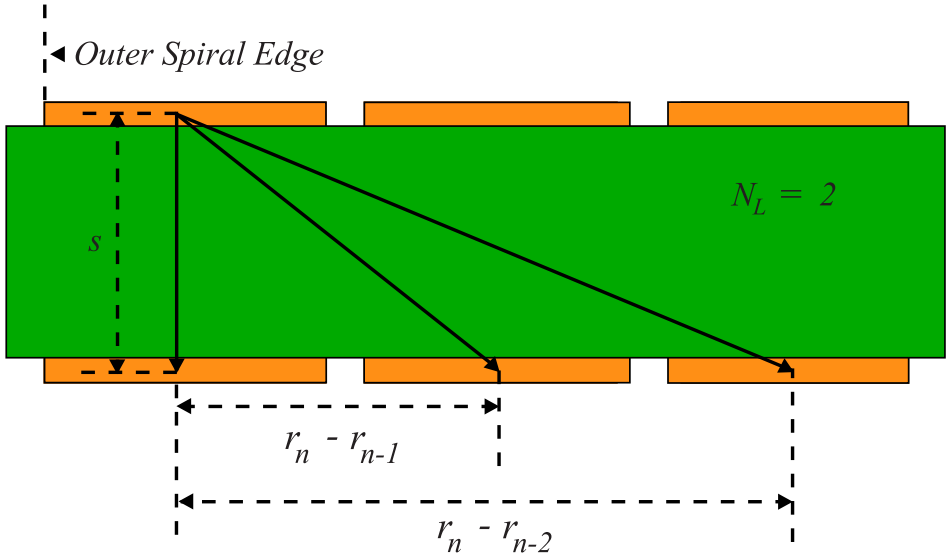

Figure 2.6: Cross-section of a multi-layer planar spiral winding, indicating the distance between layers (s), and the number of layers (N_L) for the unified dimensional system, and the distances between the centers of conductors on different layers for the mutual inductance calculations.

2.2.4 Finite Element Simulation Validation

The first step for confirming the proposed inductance modeling technique was to compare calculated data to 3D finite element simulations. To simulate L_{T_N}, the inductive energy was documented under a current excitation, I. The inductive energy (W_{ind}) within the simulation is:

$$W_{ind} = \frac{1}{4} \int_V \vec{B} \cdot \vec{H} dV \tag{2.17}$$

and this total energy is related to L_{T_N} by the relation:

$$W_{ind} = \frac{1}{2} L_{T_N} I^2 \tag{2.18}$$

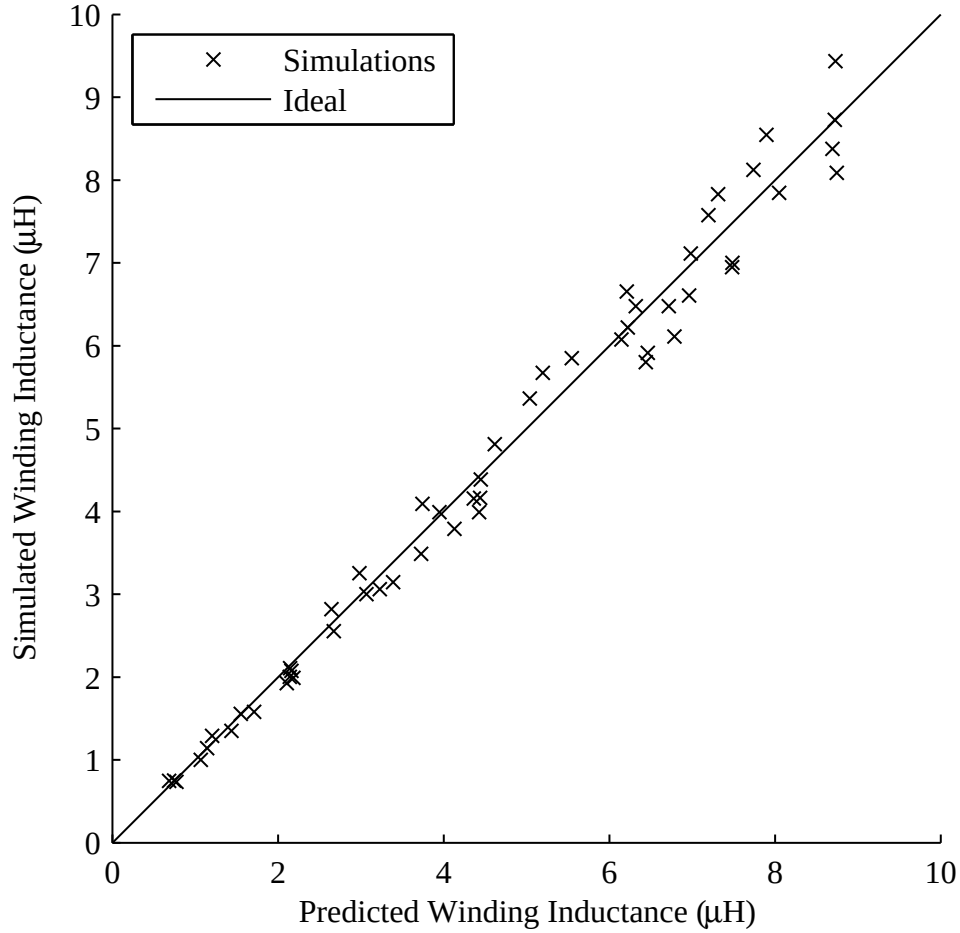

Figure 2.7: Predicted vs. simulated inductance values for 50 generalized racetrack planar spiral windings with varying dimensions, number of turns, and number of layers.

Equating (2.17) and (2.18) results in:

$$L_{T_N} = \frac{2}{I^2} \int_V \vec{B} \cdot \vec{H} dV \tag{2.19}$$

When $I^2 = 2$, the equation simplifies to:

$$L_{T_N} = \int_V \vec{B} \cdot \vec{H} dV \tag{2.20}$$

This inductance was simulated for 50 generalized racetrack planar spiral windings with

either one or two layers to confirm the technique's accuracy. The predicted and the simulated inductances were plotted against each other in Fig. 2.7, demonstrating a high accuracy for the proposed model. The discrepancies can be attributed to the approximation of the GMD between windings and the approximation of the circular corners by their octagonal equivalents.

2.3 DC Resistance Modeling of the Generalized Racetrack Planar Spiral Winding

Just as the unified dimensional system for the generalized racetrack planar spiral winding provides an effective approach to analyze its inductance, it also allows for the rapid calculation of DC resistance.

The resistance of the winding (R_N) is defined as the sum of the resistances of the individual turns:

$$R_N = \frac{\rho}{t} \sum_{n=1}^{N} \frac{l_n}{w_n} \tag{2.21}$$

where ρ represents the resistivity of the metal and t represents the metal thickness. Using the definitions of l_n and w_n defined in (2.1) and (2.5), the ratio of length to width of a single turn is:

$$\frac{l_n}{w_n} = 4\frac{(x_c + r_n(\frac{\pi}{2}) + y_c)}{a^{N-n}W} \tag{2.22}$$

where r_n is defined as in (2.2).

2.3.1 General Resistance Formula

Expanding (2.22) considering (2.3) and simplifying, the general form of the resistance of the generalized racetrack planar spiral winding is:

$$R_N = \frac{4\rho}{tT}\left[NR_{N_0} + \sum_{n=1}^{N-1}\left(R_{N_-}a^{n-N} + R_{N_+}a^{N-n}\right)\right] \tag{2.23}$$

where R_{N_-}, R_{N_+}, and R_{N_0} indicate the components of the metal resistance of an N-turn generalized racetrack spiral with negative, positive, and zero powers of a, respectively, where:

$$R_{N_-} \neq R_{N_+} \neq R_{N_0} \tag{2.24}$$

This general form of the metal resistance highlights its polynomial nature, containing powers of TWR (a) ranging from $-(N-1)$ to $N-1$. After applying (2.3) the resistance components are given by:

$$R_{N_0} = \left(1 - \frac{\pi}{2}\right)x_c + y_c + \frac{\pi}{2}\left(\frac{x_i + x_o}{2}\right) \tag{2.25}$$

$$R_{N_-} = n\left(\left(1 - \frac{\pi}{2}\right)x_c + y_c + \frac{\pi}{2}\left(x_i + \frac{(n-1)}{2}C_l\right)\right) \tag{2.26}$$

$$R_{N_+} = n\left(\left(1 - \frac{\pi}{2}\right)x_c + y_c + \frac{\pi}{2}\left(x_o + (2-n)C_l\right)\right) \tag{2.27}$$

Equations (2.23) and (2.25-2.27) are exact solutions of winding resistance and can be easily implemented in a spreadsheet or technical computing software for a target footprint and number of turns. In the end, the solution is a polynomial of TWR (a) so even the most simple of calculating methods can be used to model the resistance of the resulting spiral. It is important to note that this model is accurate in the absence of skin and proximity effects.

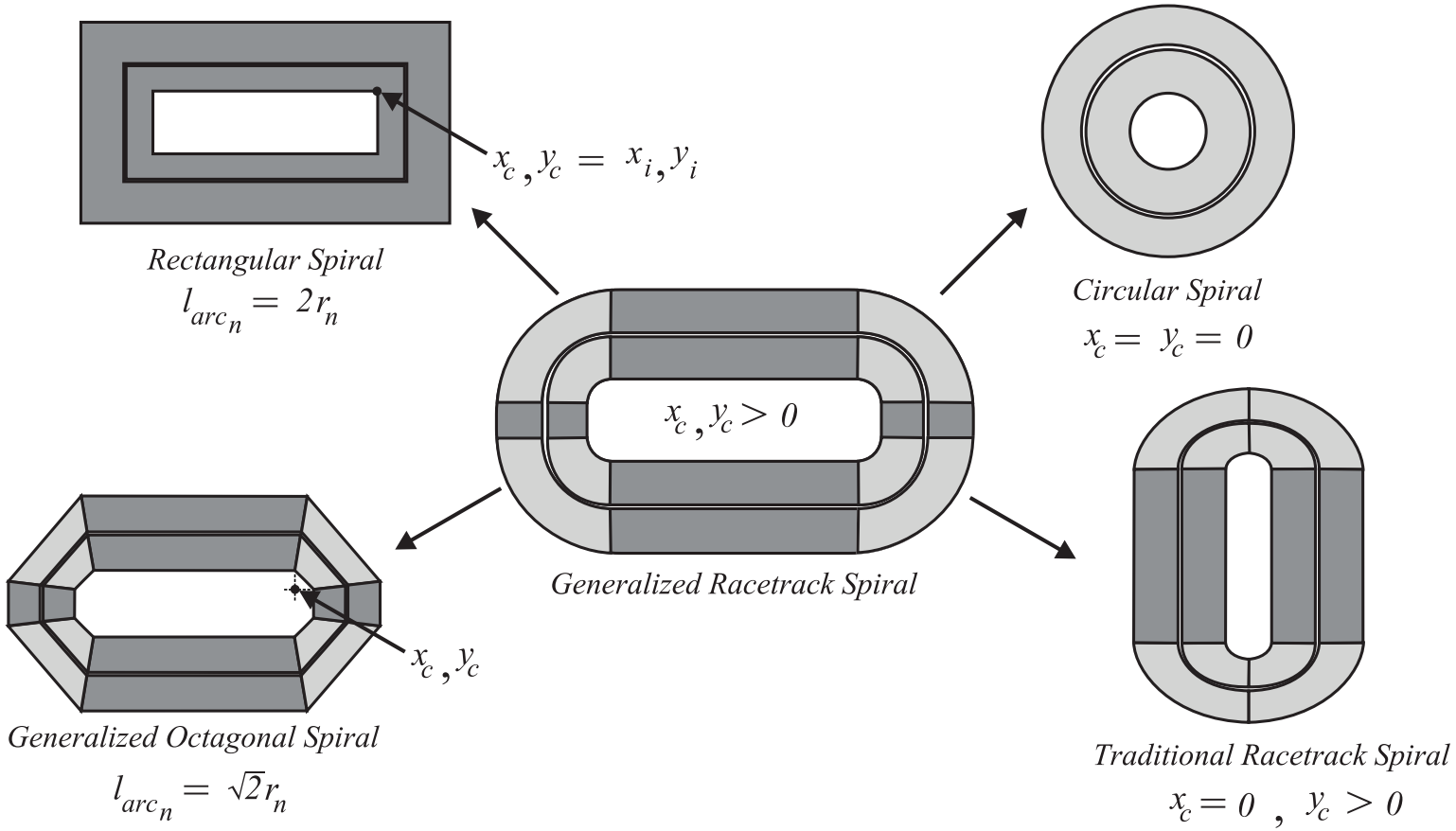

Figure 2.8: Mapping from the generalized racetrack planar spiral winding to each of the specific cases: circular, rectangular, generalized octagonal, and traditional planar spiral windings.

2.3.2 Resistance Coefficients for Special Cases

Table 2.1: Summary of Resistance Model Coefficients

Spiral	Term	Model
Generalized Racetrack	R_{N_0}	$\left(1-\frac{\pi}{2}\right)x_c + y_c + \frac{\pi}{2}\left(\frac{x_i+x_o}{2}\right)$
	R_{N_-}	$n\left(\left(1-\frac{\pi}{2}\right)x_c + y_c + \frac{\pi}{2}\left(x_i + \frac{(n-1)}{2}C_l\right)\right)$
	R_{N_+}	$n\left(\left(1-\frac{\pi}{2}\right)x_c + y_c + \frac{\pi}{2}\left(x_o + (2-n)C_l\right)\right)$
Circular	$R_{N_0(circ)}$	$\frac{\pi}{4}(x_i + x_o)$
	$R_{N_-(circ)}$	$\frac{n\pi}{2}\left(x_i + \frac{(n-1)}{2}C_l\right)$
	$R_{N_+(circ)}$	$\frac{n\pi}{2}\left(x_o + (2-n)\,C_l\right)$
Rectangular	$R_{N_0(rect)}$	$y_i + x_o$
	$R_{N_-(rect)}$	$n\left(x_i + y_i + (n-1)C_l\right)$
	$R_{N_+(rect)}$	$n\left(-x_i + y_i + 2x_o + (1-n)C_l\right)$
Generalized Octagonal	$R_{N_0(oct)}$	$\left(1-\frac{\pi}{4}\right)x_i + y_i + \frac{\pi}{4}x_o - d\left(2-\frac{\pi}{2}\right)\left(\frac{\sqrt{2}}{2}+\frac{8}{31}\right)$
	$R_{N_-(oct)}$	$n\left(x_i + y_i + \frac{\pi}{4}(n-1)\,C_l - d\left(2-\frac{\pi}{2}\right)\left(\frac{\sqrt{2}}{2}+\frac{8}{31}\right)\right)$
	$R_{N_+(oct)}$	$n\left(\left(1-\frac{\pi}{2}\right)x_i + y_i + \frac{\pi}{2}\left(x_o + (2-n)C_l\right) - d\left(2-\frac{\pi}{2}\right)\left(\frac{\sqrt{2}}{2}+\frac{8}{31}\right)\right)$
Traditional Racetrack	$R_{N_0(RT)}$	$\left(1-\frac{\pi}{2}\right)x_c + \frac{\pi}{2}\left(\frac{x_i+x_o}{2}\right)$
	$R_{N_-(RT)}$	$n\left(\left(1-\frac{\pi}{2}\right)x_c + \frac{\pi}{2}\left(x_i + \frac{(n-1)}{2}C_l\right)\right)$
	$R_{N_+(RT)}$	$n\left(\left(1-\frac{\pi}{2}\right)x_c + \frac{\pi}{2}\left(x_o + (2-n)C_l\right)\right)$

The previous derivation of winding resistance is universal to the generalized racetrack planar spiral winding. The winding is also simplified to the specific cases of circular, rectangular, and octagonal winding shapes as indicated in Fig. 2.8. The specific resistance coefficients were successfully extracted and are presented in Table 2.1. A pattern resulted, and each

resistance coefficient could be represented by one general form:

$$R_{N_0} = (1-k)\,x_c + y_c + k\left(\frac{x_i + x_o}{2}\right) \tag{2.28}$$

$$R_{N_-} = n\left((1-k)\,x_c + y_c + k\left(x_i + \frac{(n-1)}{2}C_l\right)\right) \tag{2.29}$$

$$R_{N_+} = n\left((1-k)\,x_c + y_c + k\left(x_o + (2-n)C_l\right)\right) \tag{2.30}$$

where k is a winding shape coefficient which is equal to $\frac{\pi}{2}$ for circular corner shapes (generalized and traditional racetrack, circular), 2 for rectangular, and $\sqrt{2}$ for generalized octagonal planar spiral windings.

2.3.3 Optimal Track-Width-Ratio

The general method of finding the minimum of any function is applied to find the model for the optimal TWR for a given footprint and number of turns. The derivative of the resistance formula with respect to the TWR is found and set equal to zero:

$$\frac{\partial R_N}{\partial a} = 0 \tag{2.31}$$

Considering the model of the resistance is a polynomial of a, the power rule is applied, in conjunction with the fact that the derivative of a sum of functions is the sum of the functions' derivatives, and the resultant equation for the optimal TWR (a_{opt}) for a pre-determined footprint and number of terms is:

$$0 = \sum_{n=1}^{N-1}\left((n-N)R_{N_-}a_{opt}^{n-N-1} + (N-n)R_{N_+}a_{opt}^{N-n-1}\right) \tag{2.32}$$

Multiplying both sides of the equation by a_{opt} will eliminate the newly added factors of a_{opt}^{-1} introduced by the derivative, leaving:

$$0 = \sum_{n=1}^{N-1} \left((n-N) R_{N_-} a_{opt}^{n-N} + (N-n) R_{N_+} a_{opt}^{N-n} \right) \tag{2.33}$$

Many methods are available to solve the roots of polynomials, such as the secant method or Newton's method. Many calculators and technical computing software contain built-in functions for solving such problems. This is a very quick and effective method of determining the optimal TWR to apply to a given planar spiral inductor geometry. Substituting the solution of (2.33) into (2.23) results in the theoretical minimum resistance.

2.3.4 Finite Element Simulation Validation

In order to determine the accuracy of the proposed resistance model, a variety of planar spiral windings were simulated using finite element analysis and their resistance extracted for comparison. To determine the resistance of the spiral, the ohmic loss energy (W_Ω) was simulated using the relation:

$$W_\Omega = \frac{1}{2\sigma} \int_V \vec{J} \cdot \vec{J} dV \tag{2.34}$$

which is equivalent to the ohmic loss in a lumped sum resistor, given by:

$$W_\Omega = I^2 R_N \tag{2.35}$$

Equating (2.34) and (2.35) results in:

$$R_N = \frac{1}{2} \int_V \vec{J} \cdot \vec{J} dV \tag{2.36}$$

A selection of spirals were simulated using 3D finite element analysis and compared to

the predicted resistance at $a = 1$ and $a = a_{opt}$ values. The dimensions of the windings were converted from a number of specific systems into the proposed unified dimensional system, which provides a simple method to compare all of the specific cases of windings. Table 2.2 summarizes the results which emphasize the benefits of applying TWR to planar spirals for a variety of shapes and sizes. References have been included for any windings that were extracted from other published work. It can be observed from the results that the simulated resistances match closely with the calculated values using (2.23) for a variety of footprints and number of turns. It is also critical to note that applying TWR to the planar spirals decreased resistance significantly, even on top of the improvements provided by each cited work. Both the resistance model and the TWR technique provide valuable tools for design of planar spiral windings.

Table 2.2: Dimensional Model and Optimized Resistances: Simulation vs. Calculation

Source	Spiral Family	Unified Dimensional System (Proposed in this work)	Traditional		Optimized		
			R_{sim}	R_{calc}	a_{opt}	$R_{sim}\|_{a=a_{opt}}$	$R_{calc}\|_{a=a_{opt}}$
	Generalized Racetrack	$x_i = 7.5$mm , $x_o = 17.5$mm $y_i = 4$mm , $C_l = 0.25$mm $x_c = 6.25$mm , $y_c = 2.75$mm $N = 2$, $t = 35\mu$m	14.6mΩ	14.5mΩ	0.635	13.4mΩ	13.3mΩ
[56]	Circular	$x_i = 8.9$mm , $x_o = 21.4$mm $y_i = 8.9$mm , $C_l = 0.3$mm $x_c = 0$, $y_c = 0$ $N = 8$, $t = 70\mu$m	14.6mΩ	14.9mΩ	0.905	13.3mΩ	13.5mΩ
[63]	Rectangular	$x_i = 7.5$, $x_o = 17.5$ $y_i = 4$mm , $C_l = 1.04$mm $x_c = N/A$, $y_c = N/A$ $N = 6$, $t = 70\mu$m	157mΩ	157mΩ	0.88	149mΩ	149mΩ
[64]	Square	$x_i = 2.4$mm , $x_o = 7.5$mm $y_i = 2.4$mm , $C_l = 0.15$mm $x_c = N/A$, $y_c = N/A$ $N = 7$, $t = 10\mu$m	779mΩ	783mΩ	0.86	720mΩ	723mΩ
[19]	Octagonal	$x_i = 37.5\mu$m , $x_o = 83.5\mu$m $y_i = 37.5\mu$m , $C_l = 2\mu$m $x_c = 0$, $y_c = 0$ $N = 4$, $t = 0.35\mu$m	7.84Ω	7.80Ω	0.833	7.55Ω	7.49Ω
[10]	Traditional Racetrack	$x_i = 1.465$mm , $x_o = 2.065$mm $y_i = 315\mu$m , $C_l = 50\mu$m $x_c = 1.15$mm , $y_c = 0$ $N = 5$, $t = 50\mu$m	182mΩ	180mΩ	0.92	177mΩ	176mΩ

2.4 Experimental Results

Multiple panels of planar spiral windings with various shapes and sizes were manufactured in order to test the accuracy of the developed models with the final objective of obtaining a high ratio of inductance to resistance. Several of these windings are included in Fig. 2.9, reflecting the change of trace width resulting from modifying TWR and the number of turns. Every winding contained the same internal and external dimensions, just the distribution of that copper changed as the TWR was changed. The unified dimensional system representation of the windings is:

- x_c, y_c = 2 mm, 13.5 mm
- x_i = 4.5 mm
- x_o = 14.5 mm
- t = 35 μm
- C_l = 254 μm
- S_{arc} = circ
- N = 2, 4, 6, 8, 10
- a = 0.2 - 1.0
- N_L = 2
- s = 0.5 mm

Recall that TWR (Fig. 2.3) defines how much the inner trace widths are reduced as the winding approaches the center. The inductance and dc resistance of all of the windings was

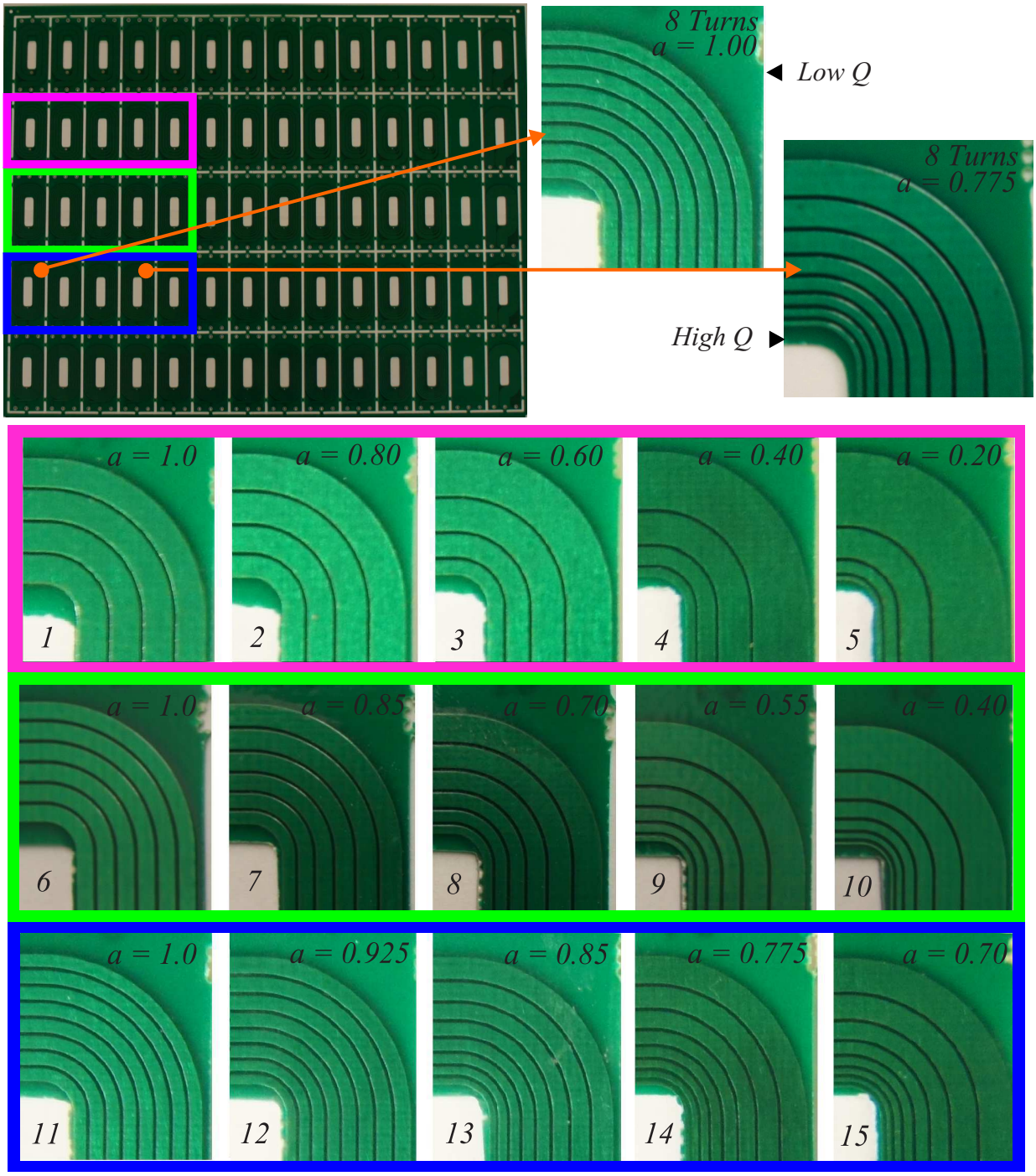

Figure 2.9: Example of manufactured generalized racetrack planar spiral windings with various turns and Track-Width-Ratios applied. The windings in the colored boxes represent the 4, 6, and 8-turn windings from Fig. 2.10, respectively.

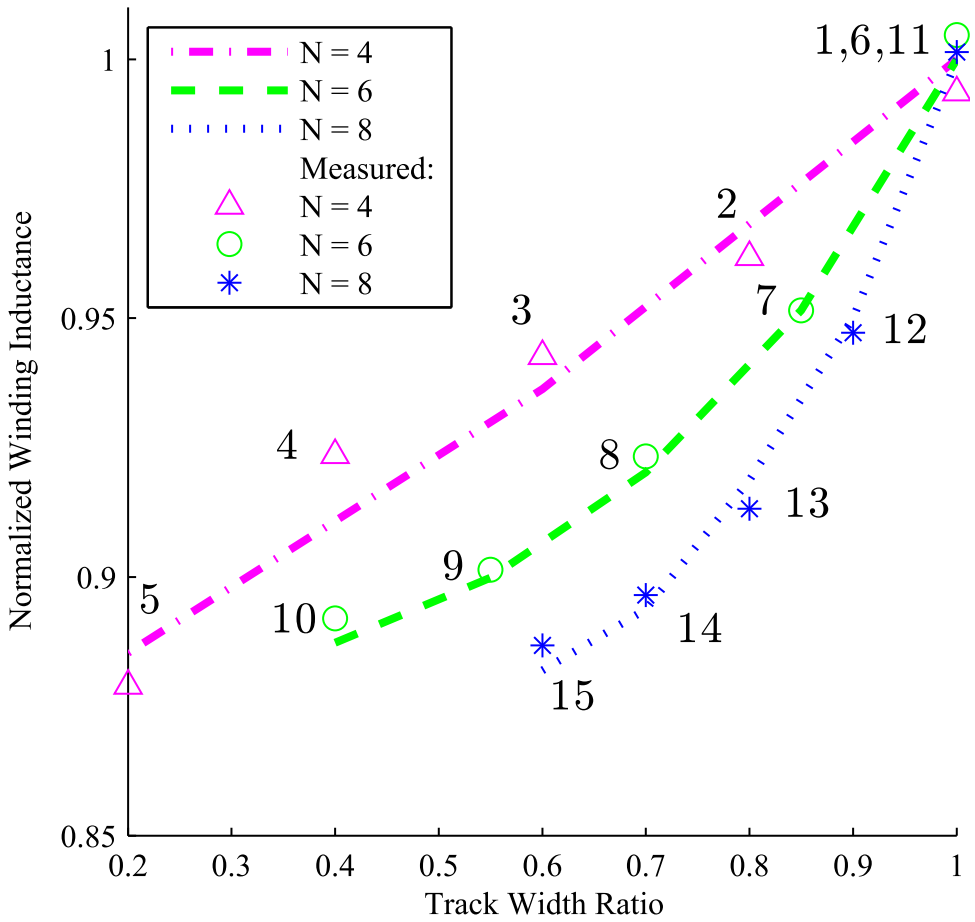

Figure 2.10: Experimental validation of inductance prediction method for generalized race-track planar spiral windings. Inductance values for 4, 6, and 8 turns per layer normalized to 567 nH, 1.27 μH, and 2.51 μH respectively. The experimental data points are numbered in correlation with their winding design highlighted in Fig. 2.9.

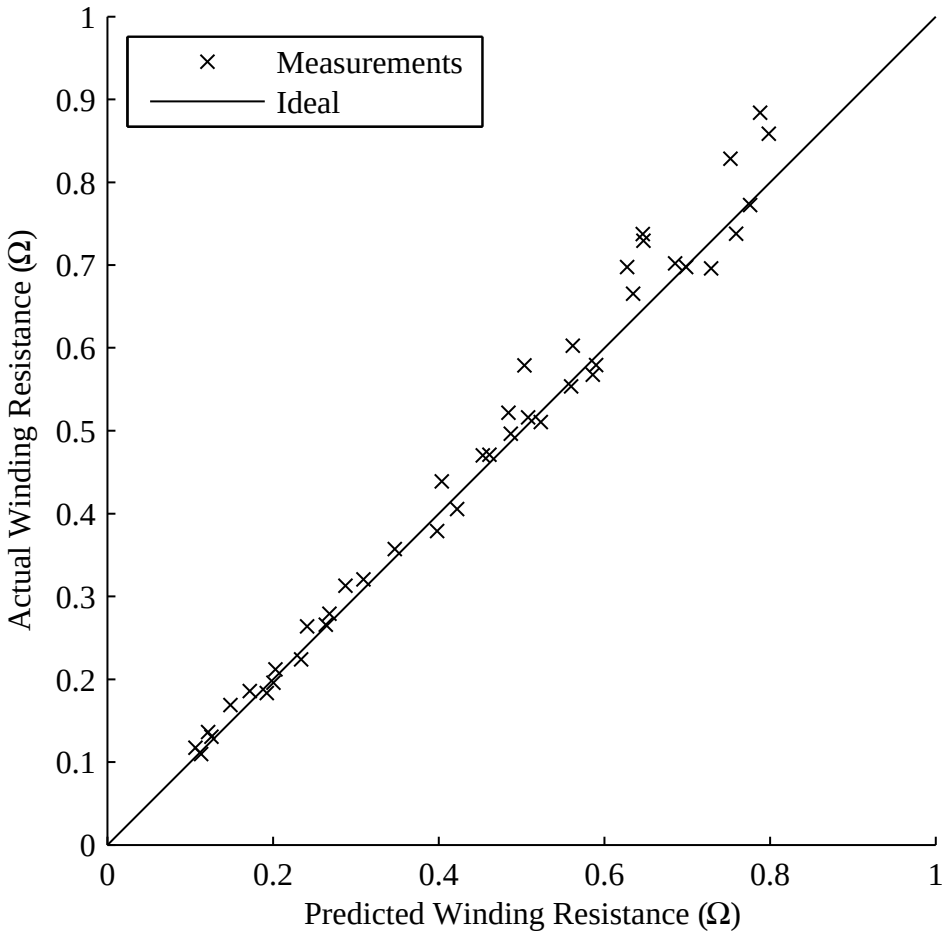

Figure 2.11: Experimental validation of DC resistance prediction method for a variety of planar spiral shapes and sizes. Sizes range from $x_i = 1$ to 15 mm, $x_o = 5$ to 30 mm, and $N = 2$ to 10, and $S_{arc} = circ$, $rect$, and oct. Exceptional accuracy is attained over a variety of windings shapes, sizes, and Track-Width-Ratio.

measured using a frequency response analyzer and their $\frac{L}{R}$ ratios were calculated. By using the equations obtained in this work, Fig. 2.10 presents the resulting predictions with dashed lines. As well, the experimental measurements are presented in Fig. 2.10 to compare predicted versus estimated. Each curve is normalized to the inductance at unity TWR ($a = 1$) such that an even comparison can be made. The generality and accuracy of the DC resistance calculation method is emphasized in Fig. 2.11. The resistance was calculated for over 100 planar spiral windings and compared to measured values for racetrack, circular, rectangular, and octagonal spiral windings with various footprints and number of turns. The line for which the expected and measured values are exactly the same has been included on the plot in order to highlight the significant accuracy of the proposed DC resistance calculation method. Finally, the objective of obtaining a high ratio of L to R is fulfilled in Fig. 2.12, which presents the comparison of the predicted to the experimentally measured. The figure includes a subset of generalized racetrack planar spiral windings. By inspection, the best TWR for N=4,6,8 to improve $\frac{L}{R}$ is obtained. Lower number of turns (e.g., N=4) require a lower TWR to obtain the highest performance, thus departing significantly from the traditional winding with TWR = 1.

2.4.1 Magnetic Substrate

These inductive and resistive models contain no magnetic material. A preliminary investigation into the effect of a magnetic substrate with a relative permeability of 1000 was performed to observe the effect. FEA simulations were used to observe the change in inductance for the windings measured in Fig. 2.10 with an infinite magnetic substrate placed below the winding. As was discussed in [32], in each case the inductance increased by a factor of two, but continued with the same normalized curves represented in Fig. 2.10. This is a very interesting result, as the prediction models from this work can be used to predict the inductance with a magnetic substrate through a simple multiplicative factor. As expected from [32], this

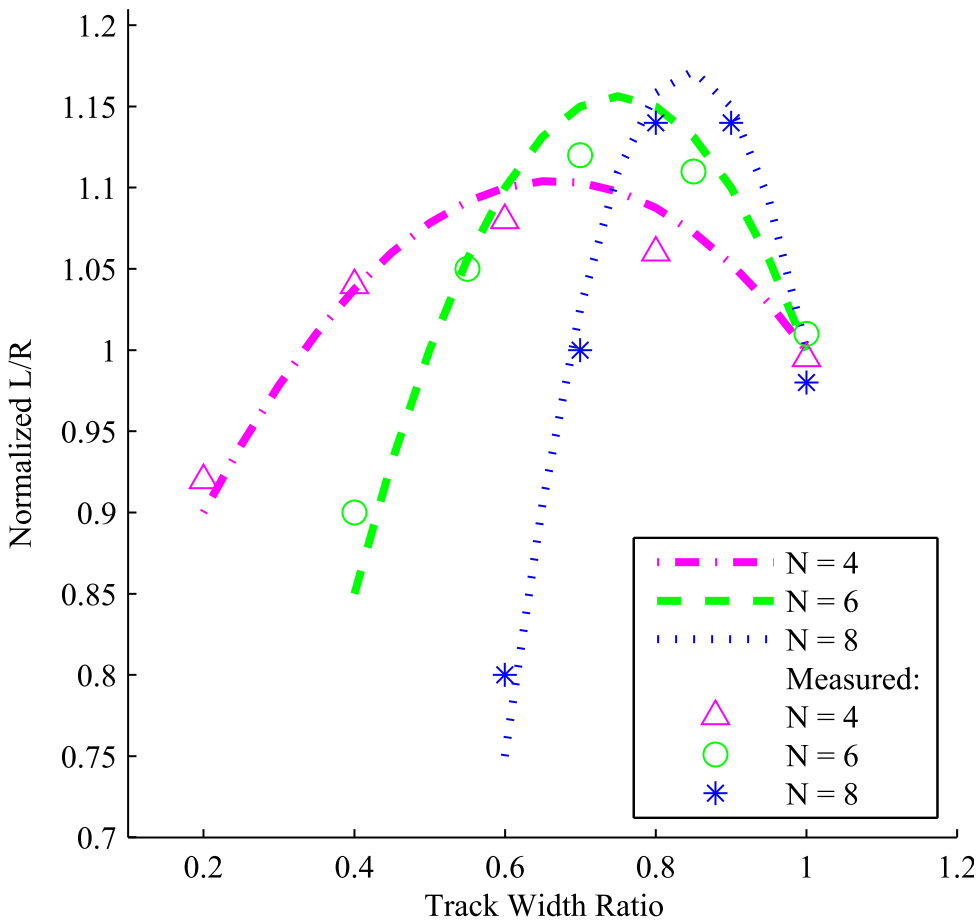

Figure 2.12: Normalized figure of merit ($\frac{L}{R}$) trends and experimental validation for generalized racetrack planar spiral windings from Fig. 2.9.

factor changes with the permeability of the material as well as the thickness of the material. This multiplier changes greatly when sandwiched between two infinite planes of magnetic material.

2.4.2 Design Example: Low Frequency Planar Spiral Winding

In this section the previously presented models for inductance and resistance are employed in order to improve the $\frac{L}{R}$ for a circular planar spiral winding. Low-frequency refers to a

Table 2.3: Design Winding Specifications

Parameter	Value
x_o	15 mm
x_i	1 mm
Shape	Circle
N	10
C_l	0.25 mm
t	35 μm
ρ_{cu}	1.68×10^{-8} Ωm
a	TBD

frequency at least two orders of magnitude below that which would exhibit the skin effect in a planar conductor of a particular width. It is important that the current density does not change due to skin or proximity effect. The specifications of the baseline winding are included in Table 2.3. The experimental planar PCB is shown in Fig. 2.13. In order to predict the inductance and resistance, and thus determine the TWR which will improve $\frac{L}{R}$ the most, the following procedure was followed:

1. Apply the dimensions from Table 2.3 in (2.2) such that it is only a factor of a and n. In this case

$$r_n = 0.75 + 0.25n + 11.75\left[\frac{a^{10-n}}{2} + \sum_{k=1}^{n-1} a^{10-k}\right] \tag{2.37}$$

2. Substitute (2.37) into (2.1) to determine each turn's length as a factor of n. In this case

$$l_n = 2\pi r_n \tag{2.38}$$

   As an example, for the equal-turn-width case ($a = 1$), the turn lengths range from 9.96 mm for the inner turn up to 90.6 mm for the 10th turn.

3. Apply the unified winding dimensions and the results from (2.38) within (2.6) to cal-

culate the self inductance of the windings. In this case

$$L_s(\mu H) = \sum_{n=1}^{10} 0.002 l_n \left[log_e \left(\frac{2l_n}{0.035 + a^{10-n}W} \right) + 0.50049 + \left(\frac{0.035 + a^{10-n}W}{3l_n} \right) \right] \tag{2.39}$$

where

$$W = 11.75 \frac{1-a}{1-a^{10}} \tag{2.40}$$

the only variable which remains to solve this equation is a, the TWR.

4. Calculate the lengths of each straight trace section of the octagonal approximate winding. The horizontal component lengths are calculated applying (2.12), the vertical component lengths are calculated applying (2.13), and the diagonal corner lengths are determined from the expression in Fig. 2.4:

$$l_j = \frac{31\pi}{94} r_n \tag{2.41}$$

where the radius of each turn, r_n, was tallied in step 1. The final length that must be calculated is l_{j+k} from (2.14).

5. Calculate the mutual inductances using (2.8)-(2.11)

6. Apply the method of Greenhouse to calculate the final inductance of the winding. A simple script to change the TWR of the design and recalculate the inductances was used to determine the inductance trends presented in Fig. 2.13

7. Calculate the resistance coefficients by substituting the dimensions into (2.25) - (2.27).

In this case:

$$R_{N_0} = 4\pi \tag{2.42}$$

$$R_{N_-} = \frac{\pi n}{2}\left(1 + \frac{(n-1)}{8}\right) \tag{2.43}$$

$$R_{N_+} = \frac{\pi n}{2}\left(15.5 - \frac{n}{4}\right) \tag{2.44}$$

8. Calculate T from (2.3):

$$T = 15 - 1 - 9 * 0.25 = 11.75mm \tag{2.45}$$

9. Substitute (2.42) - (2.45) into (2.23) to determine the resistance as a function of a:

$$R_N = \frac{3200\rho}{329}\left[40\pi + \sum_{n=1}^{9}\left(\frac{\pi n}{2}\left(1 + \frac{(n-1)}{8}\right)a^{n-10} + \frac{\pi n}{2}\left(15.5 - \frac{n}{4}\right)a^{10-n}\right)\right] \tag{2.46}$$

10. Now all models of L_N and R_N for the winding only contain a as a factor. Technical computing software such as Microsoft Excel or MATLAB can be employed to plot L_N, R_N, and $\frac{L_N}{R_N}$ for a wide range of a.

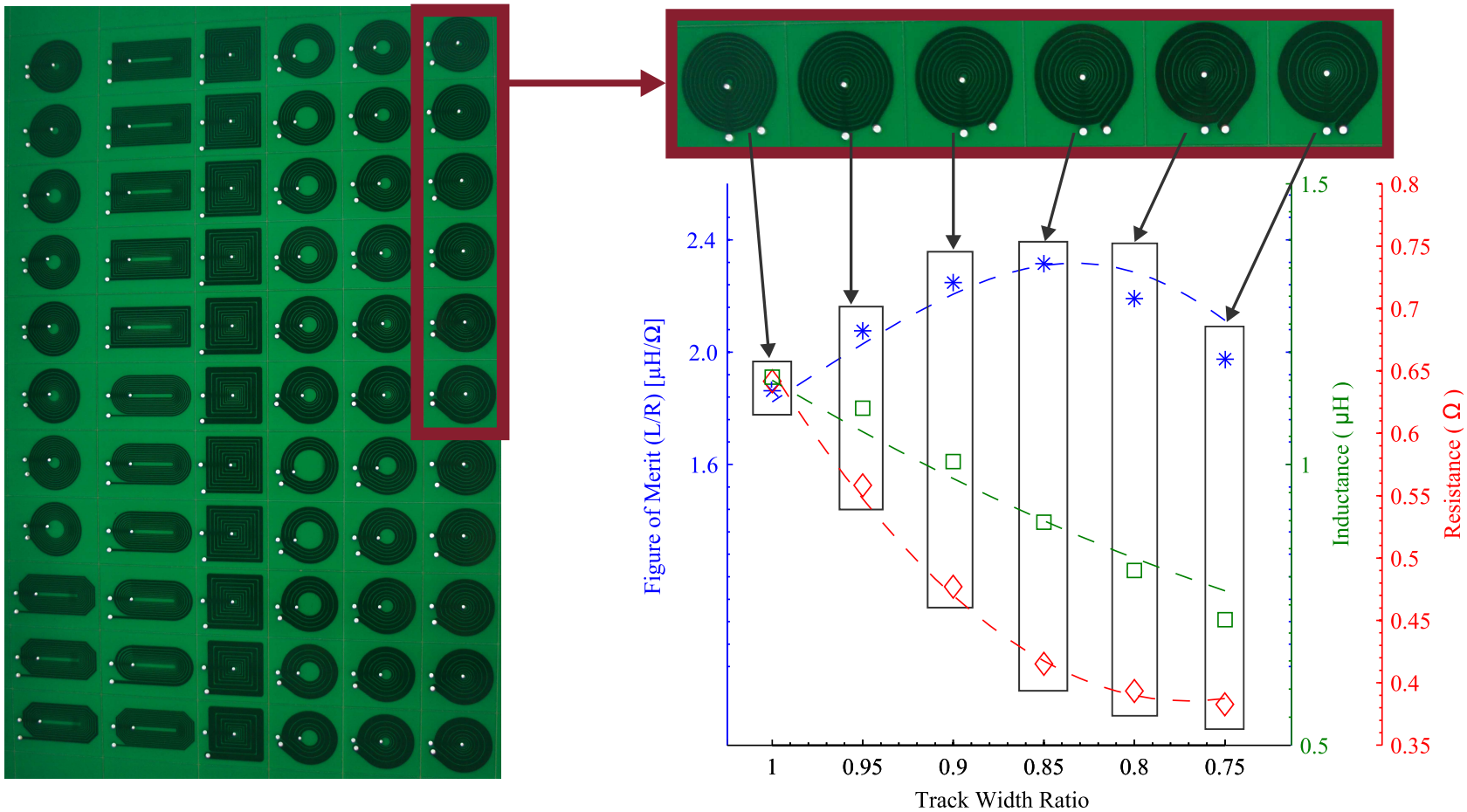

Figure 2.13: 10-Turn planar spiral windings employed in the design example to highlight the accuracy of the proposed inductance and resistance models and to confirm an improvement in the $\frac{L}{R}$ of the winding. Applying a TWR of 0.85 increased $\frac{L}{R}$ by 18%.

With the models from the preceding design procedure, L_N, R_N and $\frac{L_N}{R_N}$ were plotted vs. TWR in Fig. 2.13, in dashed lines. What was observed is that both resistance and inductance decreased as the TWR decreased from unity, but at different rates. This change in rates caused the ratio $\frac{L_N}{R_N}$ to increase until a peak was observed and then decrease again, highlighting a peak at a TWR of 0.85. Also contained in Fig. 2.13 is a panel of planar spiral windings employed in experimental confirmation of the models employed in this chapter, specifically five windings used to confirm the trends observed in this design example. L_N and R_N were measured with an impedance analyzer and the data included in Fig. 2.13, confirming the modeled trends, with a peak performance at a TWR of 0.85. The optimized winding showed an improvement in $\frac{L_N}{R_N}$ of 18%.

One of the most important insights from this design example is that the TWR which provides the minimum resistance is not the same value that provides the maximum ratio of inductance to resistance. This is due to the decrease in inductance with TWR, that shifts the maximum towards a higher TWR value. As observed in 2.13 the minimum resistance point actually occurs at a TWR of 0.765.

2.5 Summary

In this chapter, the generalized racetrack planar spiral winding and the unified dimensional system were proposed as a technique for the analysis of planar spiral windings of a variety of winding shapes and designs. The most novel aspect of the planar winding structure is the capability of modeling the effects when track widths are changed with a constant ratio, defined the Track-Width-Ratio (TWR).

The self and mutual inductance for this complex structure were modeled based on the work of Greenhouse and Grover, with the application of the proposed unified dimensional system. Single and multiple layer windings were considered and the results were compared

to simulation and experimental measurements in order to confirm their accuracy. The inductance trends observed as a part of this work suggest that the inductance of a planar spiral winding decreases exponentially as TWR decreases from unity, and that this decay is more distinct in windings with more turns. This decay was then investigated with an infinitely-thick magnetic substrate below the winding and the same normalized trend was observed, with an absolute multiplier of 2.0 of the coreless inductance value.

Also, models for the low-frequency resistance of the generalized racetrack planar spiral winding were developed analytically as a summation of the length to width of each turn of the winding. One general resistance model was presented which encompassed all subset winding families: circular, rectangular, octagonal, and traditional racetrack. This model was compared to simulation and experimental measurements of a series of windings from this work and previous literature in order to demonstrate the capabilities of TWR to reduce resistance. The resistance trends observed with the use of TWR involved a parabolic decrease in resistance until a minimum is reached, followed by a parabolic increase in resistance as TWR is decreased further. A model to predict at which TWR this resistance minimum occurs was then derived.

A design example was then performed in order to find the best TWR to be employed to maximize the performance of a planar spiral winding. This performance was measured by the ratio of the inductance to the resistance, $\frac{L}{R}$. The design example highlighted that there is a maximum for this ratio, and that it diverges from the minimum in resistance. The optimized design winding had a TWR of 0.85 and improved $\frac{L}{R}$ by 18%.

Chapter 3

AC Quality Factor Improvement in Planar Spiral Windings[3]

In the previous chapter it was established that changing the turn track widths with a constant ratio can improve the $\frac{l}{R}$ performance of planar spiral windings under low-frequency operation. This improvement is an excellent first-step towards a better design for spiral windings, but is rarely encountered in common applications. In practical scenarios, the designer must account for high-frequency magnetic field effects (skin effect and proximity effect) which can disturb the current density in the cross-section of the planar spiral. In this situation, the previous analysis cannot adequately predict the winding losses, and new techniques must be applied.

This chapter aims to present a modeling approach to high frequency resistance for the generalized racetrack planar spiral winding. This technique will be derived from the state-of-the art in high-frequency resistance modeling [38], which marries analysis with normalized finite element simulations. The prediction method in this work will apply a parabolic approximation based on the previous work when TWR is considered.

Once this prediction method is established, a technique is presented in order to mitigate high-frequency resistive losses in planar spiral windings. This technique uses a combined approach of applying TWR and increasing the internal radius to find the optimal design to reduce the effects of high-frequency resistance. When this approach is combined with the

[3]Portions of this chapter have been published in [S. R. Cove, M. Ordonez, N. Shafiei, J. Zhu, "Improving Wireless Power Transfer Efficiency Using Hollow Windings with Track-Width-Ratio," *IEEE Trans. Power Electron.*, vol. 31, no. 9, pp. 6524–6533, Sept. 2016.]

inductance prediction modeling presented in the previous chapter, an optimal quality factor can be determined for a desired winding inductance.

Fig. 3.1 highlights the two steps in the design process and how they come together to form the final hollow winding with TWR. Circular spirals are presented to increase the clarity of the image, but this technique is applicable to the generalized racetrack planar spiral winding and its subset winding families. This chapter will establish that the proposed design technique can increase the Q of the winding while allowing for an adjustable inductance, which is a feature that is not exhibited in any other technique. Inductance tuning is achievable because increasing the internal radius increases the inductance, while applying TWR reduces it. This control over the inductance is favorable for any application which is sensitive to the designed inductance value.

In order to exhibit the benefit of the proposed techniques, Design of Experiments (DoE) methodology is employed to develop meta-models of the R, L, and Q of a subset of planar spiral windings, to observe the trends with a variety of winding design parameters. The models will be experimentally confirmed to be highly accurate, and a design example will be included in order to design a high performance planar spiral winding for a 5 W Wireless Power Transfer system, based on the Qi specification.

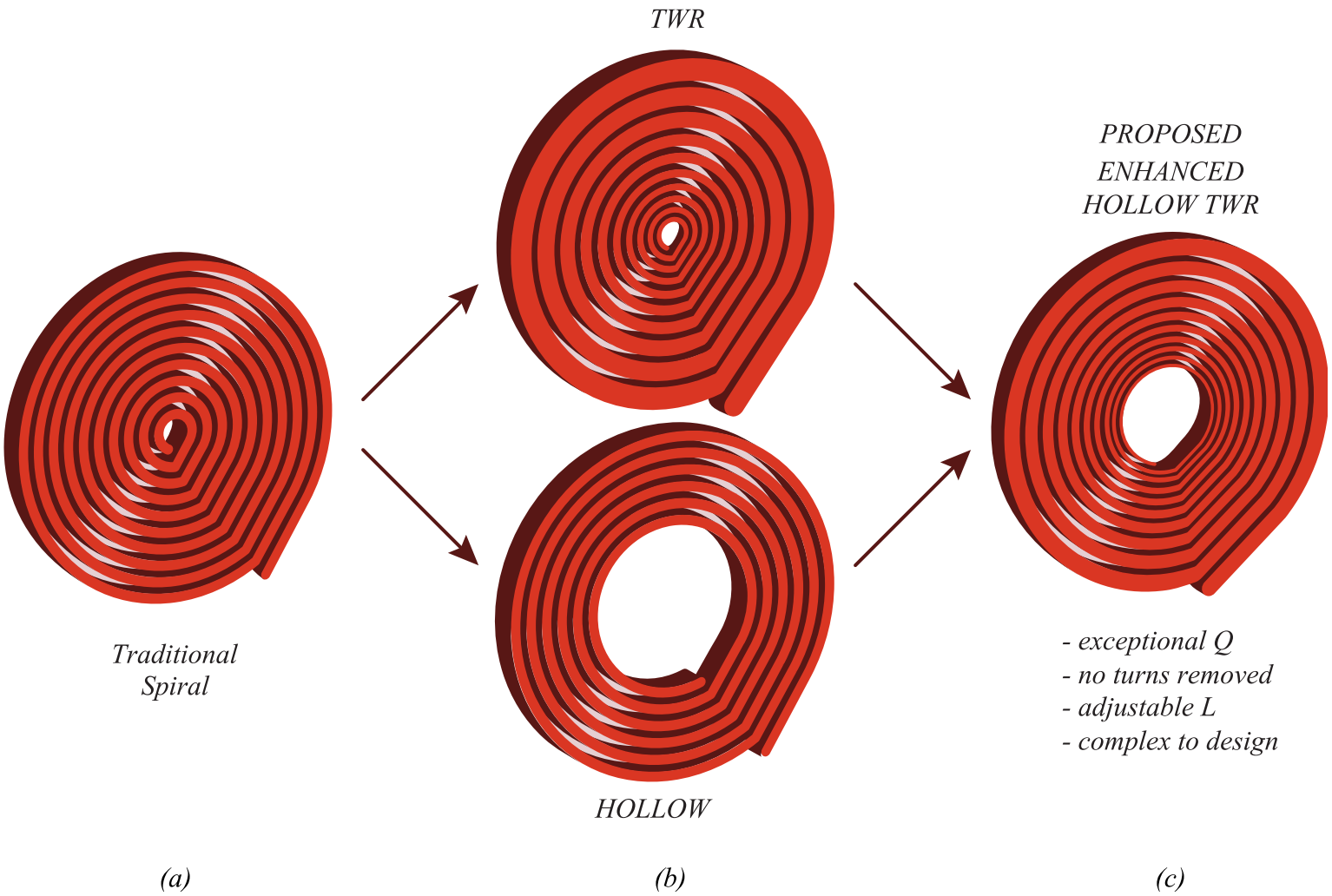

Figure 3.1: Circular planar spiral windings: (a) baseline full planar spiral winding (b) two upgrade paths previously presented for the baseline case (Track-Width-Ratio and hollowing by removing turns) (c) proposed hollow spiral winding with an increased inner radius and a non-unity Track-Width-Ratio between turns.

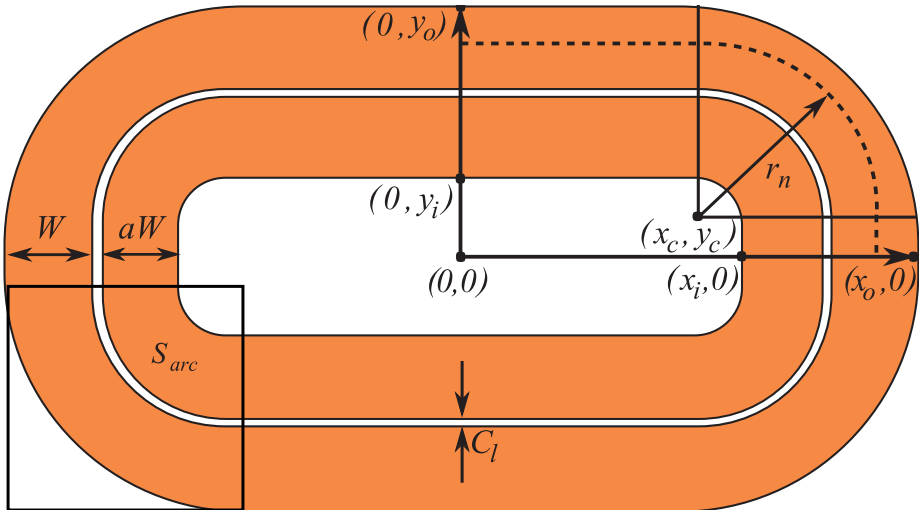

Figure 3.2: Important dimensions for the generalized racetrack planar spiral winding with Track-Width-Ratio (TWR = a) applied.

3.1 High Frequency Resistance Modeling for Planar Spiral Windings

The previous chapter introduced the generalized racetrack planar spiral winding and the unified dimensional system which continues to be employed for analysis in this chapter. A brief reminder of the shape and the important dimensions has been included in Fig. 3.2. Other important dimensions are the number of layers, N_L, and the layer spacing, s.

3.1.1 High Frequency Effects in Planar Spiral Windings

Planar spiral windings suffer from AC losses due to high magnetic field strength normal to their surface, creating high frequency eddy-current losses. These fields can be generated from high-frequency currents within the conductor of interest (skin effect) or from external conductors in close proximity (proximity effect). Fig. 3.3 presents select flux lines in a cross-section of a typical 3-turn planar spiral winding, demonstrating the flux which causes the

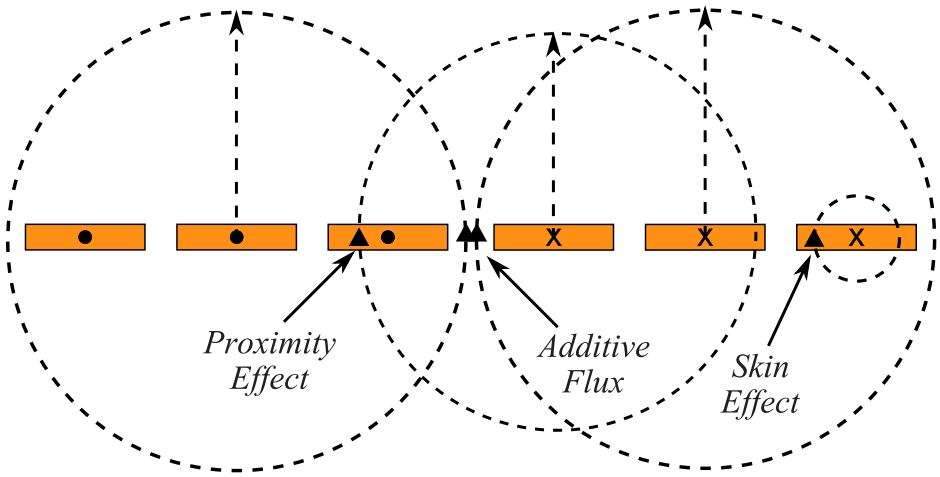

Figure 3.3: Select idealized flux lines in a 3-turn planar spiral winding, demonstrating the flux which causes skin effect, proximity effect, and the additive flux in the center of the winding. The direction of the current is indicated with dot and cross notation.

skin and proximity effect, as well as an important phenomenon in the center of the winding where the flux lines are all directed in the same direction. This additive flux presents a poor environment for planar conductors, as they will be susceptible to higher eddy-current losses. Finite element simulation was used to highlight the impact of this issue in a qualitative setting. Fig. 3.4 (a) shows a top-down view of the magnetic field strength simulation results of a circular planar spiral winding. The field is strongest in the center, which is inducing high-frequency losses on the inner turns. Fig. 3.4 (b) displays a cross-sectional look at the flux vectors whose magnitudes were represented in Fig. 3.4 (a). A distinct pattern of increased magnetic flux in the center of the winding is displayed, with very little extension vertically. The strength of the magnetic flux vectors decrease radially until they are at their weakest outside the winding, where the majority of the flux cancels itself.

This situation poses a critical problem when the internal turns in a traditional planar spiral winding contribute the least to the overall inductance, and are so wide that they contribute the highest resistive losses. The traditional approach to this problem was to remove inner turns, which provides a trade-off of lower inductance but much lower resistance [39, 40].

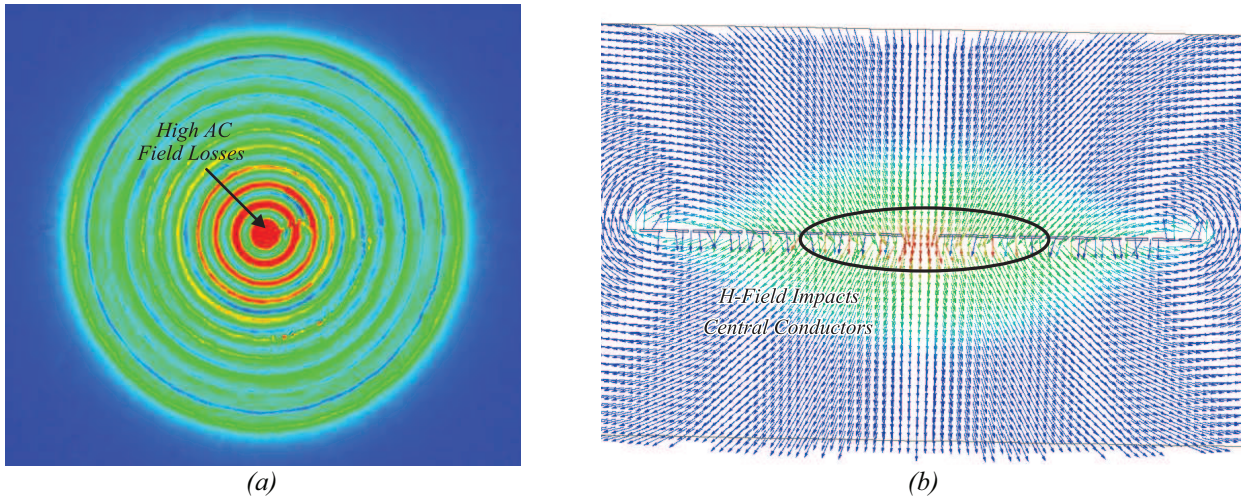

Figure 3.4: (a) Magnetic field strength, H, for a horizontal cross-section of a circular planar spiral winding. (b) Magnetic field intensity vector, $\vec{H}$, for a vertical cross-section of a circular planar spiral winding.

The problem is that the inductance can decrease a significant amount, which is unacceptable if this is for a resonant application, such as wireless power transfer. Even a 5 or 10% change in inductance will alter the resonant frequency of the system significantly.

The proposed technique builds on two different techniques to combat the high resistive losses in the internal turns: increasing the internal radius, $r_i = x_i - x_c$ and applying a non-unity TWR to the turns. In this way, the internal turns avoid more of the flux, and have less surface area for the flux to make contact with the winding. This scenario is qualitatively described in Fig. 3.5, where the magnitude of the magnetic flux, H, is plotted from an FEA simulation for the case with even widths and a proposed winding with increased internal radius and reduced TWR. The scales in both cases are the same, and demonstrate how less copper is impacted with strong magnetic fields. The work in this chapter will demonstrate that this represents a reduction in high-frequency resistance and that these two factors can be used to tune the inductance. It will be found that increasing the internal radius of the winding will increase the inductance of the spiral, while the application of TWR decreases

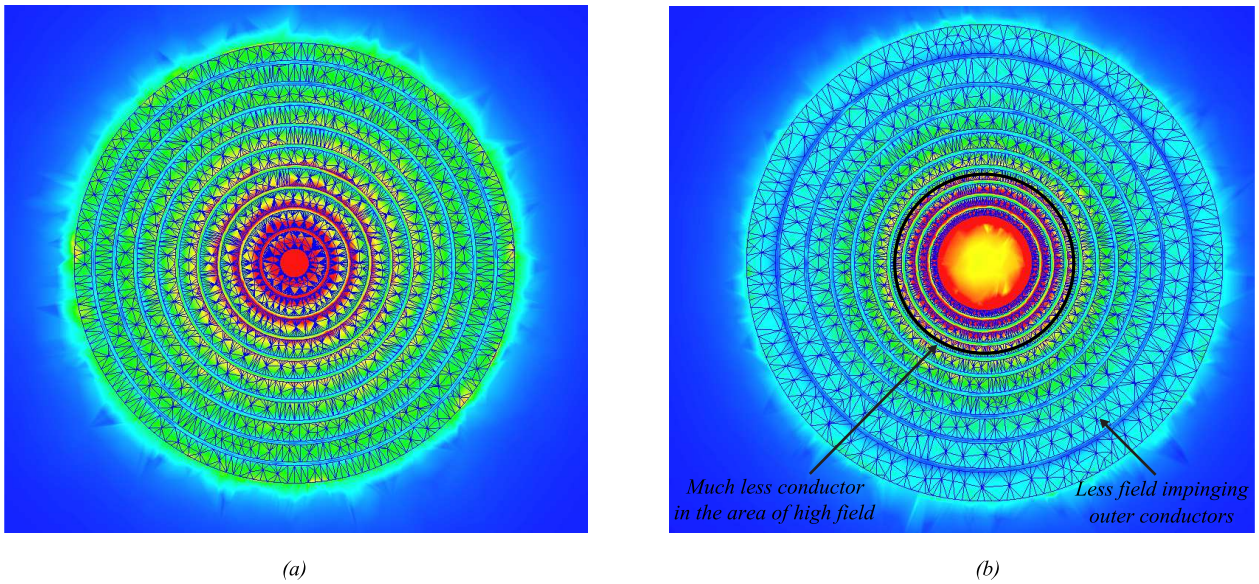

Figure 3.5: (a) Descriptive magnetic field strength, H, for a horizontal cross-section of a circular planar spiral winding with ten turns of equal width. (b) Descriptive magnetic field strength, H for a horizontal cross-section of an improved 10-turn hollow planar spiral winding with TWR applied. Both the footprint and scales are the same, and less copper is impinged with high magnetic field strength in the proposed winding structure.

it. In this way the two parameters can be tuned to provide the maximum quality factor for a given footprint, inductance, and operating frequency.

3.1.2 Modeling Resistance

The AC resistance model of the hollow spiral winding with TWR employed is based on previous work on a quasi-analytical approach to high frequency resistance estimation in planar spiral windings [38]. Finite element analysis (FEA) was inserted into the analytical model in a normalized fashion based on the conductor width and thickness in terms of the skin depth. The losses were broken down into conduction losses and proximity losses. Since the proximity losses are induced by magnetic fields which impinge the conductors at various angles, there is an x and z component to the proximity loss term (where z is vertically

upward). The models are duplicated here for clarity [38]:

$$R_{ac} = R_{cond} + R_{prox,x} + R_{prox,z} \tag{3.1}$$

where

$$R_{cond} = \frac{1}{w_n t \sigma} \Phi_{cond,rec} \left(\frac{w_n}{\delta}, \frac{t}{\delta} \right) \tag{3.2}$$

$$R_{prox,x} = \frac{1}{w_n t \sigma} \Phi_{prox,rec} \left(\frac{w_n}{\delta}, \frac{t}{\delta} \right) |\overline{H}_{o,x}|^2 \tag{3.3}$$

$$R_{prox,z} = \frac{1}{w_n t \sigma} \Phi_{prox,rec} \left(\frac{w_n}{\delta}, \frac{t}{\delta} \right) |\overline{H}_{o,z}|^2 \tag{3.4}$$

Each resistance value is per unit of length, and the Φ values are normalized frequency and geometry dependent values which are determined from FEA and are visually represented in [38]. The magnitudes of the orthogonal x and z components of the magnetic field from the proximity effect are estimated by FEA as well.

These models were established for windings with a constant conductor width. In this work, further FEA was performed in order to establish the effect of a non-unity TWR for hollow planar spiral windings. The result is a quadratic function of resistance based on frequency and the previously defined physical characteristics of the winding, which is normalized to the resistance value, R_{ac} from (3.1). The resultant model of ac resistance of the hollow planar spiral winding with TWR is given by:

$$\frac{R}{R_{ac}} = \left(\frac{N N_L x_i}{C_l f x_o} a^2 + \frac{N_L f x_o}{N x_i C_l} a + \frac{x_o^2 \sqrt{f} C_l}{N N_L x_i} \right) \tag{3.5}$$

which is a parabola with no roots and a minimum that falls between $a = (0,1)$. That minimum

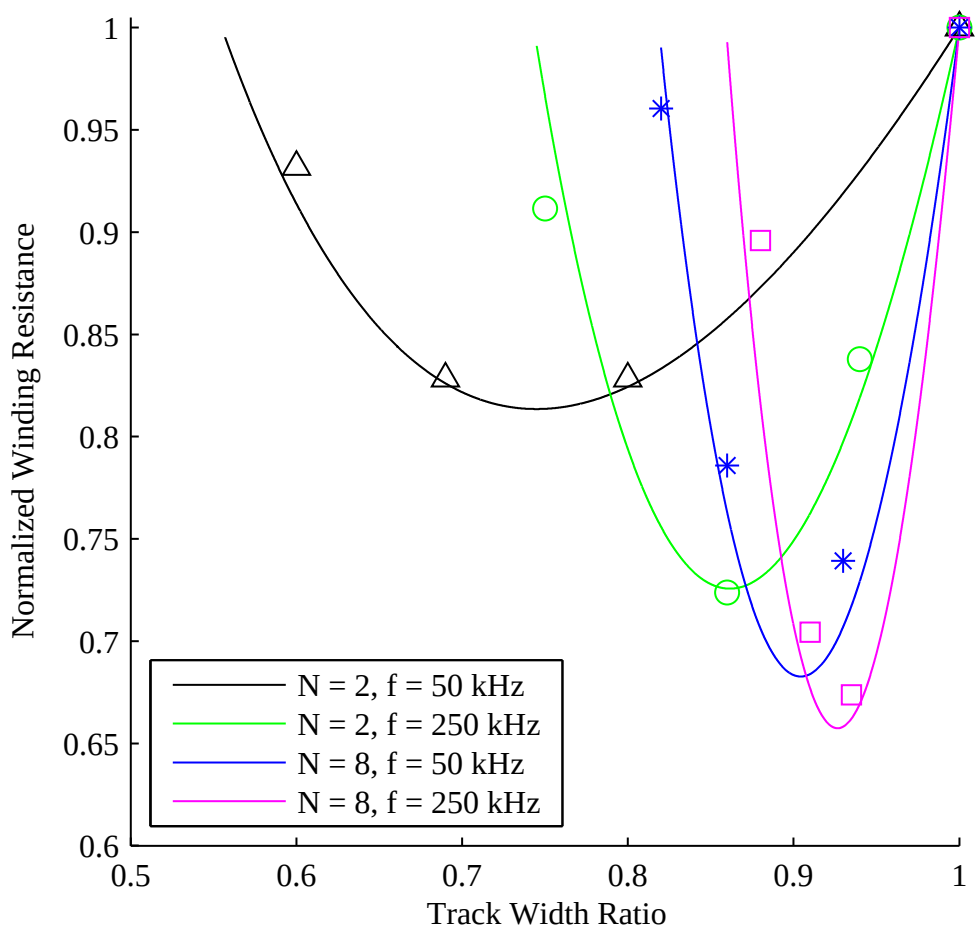

Figure 3.6: Resistance trend of hollow planar spiral windings with Track-Width-Ratio applied. Predicted values are compared to 16 finite element simulations, varying number of turns and frequency of operation.

can be determined by differentiating (3.5) and setting the result equal to zero:

$$0 = \left(\frac{2NN_L x_i}{C_l f x_o} a_{min} + \frac{N_L f x_o}{N x_i C_l} \right) \tag{3.6}$$

The model is accurate over the interval $a = [2a_{min} - 1{,}1]$, at which point the resistance of the winding exceeds R_{ac} and there is no benefit derived from employing TWR at that

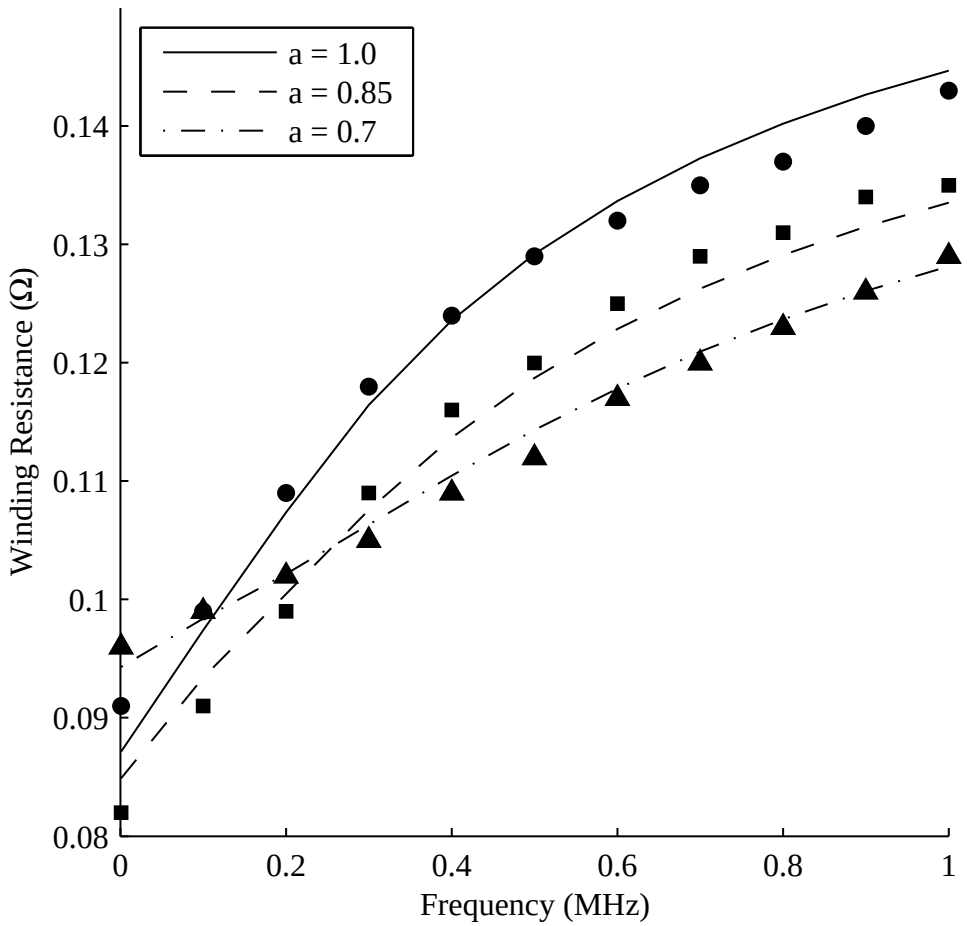

Figure 3.7: Finite element validation of the high frequency resistance models for the $N = 6$ windings. The model accurately highlights the non-linearity of the resistance with respect to frequency, and the frequency dependence of the optimal TWR value.

frequency.

3.1.3 Finite Element Simulation Validation

Figs. 3.6 and 3.7 present resistance curves for various combinations of turns, frequency, and TWR with comparisons with the models provided in this chapter. Beyond indicating the high accuracy of the model, some insights from Fig. 3.6 are that a_{min} increases as the number of turns increase, and that the impact of a on resistance increases with the number of turns and the frequency of operation. Fig. 3.7 takes a different approach and keeps the number of turns constant while varying the TWR and frequency. This plot demonstrates that as the frequency changes, the preferred TWR changes, but at no point is the traditional case ever the optimal one. At low frequencies a conservative value of TWR provides a preferred response, which eventually is usurped by a TWR that departs further from unity.

3.2 Meta-Models for Resistance, Inductance, and Quality Factor

While the previously derived models for high-frequency resistance and inductance can accurately predict the performance of planar spiral windings with TWR applied, their use in design is limited by reliance on finite element simulations or summations of summations. In order to quickly observe the effect of TWR with frequency, or any other physical parameter, statistical Design of Experiments (DoE) will be employed in conjunction with the unified dimensional system to extract meta-models of the inductance, high frequency resistance, and then quality factor. DoE [62] is a technique to deal with complex multivariate non-linear systems. In particular, the variables for the analysis will be the parameters of the unified dimensional system. Modeling the effects of every combination of the unified dimensional

Table 3.1: Factors range of operation

Factor	Low	Mid	High	Units
x_c	0	20	40	mm
y_c	0	15	30	mm
$x_i - x_c$	0	2	4	mm
$x_o - x_c$	5	15	25	mm
N	2	6	10	turns
Frequency	0	0.5	1.0	Mhz
a	0.80	0.90	1.0	

system coordinates and frequency one at a time would be computationally impractical and require significant resources without providing any insight into the interactions between factors. To produce accurate parametric models, a face-centered Central Composite Design (CCD) is used. The methodology employs ANOVA regression analysis to provide parametric models of the form

$$F(Y) = a_0 + \sum_{i=1}^{m} a_i u_i + \sum_{i=1}^{m} \sum_{j=1}^{m} b_{ij} u_i u_j \tag{3.7}$$

where Y is the response being measured (inductance, resistance, quality factor), F represents a functional transform of Y (such as natural log or square root), a_0 is the overall average of measurements, a_i are linear regression coefficients, b_{ij} are quadratic and interaction regression coefficients, m represents the number of factors while u_i and u_j represent the factors being varied. These equations are valid over the entire factor ranges with an accuracy proportional to the adjusted R^2 value of the model.

The unified dimensional system combined with frequency provide the factors of the experiment, allowing for a thorough investigation based on geometry and non-linear current distribution. The factor ranges were chosen in order to encompass all of the winding designs currently used by the Qi standard for WPT [65], in preparation for the design example at the end of this chapter, and are summarized in Table 3.1. A quarter-fractional face-centered

CCD with 7 factors requires $2^5 = 32$ calculations with factors at high and low values, $2 \times 7 = 14$ calculations with all but one factor at its mid point, and 1 calculation where all factors are at their mid point, totalling 47 calculations [62].

One important note is that the number of layers is a non-continuous variable, meaning that it can only be employed in integer values. In this case, different meta-models will be required for different numbers of layers. This work covers 2 and 4 layer winding models.

3.2.1 High Frequency Resistance Meta-Model

All 47 factor combinations were calculated through the application of the high frequency resistance model proposed in this chapter, within the ranges specified. The resultant parametric model of high frequency resistance of generalized racetrack planar spiral windings with 2 layers (in $m\Omega$) is:

$$\begin{aligned} ln(R_{ac2l}) \times 10^3 = {} & 3190 + 30.3x_c + 37.6y_c + 28.4(x_i - x_c) \\ & - 194(x_o - x_c) + 814N + 459f - 946a \\ & - 0.429x_cy_c - 0.571x_c(x_o - x_c) + 0.668x_cN \\ & - 0.694y_c(x_i - x_c) - 4.28N(x_o - x_c) \\ & + 19.8f(x_o - x_c) + 93.7a(x_o - x_c) \\ & - 36.2N^2 - 356f^2 + 7.967a^2 \end{aligned} \tag{3.8}$$

and the model for 4 layers is:

$$
\begin{aligned}
ln(R_{ac4l}) \times 10^3 = {} & 6409 + 46.8x_c + 70.2y_c + 49.6(x_i - x_c) \\
& - 276(x_o - x_c) + 892N + 651f - 680a \\
& - 0.872x_cy_c - 0.693x_c(x_o - x_c) + 0.888x_cN \\
& - 0.977y_c(x_i - x_c) - 7.34N(x_o - x_c) \\
& + 34.0f(x_o - x_c) + 140.1a(x_o - x_c) \\
& - 59.2N^2 - 563f^2 + 11.4a^2
\end{aligned} \tag{3.9}
$$

These high frequency resistance meta-models highlights the highly nonlinear and interactive nature of resistance. They also support each other in that all of the same factors were deemed statistically significant in each model, and only the coefficients changed. The 2-layer model has an adjusted R^2 value of 0.9942 indicating an exceptional fit with the calculated data (the ideal value is 1.0), while the 4-layer model has an adjusted R^2 value of 0.9931.

The proposed models provide deep insight into the impact of each factor of the experiment as well as highlight the interactions that exist between many of the factors. It is an efficient way to analyze the resistance of a wide variety of generalized racetrack planar spiral windings and the accuracy is at its highest within the range of factors presented in Table 3.1. Designs outside of this space can be investigated using the proposed equation as an initial design check.

3.2.2 Inductance Meta-Model

The inductance was calculated for the same 47 factor combinations as the resistance was. The inductance was determined by the models from Chapter 2, repeated here for clarity. The

self inductance was calculated from:

$$L_{s_N}(\mu H) = \sum_{n=1}^{N} 0.002 l_n \left[log_e \left(\frac{2l_n}{t + a^{N-n}W} \right) + 0.50049 + \left(\frac{t + a^{N-n}W}{3l_n} \right) \right] \tag{3.10}$$

and the mutual inductances were calculated from either the relation:

$$M_l(\mu H) = 2l \left[log_e \left\{ \frac{l}{GMD} + \left(1 + \frac{l^2}{GMD^2} \right)^{\frac{1}{2}} \right\} - \left(1 + \frac{GMD^2}{l^2} \right)^{\frac{1}{2}} + \frac{GMD}{l} \right] \tag{3.11}$$

or

$$M_{jk}(\mu H) = 0.001(\frac{\sqrt{2}}{2}) l_j \left[log_e \frac{1 + \frac{l_k}{l_j} + \frac{l_{j+k}}{l_j}}{1 - \frac{l_k}{l_j} + \frac{l_{j+k}}{l_j}} + \frac{l_k}{l_j} log_e \frac{\frac{l_k}{l_j} + \frac{l_{j+k}}{l_j} + 1}{\frac{l_k}{l_j} + \frac{l_{j+k}}{l_j} - 1} \right] \tag{3.12}$$

where the GMD was assumed to be the distance between the center of each conductor. The resultant inductance was calculated as a sum of the self and mutual inductances as per the work of Greenhouse. The 47 datapoints were analyzed statistically for the 2 and 4-layer cases and the resultant meta-models are given as:

$$\begin{aligned} L_{2Layer} &= 12 + 2.6x_c + 4.75y_c + 28.4(x_i - x_c) \\ &- 194(x_o - x_c) + 814N - 946a \\ &- 0.429x_c y_c - 0.571x_c(x_o - x_c) + 0.668x_c N \\ &+ 93.7a(x_o - x_c) - 36.2N^2 - 1.64a^2 \end{aligned} \tag{3.13}$$

for the 2-layer case and:

$$\begin{aligned} L_{4Layer} &= 23 + 5.0x_c + 7.9y_c + 11.2(x_i - x_c) \\ &+ 13.6(x_o - x_c) + 814N - 946a \\ &- 0.429x_cy_c - 0.571x_c(x_o - x_c) + 0.668x_cN \\ &+ 15.7a(x_o - x_c) + 36.2N^2 - 3.23a^2 \end{aligned} \tag{3.14}$$

for the 4-layer case. L is calculated in μH, and the adjusted-R^2 of each equation is 0.966 and 0.974 respectively. This is considered to be an excellent fit to the simulated data. It is also noticed that in each case the significant factors remain the same and only the coefficients change. This is one more sign of consistency in the results. It is also important to notice that frequency was not deemed to be a significant factor in the inductance, since it is always measured at DC.

3.2.3 Resultant Quality Factor Meta-Model

Having the meta-models for L and R, the data for the quality factor meta-model were derived from the equation:

$$Q = \frac{\omega L}{R} \tag{3.15}$$

where L and R were the same data that was used for (3.8), 3.9, (3.13), and (3.14). The resultant model for 2-layers is

$$\begin{aligned} Q_{2Layer} = {} & 25 + 1.8x_c + 4.3y_c + 12.7(x_i - x_c) \\ & - 1.98(x_o - x_c) + 9.34N + 2.23f - 1.93a \\ & - 0.112x_cy_c - 0.445x_c(x_o - x_c) + 0.215x_cN \\ & - 0.872y_c(x_i - x_c) - 5.23N(x_o - x_c) \\ & + 13.2f(x_o - x_c) + 16.8a(x_o - x_c) \\ & - 24.5N^2 - 113f^2 - 4.22a^2 \end{aligned} \tag{3.16}$$

and the model for 4-layers is:

$$\begin{aligned} Q_{4Layer} = {} & 40 + 3.2x_c + 7.65y_c + 22.3(x_i - x_c) \\ & - 3.62(x_o - x_c) + 18.72N + 6.31f - 2.49a \\ & - 0.343x_cy_c - 0.788x_c(x_o - x_c) + 0.451x_cN \\ & - 1.38y_c(x_i - x_c) - 7.33N(x_o - x_c) \\ & + 16.2f(x_o - x_c) + 20.2a(x_o - x_c) \\ & - 30.8N^2 - 148f^2 - 7.2a^2 \end{aligned} \tag{3.17}$$

where Q is a dimensionless quantity. The adjusted R^2 of the Q models are 0.988 and 0.967 respectively. Each model contains the same terms of different weighting, and it is a function of every dimension of the investigation in a highly nonlinear manner.

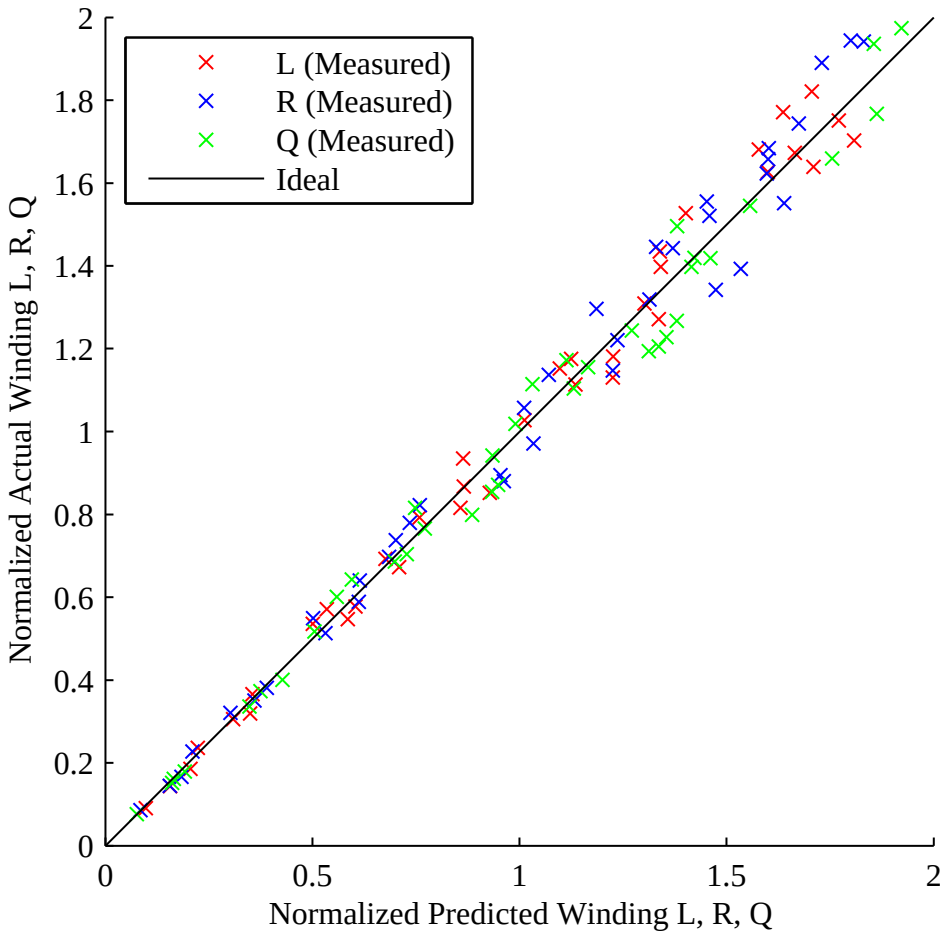

Figure 3.8: Normalized simulated vs. predicted data for L, R, and Q for circular planar spiral windings employing a variety of turns, inner radius, and Track-Width-Ratio. L is normalized to 40 μH, R was normalized to 250 $m\Omega$, and Q was normalized to 25.

3.2.4 Meta-model Accuracy Confirmation

Fifty planar spiral windings that fit within the dimensions from Table 3.1 were simulated using finite element analysis in order to evaluate the accuracy of the proposed meta-models. The normalized results for R, L, and Q at various layers are presented in Fig. 3.8. The meta-models fit the data exceptionally well, within 5% of the simulated value in all occurrences. With these powerful meta-models on hand, the proposed technique of the hollow planar spiral winding with TWR can be evaluated in a design example, and then in a dynamic example

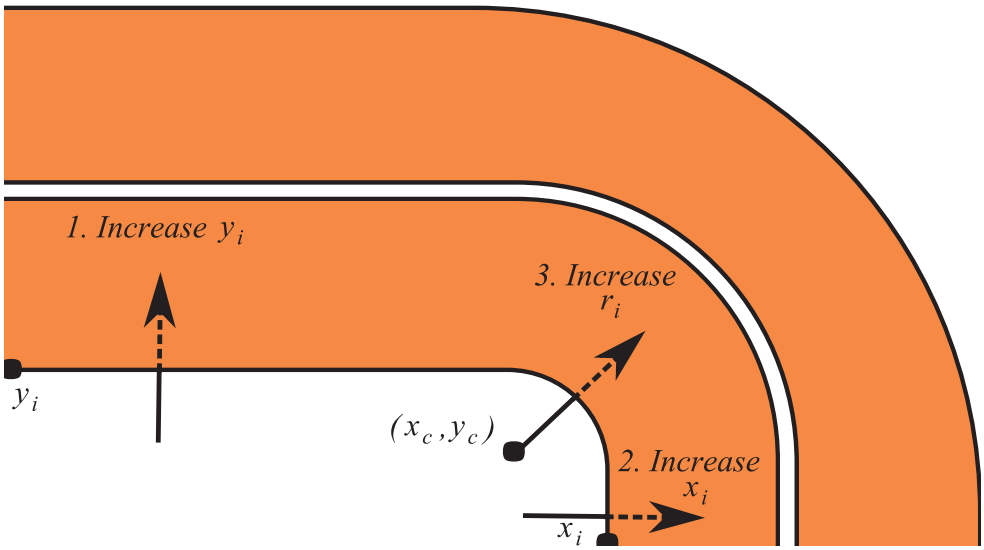

Figure 3.9: Three distinct methods of hollowing the generalized racetrack planar spiral winding: 1. Increasing y_i, 2. Increasing x_i, 3. Increasing r_i. This work chooses the symmetric approach of increasing r_i, such that x_i and y_i will always increase by the same amount.

in a 5 W WPT system.

3.3 Improving Quality Factor by Applying Hollow Track-Width-Ratio

Now that the high-frequency resistance of the generalized racetrack planar spiral has been established, this work presents the hollow generalized racetrack planar spiral winding as a method to reduce the high frequency losses. The combination of hollowing the winding with the application of TWR allows for designs which can reduce the amount of copper affected by the high frequency magnetic field generated by the winding. There are three ways in which the internal dimensions of the unified dimensional system could be changed to indicate a hollowing of the winding, which are highlighted in Fig. 3.9:

1. Increasing y_i, while maintaining x_i constant.

Table 3.2: Factors range of operation

Factor	Value	Units
x_c, y_c	0, 0	mm
N_L	2, 4	
f	150	kHz
N	10	turns
x_o	15	mm
C_l	0.25	mm
t	0.105	mm
s	1.0	mm

2. Increasing x_i, while maintaining y_i constant.

3. Increasing r_i, which increases both y_i and x_i uniformly.

This work focuses on only option 3, in which the internal corner radius, r_i, is increased such that x_i and y_i increase uniformly. In this way, the increase matches closely with that of a purely circular winding, and the assumptions from the previous chapter can still apply, in that:

$$x_o - x_i = y_o - y_i \tag{3.18}$$

and

$$x_i - x_c = y_i - y_c \tag{3.19}$$

and also, it removes $x_i - x_c$ and $x_o - x_i$ from the analysis and replaced with r_i and r_o.

3.3.1 Inductance and Quality Factor Trends

While the meta-models were presented earlier, it is not readily apparent how L and Q change when isolated to just the changes of the internal radius and the TWR. In this section, a subset of the windings from the meta-model domain are investigated in order to determine the trends

with the change of r_i and a. The static dimensions of the investigated windings are included in Table 3.2. The results of the investigation can be observed in the 3-D plots in Fig. 3.10 for the 2-layer spirals and Fig. 3.11 for the 4-layer spirals. They highlight that there is a maximum Q for a given footprint and frequency, for this case. The quality factor improves with an increase in a and r_i until a peak is reached, and then reduces. The peak Q can be significantly higher than the baseline winding, in this case an increase of 400% is observed in the 2-layer case. This is natural because of the way TWR reduces the resistance of the winding. If this plot is observed in slices of constant inductance, from Fig. 3.10 it still exhibits a maximum Q for each slice. Fig. 3.11 demonstrates the changes in the surface when more layers are added. In this case, the peak Q is attained from higher values of x_i and a, at a value higher than the 400% observed in Fig. 3.10. This makes sense since the field is stronger in the middle with the added layers, requiring a higher internal radius and stronger TWR to reduce the high frequency resistance. It is important to notice that the inductance does not reduce to provide this exceptional behavior. The following section confirms the models experimentally, while investigating the performance of the proposed windings compared to traditional hollow windings.

3.4 Experimental Confirmation and Application Example: Low Power WPT Spiral

In this section, many aspects of experimental testing of the previous meta-models are discussed. First, some practical winding considerations are presented in regards to designing circular windings. This spirals are the only ones which require some approximation with manufacturing, in order to keep clearances constant. Then the resistance, inductance, and quality factor meta-models will be confirmed with experimental measurements. Following

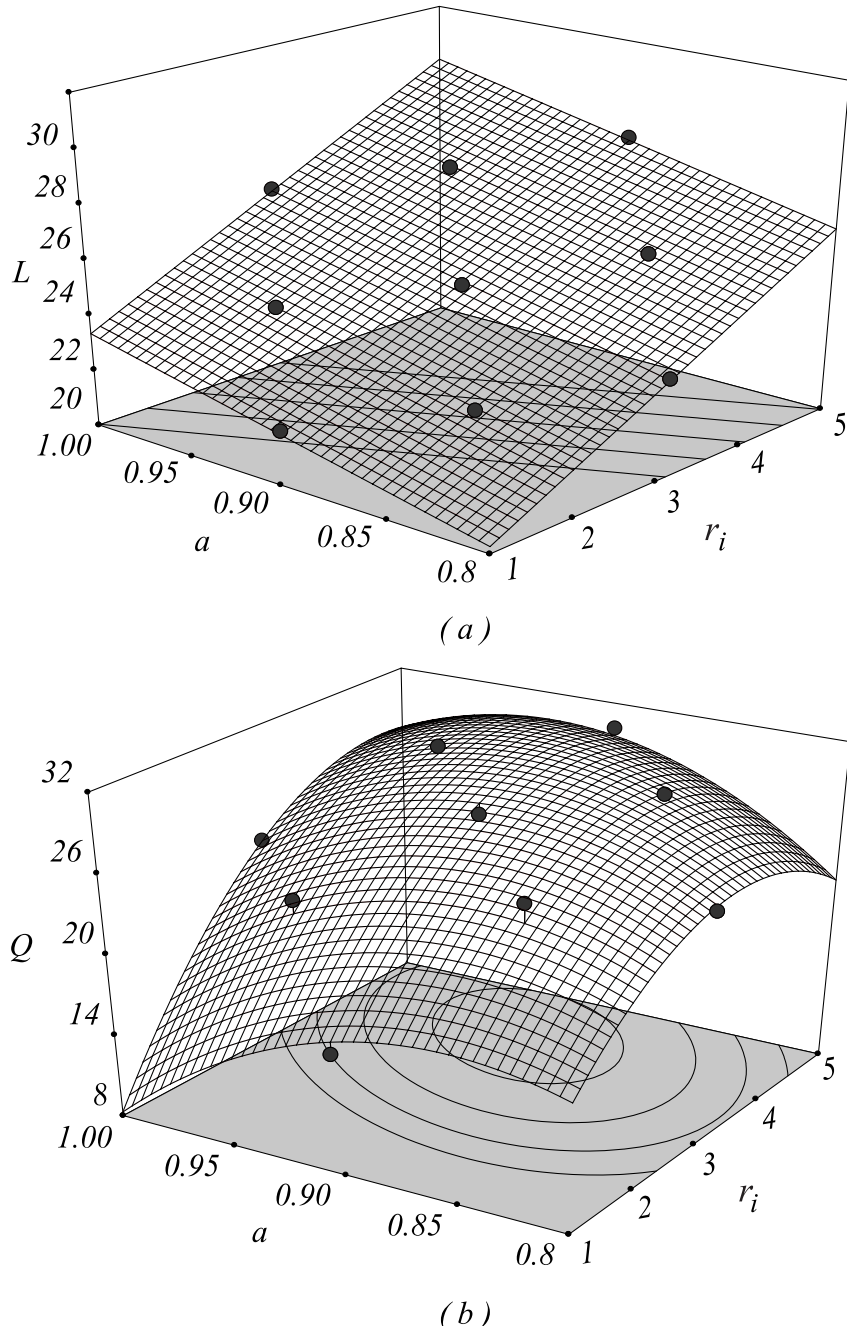

Figure 3.10: 3-D representations of the inductance and quality factor for windings described in Table 3.2 at 200 kHz (a) inductance of 2-layer windings in μH (b) quality factor of 2-layer windings

that, an application example of a 5W Wireless Power Transfer system will be presented, in which the proposed hollow planar spiral winding is compared to the traditional planar spiral

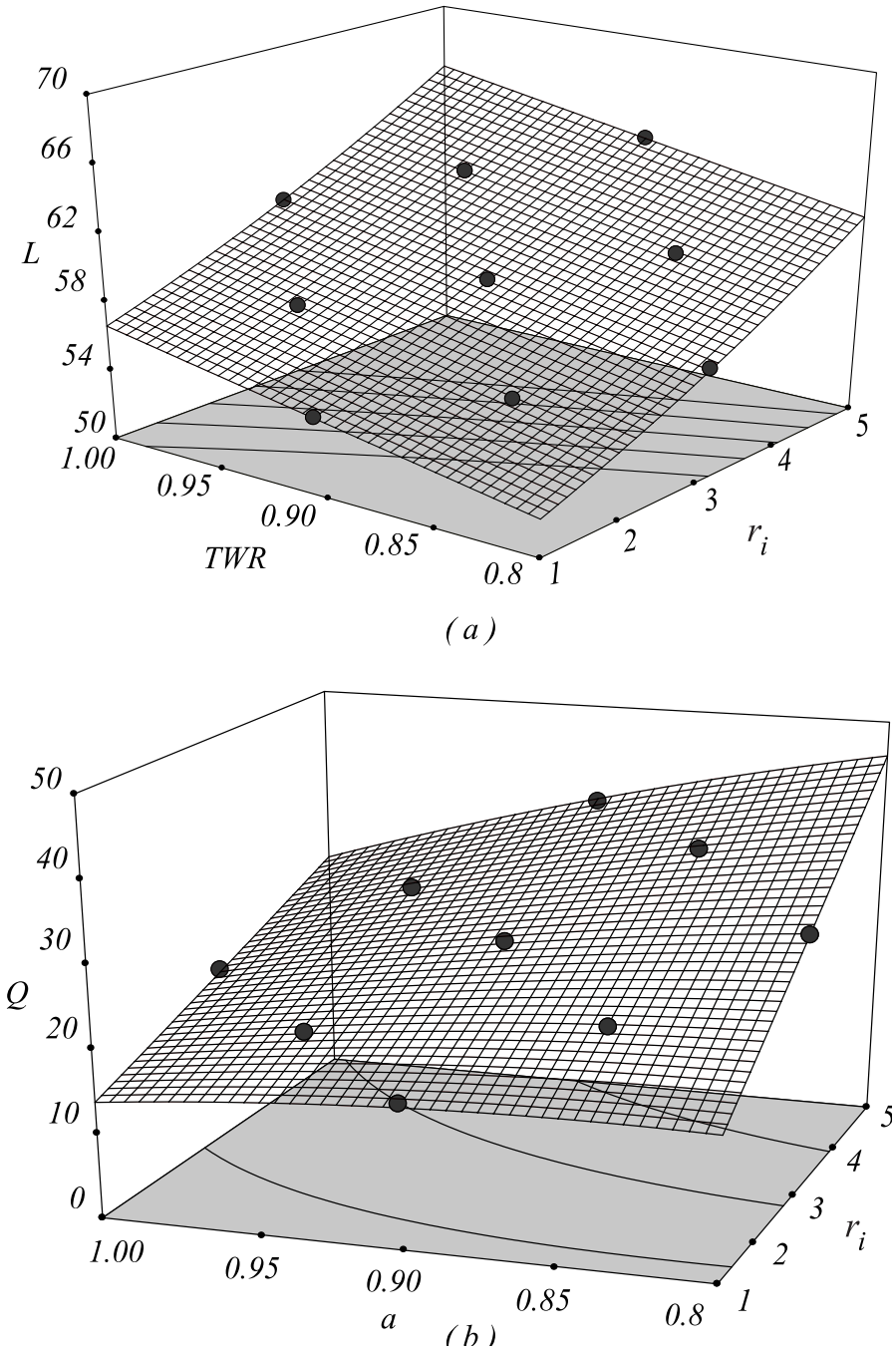

Figure 3.11: 3-D representations of the inductance and quality factor for windings described in Table 3.2 at 200 kHz (a) inductance of 4-layer windings in μH (b) quality factor of 4 layer windings.

winding, and the planar spiral winding which has been hollowed by removing turns.

3.4.1 Practical Winding Considerations for Circular Spirals

There are various practical implementation considerations when employing windings with a non-unity TWR. One is the way in which the turns of various width are connected. The approach that was taken for the physical experimentation in this work has minimized the effect of turn connections while still maintaining a constant clearance so that the voltage rating of the spiral is not impacted. For the rectangular spirals, the width changes at the 90 degree angles between turns such that no additional connection is required. Circular windings are comprised of N concentric circular arcs of approximately 300° and the outer turn is connected to the inner turn by a straight trace, as observed in Fig. 3.12. The connections are as seamless as possible as to not deviate far from the ideal concentric-turn analysis. The overall conductor length was compared between the ideal construction and the practical circular winding for all windings tested in this work and they all portrayed less than 2% difference when compared.

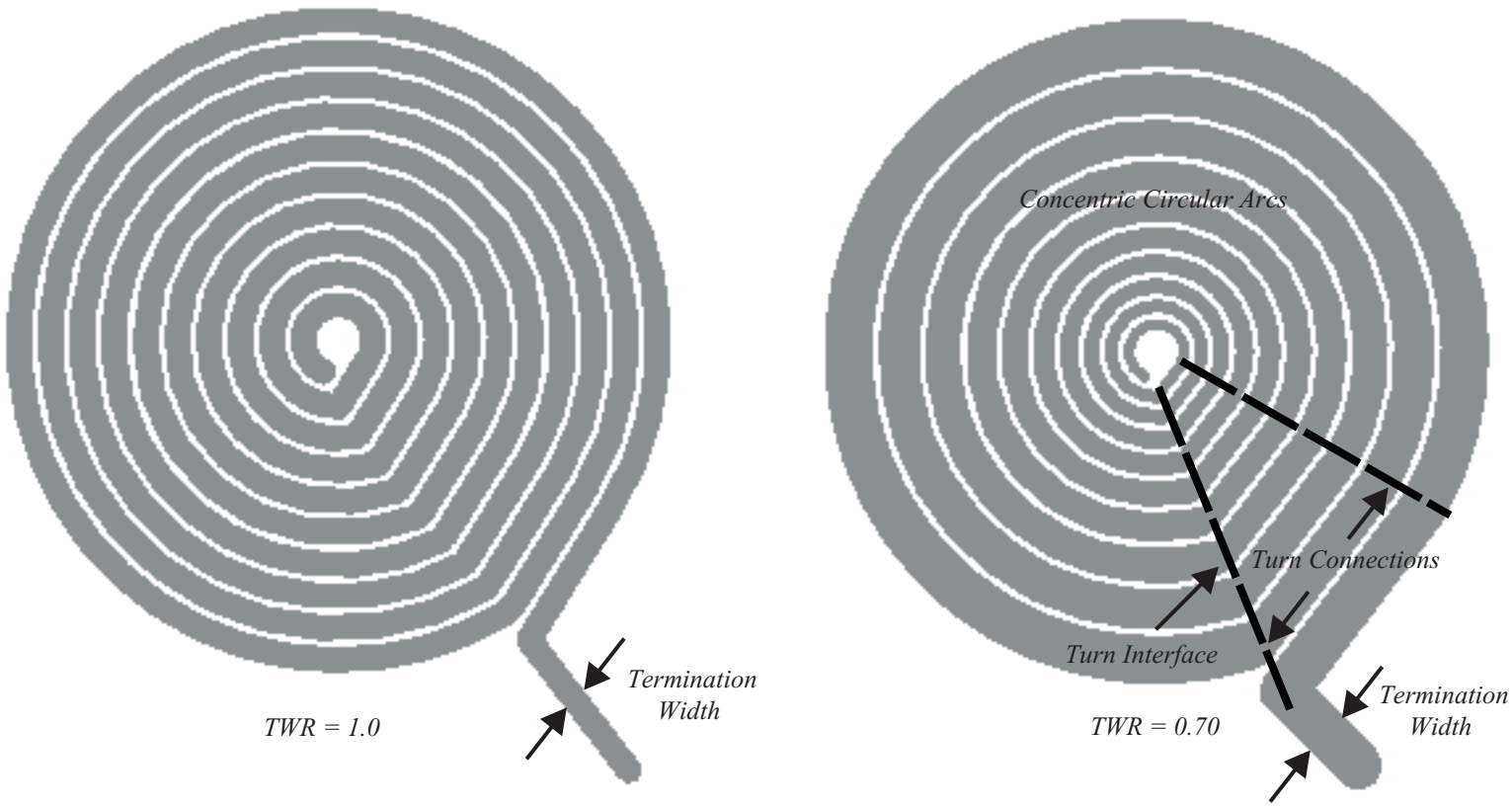

Figure 3.12: The practical implementation of a 10 turn circular winding with a = 1.0 and 0.85, highlighting the method in which the turns of varying width are connected as well as the improvement in termination track width.

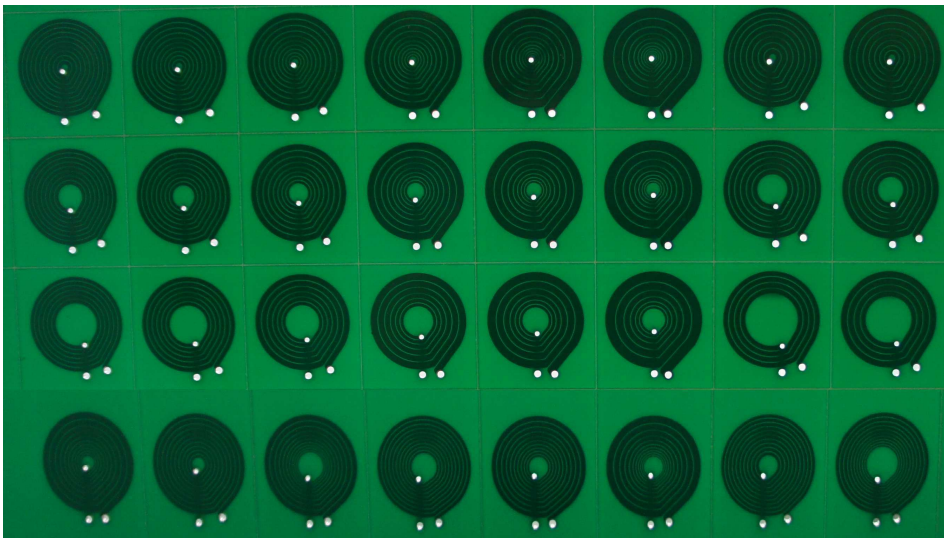

Figure 3.13: Subset of circular windings employed to test the accuracy of the proposed modeling of the hollow planar spiral winding with TWR.

The other consideration is connecting the layers, and then the inductor to the external circuit. In order to connect the winding layers, vias are used at the center of the winding to allow for external connection on a lower PCB layer. A conservative estimate of less than 1 A per via is used when determining the number of vias. All tests performed in this work contained the exact same connection to the winding from the bottom layer of a 2 layer board. When connecting the winding to the external circuit, one of the benefits of applying a non-unity TWR is acknowledged in Fig. 3.12, which is that the input termination track width can be much wider than the unity TWR case which can reduce connection losses. In this particular case the windings with $a = 0.85$ has an input connection which is 3 times wider than the unity TWR case.

3.4.2 Experimental Prototype and Performance

Fig. 3.13 shows a series of circular planar spiral windings that were manufactured in order to test the models developed in the previous section and their L, R, and Q were measured

by employing a high-accuracy impedance analyzer. Excellent correlation was found between the measurements and the calculated results from the models employed in this work, as can be observed in Fig. 3.8. Tight tolerances, less than 5%, are noticed between predicted and actual values for L, R, and Q. In this situation, they are normalized parameters, where L was normalized to 40 μH, R was normalized to 250 $m\Omega$, and Q was normalized to 25.

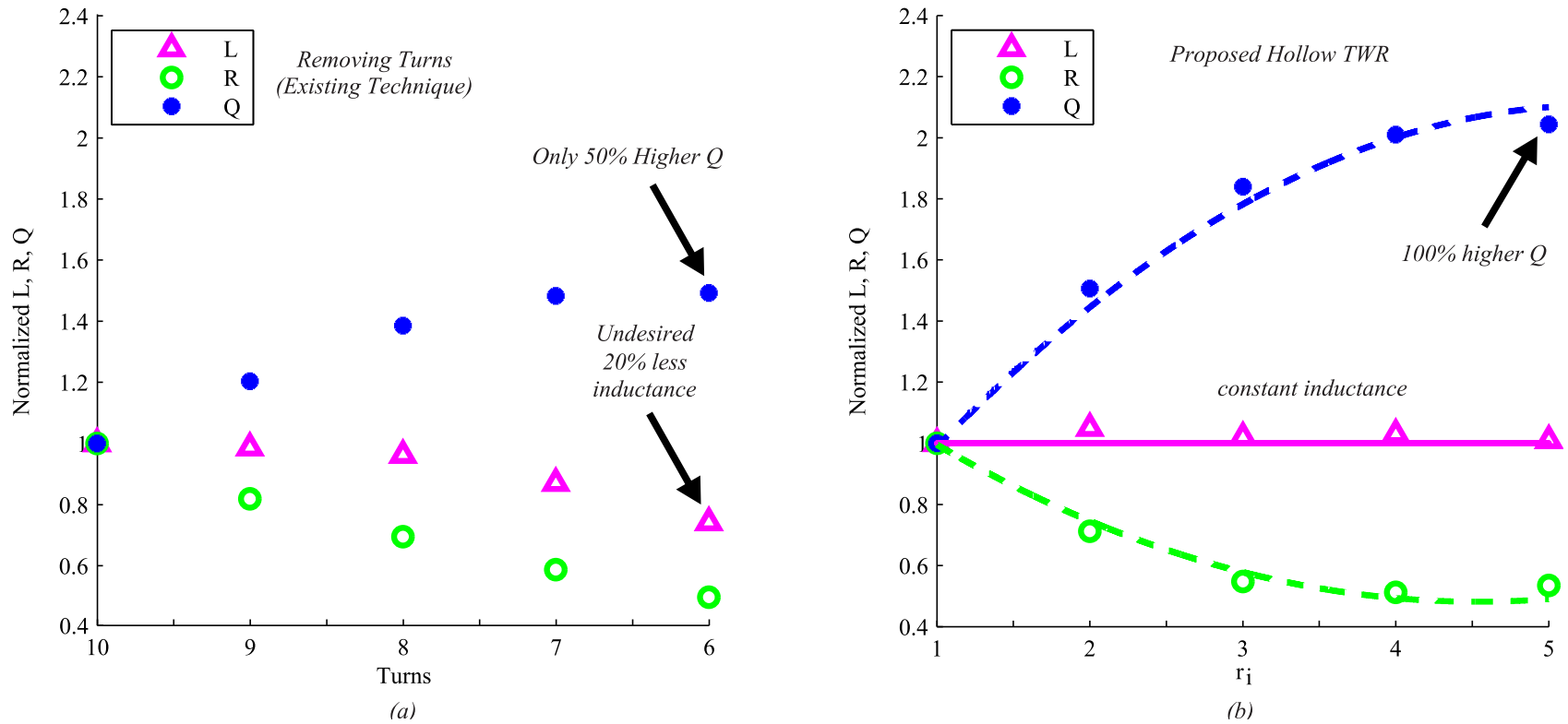

Figure 3.14: (a) Normalized representation of the performance of hollow planar spiral windings by removing turns. Q is normalized to 15, L is normalized to 25 μH, and R is normalized to 475 $m\Omega$. A 15% reduction in L is observed in order to attain a Q which is 50% higher. (b) Normalized experimental confirmation for L, R, and Q of 2-layer proposed hollow circular planar spiral windings with Track-Width-Ratio. Q is normalized to 15, L is normalized to 25 μH, and R is normalized to 475 $m\Omega$. It can be observed that by tuning the combination of x_i and a, the inductance stays almost constant while Q doubles.

Table 3.3: WPT Experimental Specifications

Factor	Value	Units
L	25	μH
N_L	2	
f_r	100	kHz
f	105-200	kHz
l	10	mm
V_{in}	19	V
P_{out}	5	W

3.4.3 Low Power Wireless Power Transfer Application

The proposed hollow planar spiral windings with TWR have the benefits of greatly increased quality factor compared to traditional approaches and have the added benefit of being able to tune the inductance up or down without changing the footprint. This makes the technique much more suitable for low power, resonant WPT systems such as those covered by the Wireless Power Consortium's Qi standard. In this section, the trends observed in Figs. 3.10 and 3.11 are confirmed experimentally, then compared to experimental data from the approach of removing inner turns, and finally three windings are chosen for testing in a 5 W WPT system and their transmission efficiencies are documented: the baseline case, the best case winding with turns removed, and the best case proposed hollow planar spiral windings with TWR applied. The specifications of the WPT system are contained in Table 3.3.

The maximum frequency of operation is 200 kHz, which is where the ac losses will be at their worst. This is the frequency the windings will be designed for. At 25 μH inductance, a 2 layer solution is chosen due to inspection of Fig. 3.10, whose surface was used to define a locus of designs for which the inductance is predicted to stay at 25 μH. A series of spirals were manufactured to confirm this behavior, and were compared to the trends provided from Figs. 3.10 and 3.11. The results are presented in Fig. 3.14(c). The data points follow 25 μH

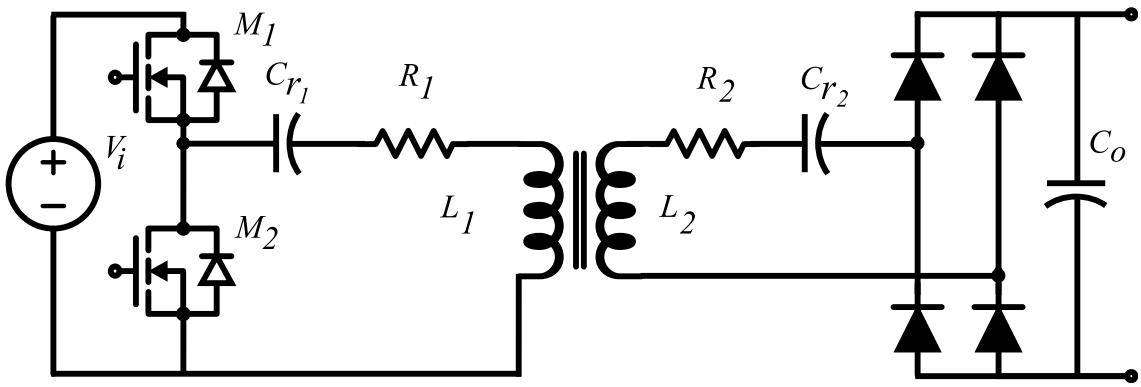

Figure 3.15: Schematic of the experimental wireless power transfer circuit. The inductors L_1 and L_2 are the spirals under test.

inductance line and plot the resistance and Q of the combination, up to the point calculated here as the maximum. The inductance stays approximately constant, while the resistance decreases greatly, culminating in a Q which is over twice the initial value. These results are then compared with those achieved from hollowing the planar spiral by removing inner turns. In this case, the procedure was straightforward: measure L, R, and Q of a series of spirals in which one turn is removed at a time and observe the results. The data for this particular case is displayed in Fig. 3.14(b). The Q only reaches 50% higher than the baseline case, and at that point the inductance is reduced by 20%. This will also require a capacitor which is 25% larger in order to achieve the same resonant frequency for wireless power transmission. The proposed technique of increasing the internal radius and applying TWR has more flexibility and provides a nearly constant value of inductance. This is intuitive as the resistance decreases when the turns are shifted from the high field in the center, and the shorter turn lengths get matched with smaller winding widths. The inductance increases from the effect of hollowing, then decreases from the application of TWR, which provides the tunable inductance.

Three windings were placed in a WPT system, whose simplified circuit diagram is included

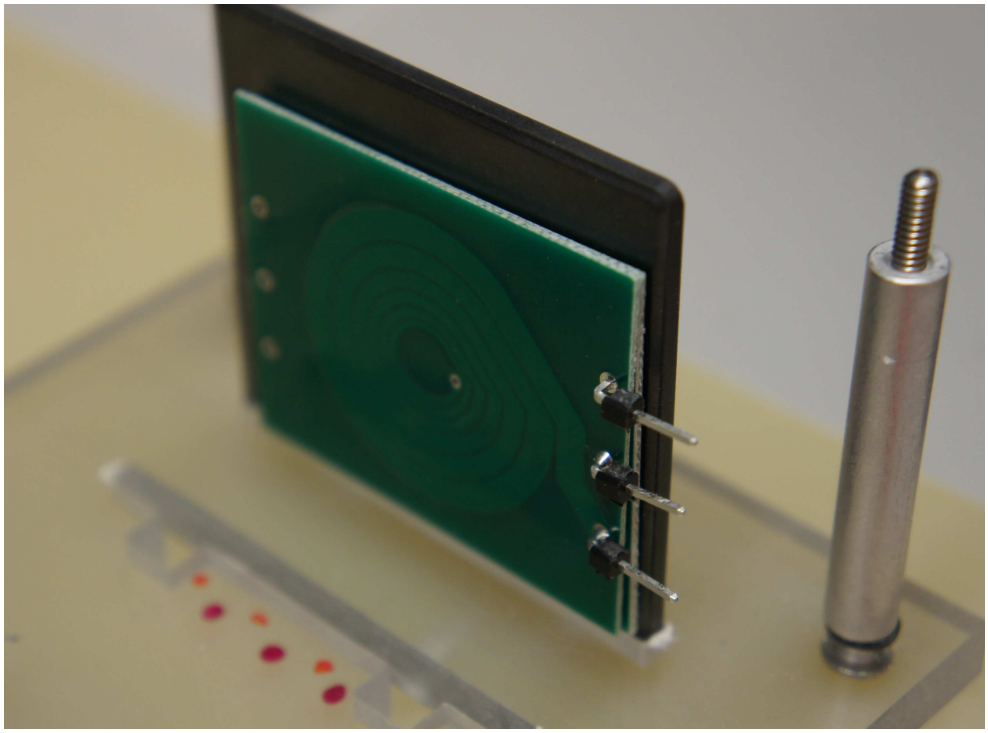

Figure 3.16: Wireless power transfer system with proposed hollow planar spiral windings with Track-Width-Ratio. Several connections and alignment aids have been removed to add clarity.

in Fig. 3.15: the completely filled winding (baseline), the highest-Q option when turns were removed, and the highest-Q option when the inner radius was increased and TWR was applied. The series capacitors were chosen in order for resonance to occur at 100 kHz, and operation was swept from 105 kHz to 200 kHz. A deconstructed view of the proposed winding setup in the WPT transmission system is displayed in Fig. 3.16 with no alignment aids or connections such that the spiral can be observed.

Efficiency was compared at full load (5 W) condition. The best efficiency in each case was at around 170 kHz, in which the baseline case had a 70% transmission efficiency (Fig. 3.17), the winding with turns removed had 80% (Fig. 3.18), and the proposed winding had 90% (Fig. 3.19). As predicted by the modeling, the proposed design method pushes planar spiral

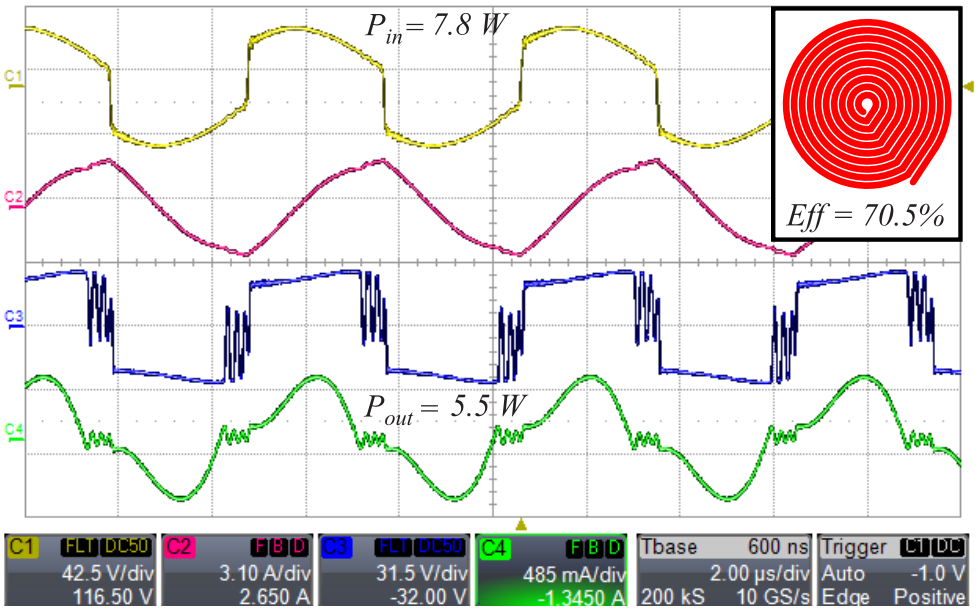

Figure 3.17: Input voltage, input current, output voltage, and output current of the WPT system employing the baseline full planar spiral windings with a unity Track-Width-Ratio at 170 kHz. Input power is 7.8W and output power is 5.5 W, demonstrating a 70.5% efficiency.

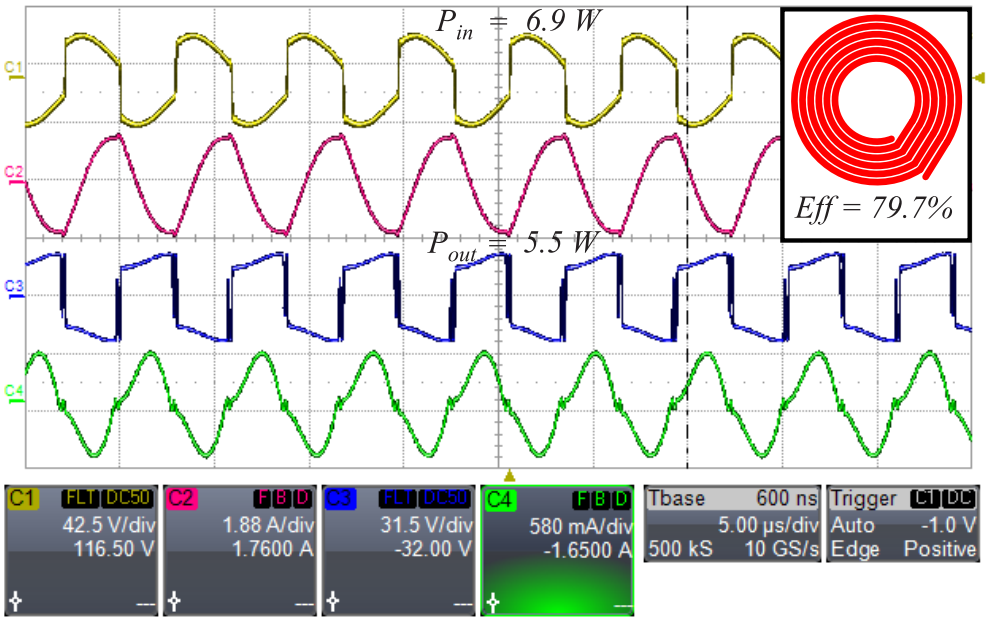

Figure 3.18: Input voltage, input current, output voltage, and output current of the WPT system employing hollow planar spiral windings with 4 turns removed at 170 kHz. Input power is 6.9W and output power is 5.5 W, demonstrating a 79.7% efficiency.

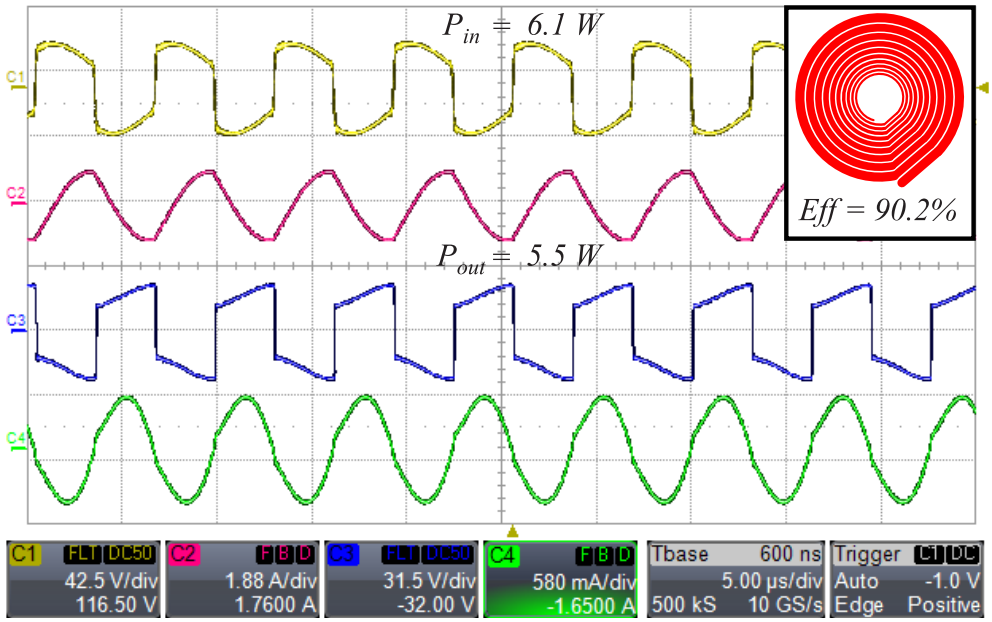

Figure 3.19: Input voltage, input current, output voltage, and output current of the WPT system employing the proposed hollow planar spiral windings with non-unity Track-Width-Ratio at 170 kHz. Input power is 6.1W and output power is 5.5 W, demonstrating a 90.2% efficiency, the highest performance of the experimental cases.

windings to exceptional efficiencies. The resulting low profile, high efficiency winding can be used for WPT in slim consumer electronics for battery charging purposes.

3.5 Summary

This chapter introduced the hollow spiral winding with Track-Width-Ratio (TWR) as a means of improving the Quality Factor (Q) of planar spiral windings. The proposed winding structure involved a two-factor interaction between extending the internal radius of the planar spiral winding in order to make it hollow, and then to apply TWR in order to decrease the width of internal turns of the winding. In doing so, the area of copper which can be impinged by the magnetic field is reduced, decreasing the overall ac resistance of the winding.

This work applied a quadratic factor to the previous work to account for the application of TWR in order to predict the behavior at any frequency of operation. Since this technique

is still reliant on finite element simulation data, a statistical Design of Experiments approach was employed to create meta-models of the resistance values for a subset of windings in order to observe the resistance trends with frequency, and later as part of a design example.

Similar meta-models were created for the inductance, employing the models from Chapter 2. This investigation confirmed that the increase in internal radius can increase the overall inductance of the winding, while TWR can decrease it. This allowed for combinations of these factors to be employed to tune the inductance, rather than the decrease in inductance observed from previous techniques.

A specific design example was performed in order to maximize the Q of a circular planar spiral winding for application in a Wireless Power Transfer (WPT) system. Studying windings based on the Qi specification, the proposed technique was able to improve Q by 100% while keeping the inductance constant. This was compared to the technique of removing turns, which experienced a 20% reduction in inductance and only 50% increase in Q. Removing turns fails to have a second degree of freedom to tune the inductance without changing the footprint of the winding.

The proposed winding was then compared to the traditional planar spiral winding and the winding with turns removed in a 5 W, 110-200 kHz WPT system. At the rated load, the traditional planar spiral winding had an efficiency of 70%, the winding with removed turns had an efficiency of 80%, while the proposed hollow planar spiral winding with TWR had an efficiency of 90%.

Chapter 4

Capacitance Mitigation in Planar Spiral Windings[4]

One of the biggest drawbacks of employing planar spiral windings in power electronic applications is the excessive parasitic capacitance between layers and windings. The wide overlapping conductors act like capacitive plates which will reduce the operating frequency of the coil and can distort current and voltage waveforms. In the worst-case scenario, in planar transformers or wireless power transfer windings, high $\frac{dV}{dt}$ can cause shoot-through currents which can trip protections or damage devices.

Previous attempts have been made to minimize capacitance in planar magnetics [53–58]. Preliminary work has been performed on predicting capacitance in planar transformers for 2-layer coreless planar spiral windings [53] and for multi-layer planar transformers when an equal-voltage-drop model is employed between each turn [54]. Improved shielding techniques have been proposed to mitigate the impact of planar transformer capacitance [55] and a method of reducing voltage differential between overlapping conductors has shown promise for extending PCB spiral winding operating frequency with an extensive number of layer connections [56]. Recently an approach which removes the overlapping copper from the winding window has been proposed [57] and was later improved to include a connection to ground in the open space to reduce the capacitance and serve as an EMI filter [58].

[4]Portions of this chapter have been accepted for publication in [S. R. Cove and M. Ordonez, "Low-Capacitance Planar Spiral Windings Employing Inverse Track-Width-Ratio", accepted for publication in *IEEE Energy Conversion Congress and Expo. (ECCE)*, 2016.]

Figure 4.1: Planar spiral winding cross-sections and their impact on capacitance and resistance: Traditional winding techniques, removing overlapping windings, and the proposed winding with Track-Width-Ratio (a) applied in opposite directions on each layer.

In these previous investigations, either copper was removed from the winding or shields were added in order to lower capacitance. This means leakage inductances were increased, and at many frequencies the resistance was increased in order to reduce capacitance. The proposed technique in this work builds upon the techniques presented in the previous chapters. Instead of applying the same TWR to each layer of a multi-layer winding, every layer changes the reference of the TWR from the outside turn, to the inside turn, or vice-versa. Applying this technique, named Inverse TWR, the amount of overlapping conductor is reduced which results in a significant reduction in stored capacitive energy. Since the outer dimension, inner dimension, and clearance values are not changed. Compared to other techniques, the proposed method maintains better resistive and inductive properties.

This proposed inverse TWR technique is displayed in Fig. 4.1 with a qualitative description of the claims within this chapter when compared to traditional winding designs and designs which reduce the copper within the winding window. The proposed technique reduces the overlapping copper in the multi-layer winding while reducing the overall voltage gradients between overlapping turns, resulting in a significant reduction in overall capacitance. This chapter provides a revised low-frequency resistance model for the proposed inverse TWR structure, a specific case of the windings in Chapter 2. This model is employed to find the voltages for each turn in order to simulate the capacitance employing 2D finite element analysis. The inductance model in Chapter 2 is employed to calculate the inductance of the proposed structure.

The analytical results for low frequency highlight the capability for improvement over the traditional case. A comparative example is included, in which the optimized planar spiral winding employing TWR was able to reduce the capacitance by 50%, reduce ac resistance up to 20%, and keep the inductance within 4% of the nominal. The winding performance was measured with an impedance analyzer to confirm the improved operation.

4.1 Capacitance in Planar Spiral Windings

The previous chapter introduced the generalized racetrack planar spiral winding and the unified dimensional system which continues to be employed for analysis in this chapter. A brief reminder of the shape and the important dimensions has been included in Fig. 4.2. Other important dimensions are the number of layers, N_L, and the layer spacing, s.

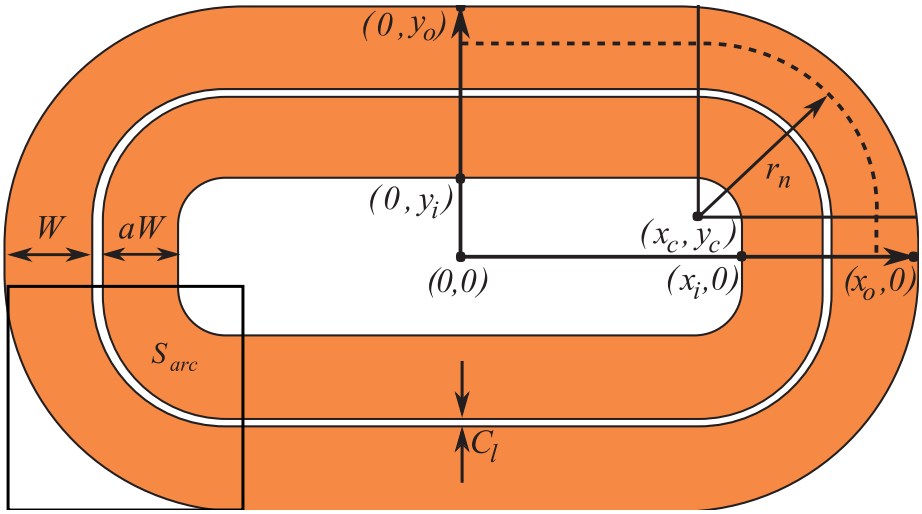

Figure 4.2: Important dimensions for the generalized racetrack planar spiral winding with Track-Width-Ratio (TWR = a) applied.

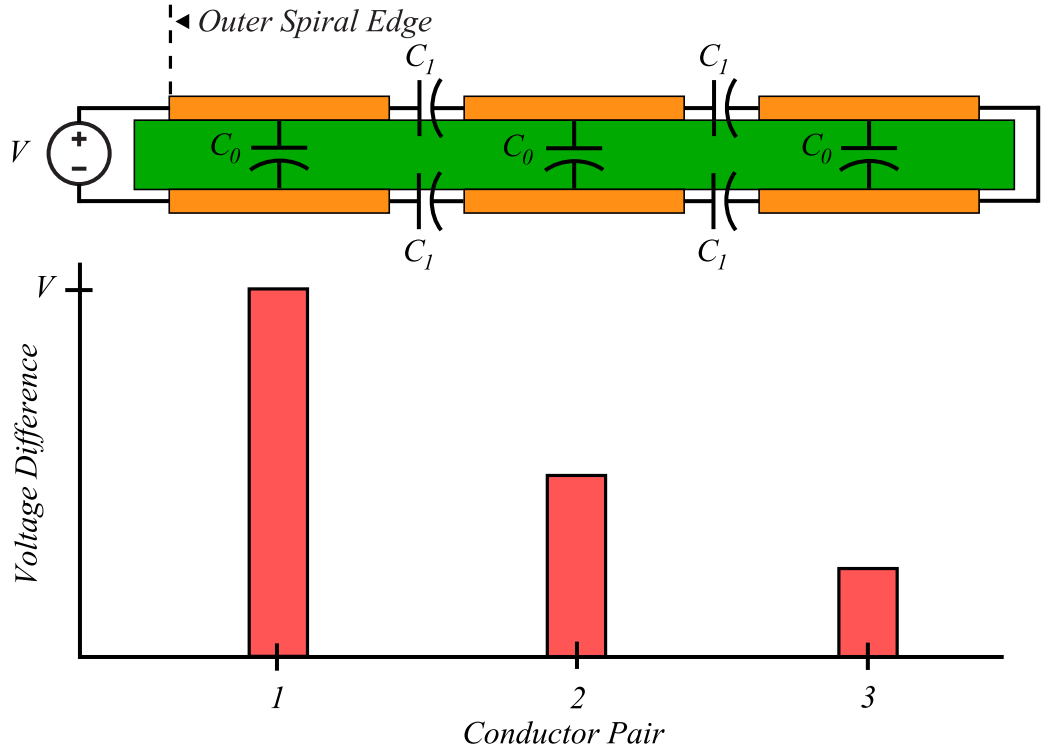

Figure 4.3: Distributed capacitance and voltage differences in planar spiral windings when voltage V is applied. Each overlapping conductor pair has the same capacitance, but a very different voltage difference between them.

4.1.1 Planar Spiral Winding Capacitance

Traditionally, the capacitance between overlapping layers in planar inductors can be approximated by considering them as parallel plate capacitors:

$$C = \frac{\epsilon A}{s} \tag{4.1}$$

where ϵ represents the permittivity of the material between the winding layers, A represents the overlapping area between conductors, and s represents the vertical distance between the two turns, as per the unified dimensional system presented in Chapter 2. This is a crude approximation due to the effects of fringing fields within the winding window, but it can be used to approximate the individual capacitive effects between turns and layers that must be summed to achieve the total capacitance of the winding, as illustrated in Fig. 4.3. This highlights that while each overlapping conductor pair has the same capacitance, C_0, the voltage differential between then is starkly different, decreasing exponentially as the conductors approach the center of the winding. This greatly affects the capacitive energy that is stored between each conductor pair (E), from the relationship:

$$E = \frac{1}{2}CV^2 \tag{4.2}$$

This demonstrates that the outer turns are the most important for determining the overall capacitive energy stored in the winding, and suggests that there are a variety of methods which can improve the capacitance of planar spiral windings:

- Reduce the overlapping area (A) in adjacent layers.
- Increase the layer separation (s) between layers.
- Decrease the voltage differential between overlapping conductors.

Considering the fact that s is generally chosen based on the required inductance and power density of the application at hand, the degrees of freedom for reducing the capacitance in planar spiral windings involves techniques to either reduce A or reduce the voltage differential. At their extremes, techniques that remove all overlapping area are prone to increased resistive losses, while techniques that completely reduce the voltage differential are prone to restrictive construction techniques and increased losses in connections between layers. This work combines both techniques but takes neither of them to the extreme, and the results are a significantly reduced capacitance, and a reduction in winding resistance.

4.2 Inverse Track-Width-Ratio

The proposed planar winding structure with inverse TWR is a way of designing multi-layer planar spiral windings in which the width of each track changes as it approaches the center of the winding. In one layer the widest conductor is on the outside of the spiral and in the next layer the widest conductor is in the center of the winding as illustrated in Fig. 4.4. For clarity, the spiral with the smaller inner turns will be referred to as the traditional layer, and the spiral with the wider inner turns will be referred as the inverted layer. The TWR (a) is a ratio of track widths which stays constant throughout the entire winding. In the traditional layer of Fig. 4.4 it is referenced to the outer turn, which is of width W, thus reducing the width of inner turns. This is different from the inverted layer, in which the inner turn is of width W and the outer turns reduce in width by the same ratio. The clearance (C_l) stays constant between each turn.

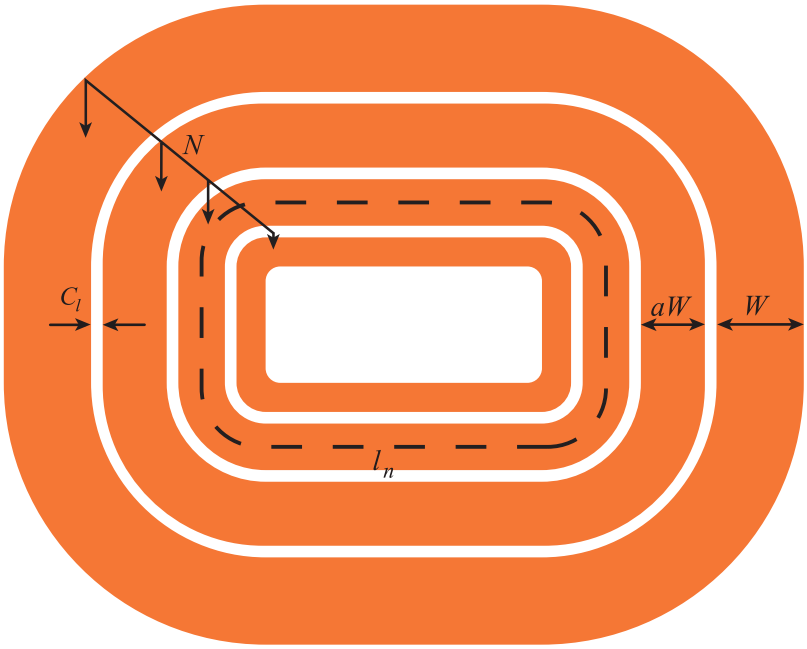

(a) Top Layer

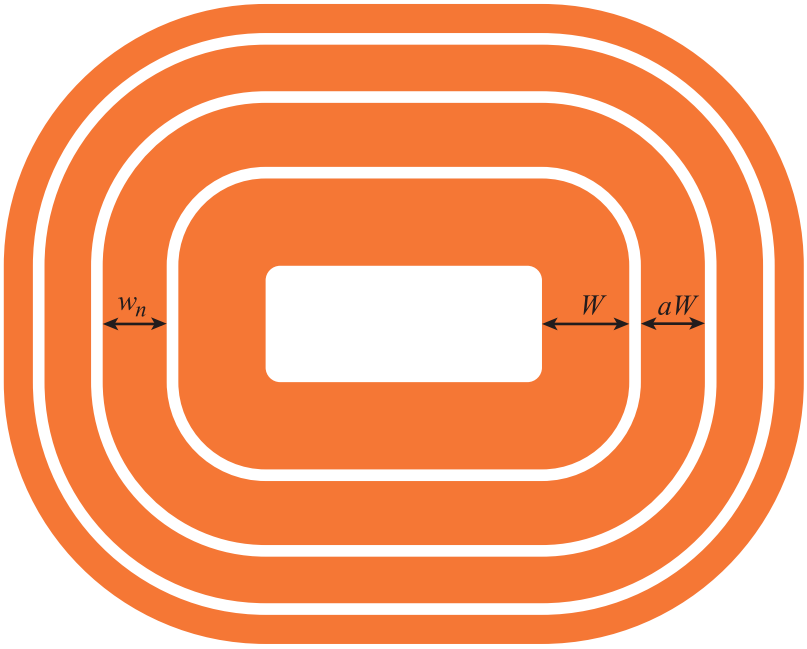

(b) Bottom Layer

Figure 4.4: Top view of the two layers of the proposed planar spiral winding with (a) traditional TWR and (b) inverse TWR.

4.2.1 Low-Frequency Resistance Modeling of the Inverse TWR Planar Spiral Winding

The planar spiral winding structure with inverse TWR has some slight changes when compared to the generalized racetrack planar spiral winding, so an improved resistance model has been derived. This model will be employed to model the voltage gradient in the spiral winding and used as an input to the finite element simulations in order to model the winding capacitance. This is achieved from calculating the resistance of each turn as a ratio of the total resistance of the winding. The resistance of each turn (R_n) is calculated by employing:

$$R_n = \frac{\rho l_n}{t w_n} \tag{4.3}$$

where w_n is a function of W, the widest turn width, which is defined in Chapter 2 as:

$$W = \frac{1-a}{1-a^N}(x_o - x_i - (N-1)C_l) \tag{4.4}$$

Then each winding width of the traditional layer follows as:

$$w_{n(trad)} = a^{N-n}W \tag{4.5}$$

and the inverted layers as:

$$w_{n(inv)} = a^{n-1}W \tag{4.6}$$

where n always starts from 1 at the innermost turn and extends to N at the outermost turn of the winding, whether it is a traditional or inverted layer. The length of each individual turn, l_n, is defined for any layer as:

$$l_n = 4(x_c + r_n(\frac{\pi}{2}) + y_c) \tag{4.7}$$

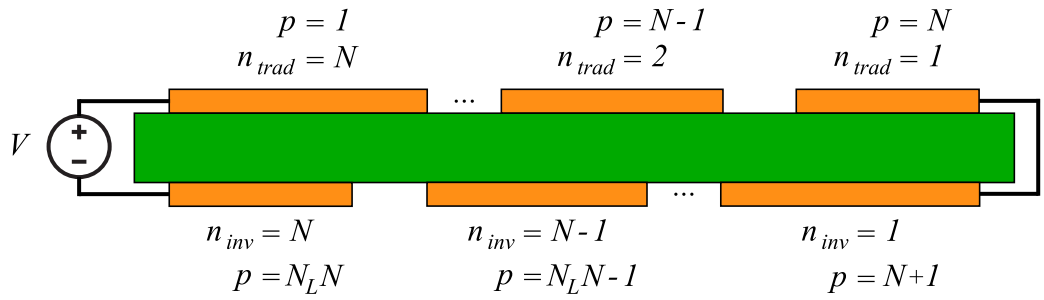

Figure 4.5: Cross-section of a planar spiral winding with the inverse TWR structure. Each layer has its turns, n_{trad} and n_{inv} extend from the interior to the exterior of the winding, each ranging from 1 to N, while p is defined from the turn of highest to lowest voltage, ranging from 1 to the product of the number of layers by the number of turns per layer, $N_L N$.

which is a function of the radius of each turn's corner, r_n, which now is different depending on which layer is being discussed. The radii of the traditionally defined layer turns ($r_{n(trad)}$) is given by:

$$r_{n(trad)} = x_i + (n-1)C_l + (x_o - x_i - (N-1)C_l)\left[\frac{a^{N-n}}{2} + \sum_{k=1}^{n-1} a^{N-k}\right] \tag{4.8}$$

while the radii of the inverted layers ($r_{n(inv)}$) is described as:

$$r_{n(inv)} = x_i + (n-1)C_l + (x_o - x_i - (N-1)C_l)\left[\frac{a^{n-1}}{2} + \sum_{k=1}^{n-1} a^{k}\right] \tag{4.9}$$

From that, the total resistance (R_{tot}) is:

$$R_{tot} = \sum_{m=1}^{N_L}\sum_{n=1}^{N} R_n \tag{4.10}$$

where N_L is the number of layers.

With this data, the turns can be iterated through in the order in which they are seen from the source (using p as the index as described in Fig. 4.5) and the voltage for each turn

(V_p) can be derived as:

$$V_p = \frac{V}{R_{tot}} \sum_{i=p}^{N_L N} R_i \tag{4.11}$$

where V is the input voltage. With this data, V_p for every turn can be used in 2-D Finite Element Analysis to find the overall capacitance of the proposed planar spiral winding with inverse TWR.

4.2.2 Inductance Modeling of the Inverse TWR Planar Spiral Winding

The inductance calculation for the inverse TWR planar spiral structure will follow the calculations from Chapter 2, which are duplicated here for clarity. The self inductance is calculated from:

$$L_{s_N}(\mu H) = \sum_{n=1}^{N} 0.002 l_n \left[log_e \left(\frac{2l_n}{t + a^{N-n}W} \right) + 0.50049 + \left(\frac{t + a^{N-n}W}{3l_n} \right) \right] \tag{4.12}$$

while the mutual inductances between straight section conductors is calculated through:

$$M_l(\mu H) = 2l \left[log_e \left\{ \frac{l}{GMD} + \left(1 + \frac{l^2}{GMD^2} \right)^{\frac{1}{2}} \right\} - \left(1 + \frac{GMD^2}{l^2} \right)^{\frac{1}{2}} + \frac{GMD}{l} \right] \tag{4.13}$$

or

$$M_{jk}(\mu H) = 0.001 (\frac{\sqrt{2}}{2}) l_j \left[log_e \frac{1 + \frac{l_k}{l_j} + \frac{l_{j+k}}{l_j}}{1 - \frac{l_k}{l_j} + \frac{l_{j+k}}{l_j}} + \frac{l_k}{l_j} log_e \frac{\frac{l_k}{l_j} + \frac{l_{j+k}}{l_j} + 1}{\frac{l_k}{l_j} + \frac{l_{j+k}}{l_j} - 1} \right] \tag{4.14}$$

based on their orientation. The self and mutual inductance components are summed through the use of Grover's algorithm as per the relation:

$$L_{T_N} = L_{s_N} + M_N \tag{4.15}$$

where:

$$M_N = 2\sum_{j \neq k} M_{jk} \tag{4.16}$$

The important dimensions in these calculation is the GMD which is approximated as the distance between the center of conductors. With these models the inductance of the inverse TWR planar spiral winding can be investigated.

4.2.3 Capacitance Simulation of the Inverse TWR Planar Spiral Winding

Capacitance is measured in FEA by applying a DC voltage to the winding and measuring the total capacitive energy developed (E_{tot}), through the relation presented in (4.2), and the energy density relationship:

$$E_{tot} = \frac{1}{2}\int_A \vec{D} \cdot \vec{E} dA \tag{4.17}$$

where V is the lumped voltage applied to the winding and A is the area where capacitive energy exists. Setting (4.2) equal to (4.17) and setting V to 1 V, the resultant capacitance is calculated from the FEA data by the equation:

$$C = \int_A \vec{D} \cdot \vec{E} dA \tag{4.18}$$

In order to simulate the correct amount of capacitive energy in a 2-D FEA model, the voltage of each turn is required, as it is distributed across the winding. These voltages were determined through the application of (4.10) and (4.11). Fig. 4.6 displays the capacitive energy density between a traditional planar spiral winding and the proposed winding structure. It can be seen that the proposed winding structure has a more even energy distribution due to the reduced surface area between turns with the highest voltage differential between them.

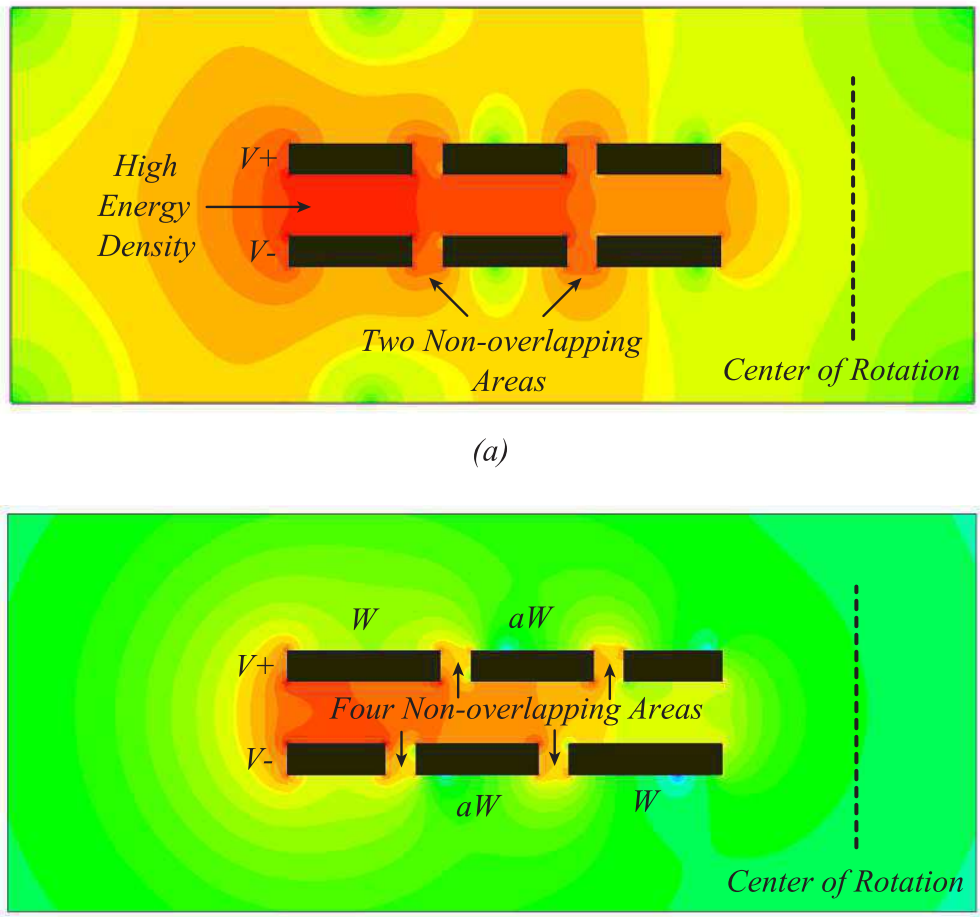

Figure 4.6: FEA capacitive energy cross-section of (a) a traditional planar spiral winding and (b) the proposed inverse TWR planar spiral winding. The traditional winding exhibits more overlapping conductor and an area of extremely high capacitive energy at the winding input terminals. The proposed winding provides double areas without overlap and much less energy trapped at the input terminal.

While the same total cross-sectional width of conductor is used in each case, a lot of the field is dissipated through the reduced overlap provided by the staggered clearances.

A series of planar spiral windings were simulated and calculated in order to observe the effect of changing TWR on the overall inductance, resistance, and capacitance of the spirals.

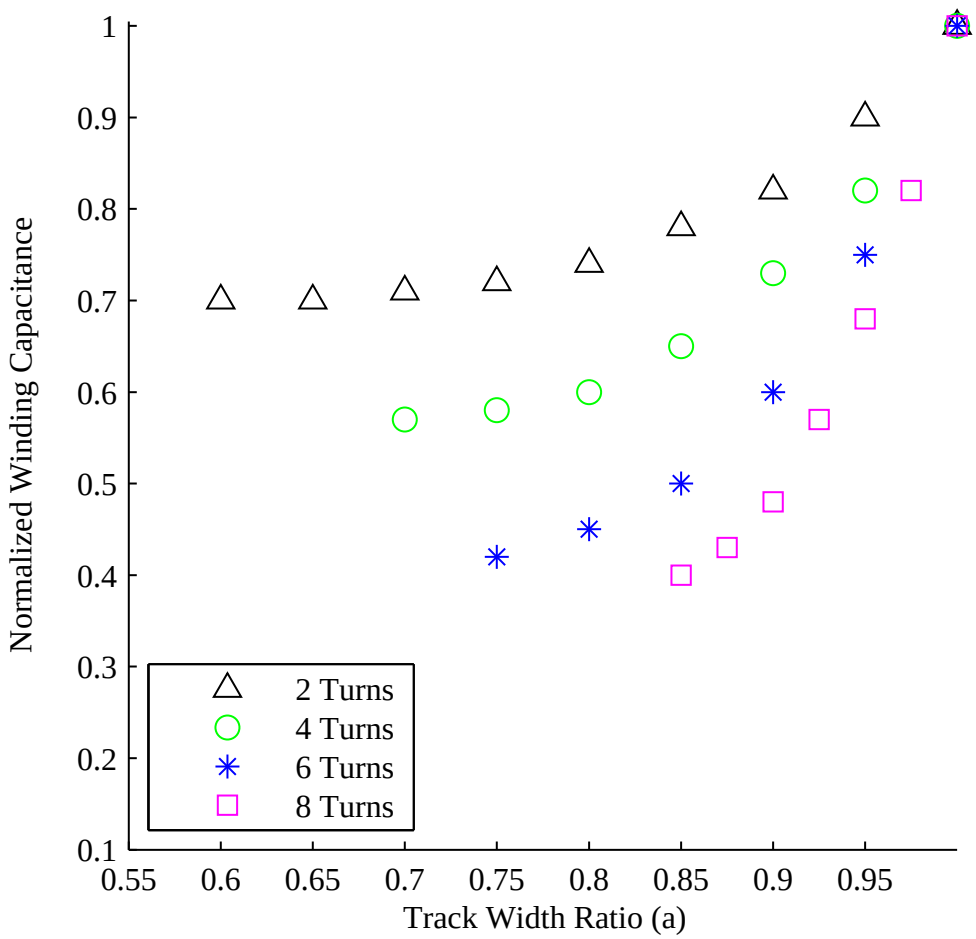

Figure 4.7: Normalized simulated winding capacitance in the proposed planar spiral winding with inverse TWR. Baseline parameters are included in Table 4.1.

Table 4.1: Simulated Winding Parameters

Factor	Value	Units
x_c, y_c	5,2	mm
r_i	1	mm
N_L	2	
N	2, 4, 6, 8	turns
r_o	15	mm
C_l	0.25	mm
t	0.105	mm
s	1.1	mm

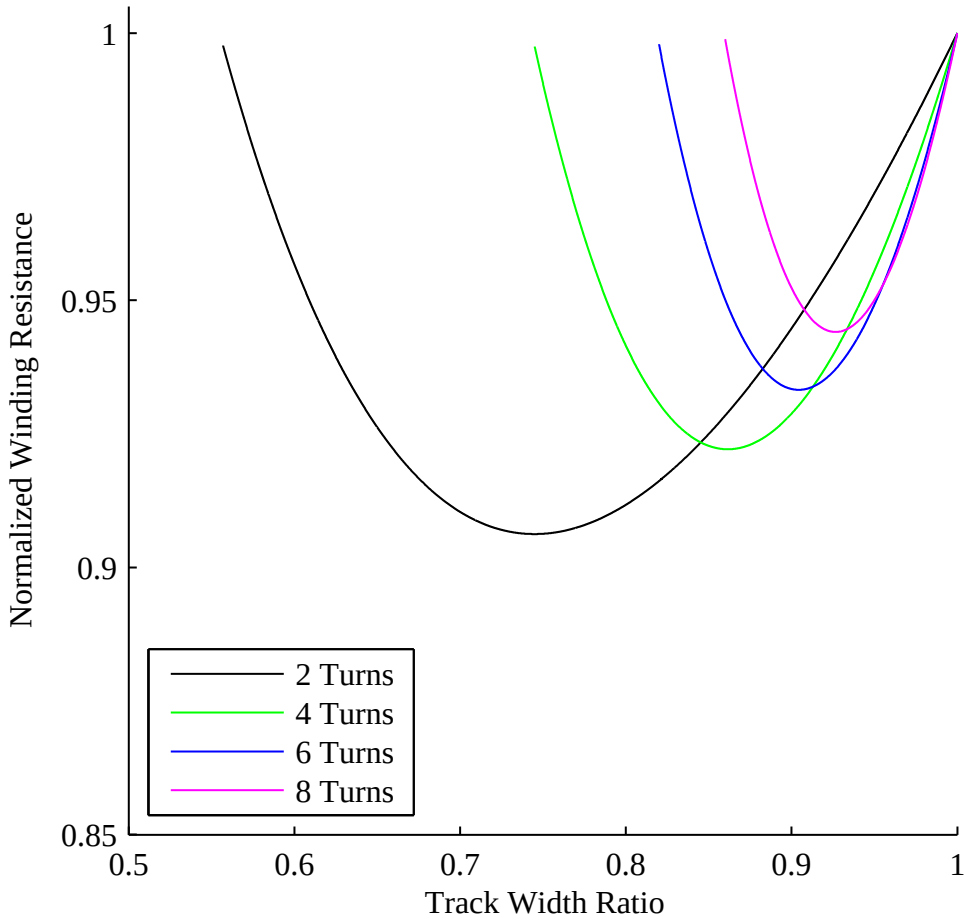

Figure 4.8: Analytical models of the DC resistance of the proposed planar spiral winding with inverse TWR based on (4.10). Baseline parameters indicated in Table 4.1.

The dimensions of the windings are contained in Table 4.1. Figs. 4.7, 4.8, and 4.9 display normalized capacitive, resistive and inductive results for 5 different 2-layer winding cases of changing number of turns. It can be observed that as TWR decreases, the capacitance rapidly falls and then stabilizes at a much lower value than the initial capacitance, while the resistance decreases to a minimum and then rebounds back as the TWR is further decreased. The inductance stays constant for the area of resistance decrease and then falls off rapidly once the capacitance settled at its expected value. In each case there is an optimal region where the capacitance is within 5% of its minimum value, the resistance is still below the

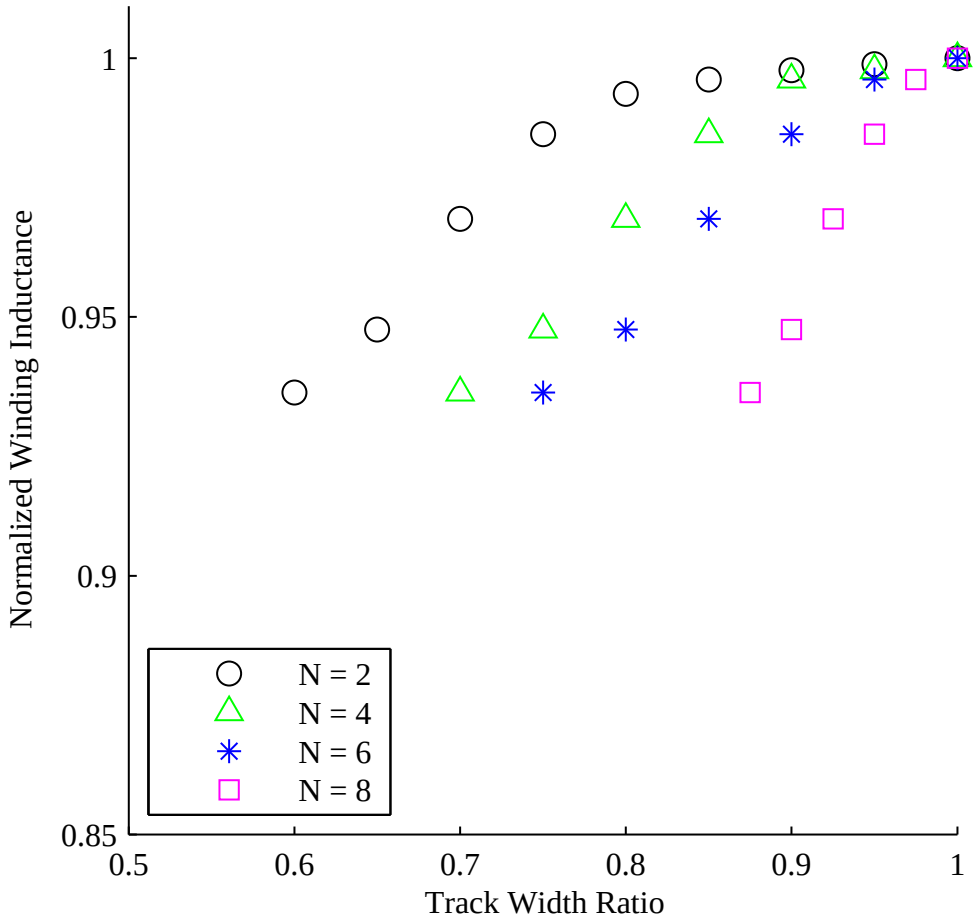

Figure 4.9: Normalized calculated inductance results of the proposed planar spiral winding with inverse TWR based on the analysis in Chapter 2. Baseline parameters indicated in Table 4.1.

initial case, and the inductance is within 1% of its nominal value. This is considered to be the optimal design point for applications in which the current density is roughly constant across the conductor surfaces.

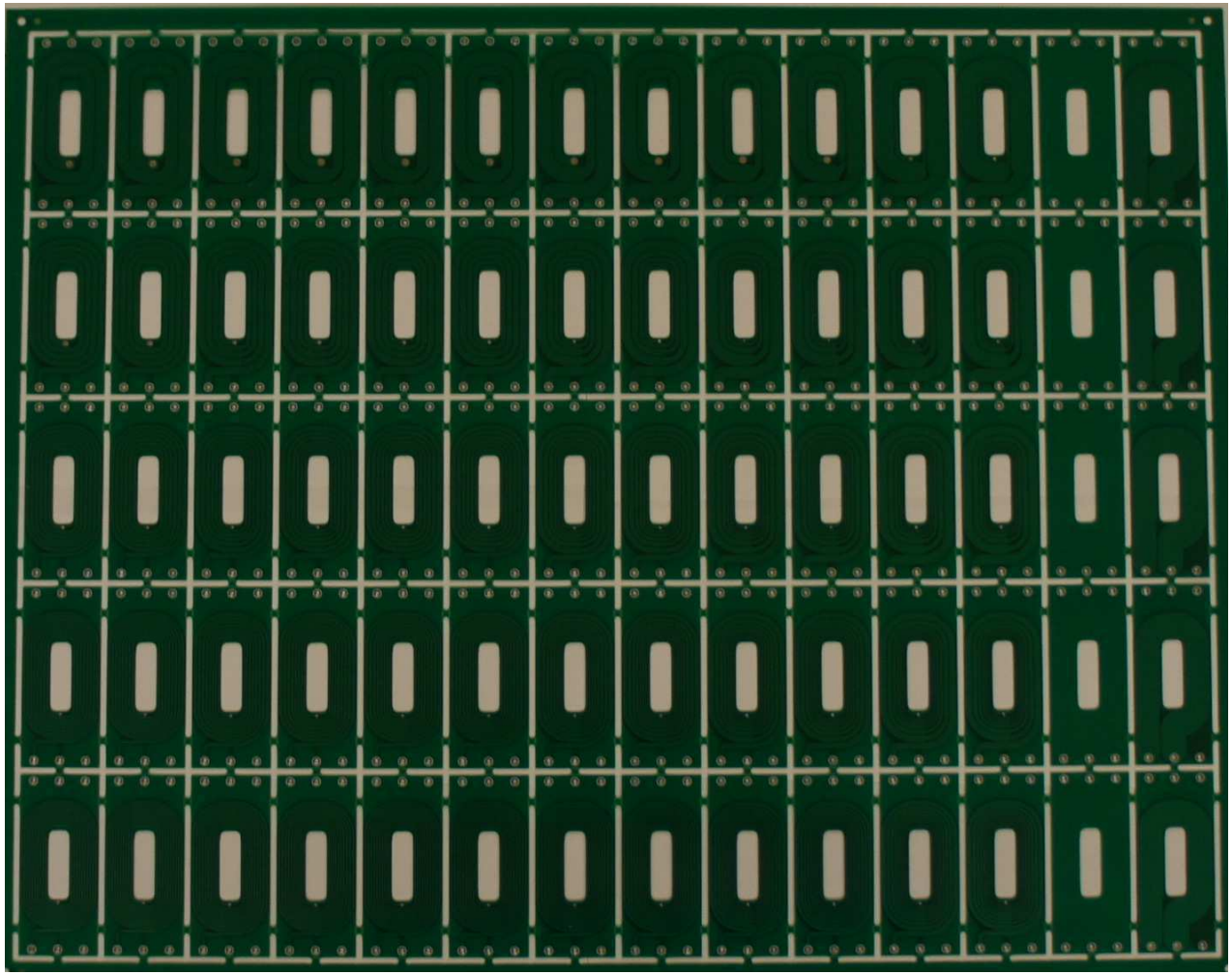

Figure 4.10: Subset of windings employed to test the accuracy of the proposed resistance and capacitance modeling of the inverse TWR planar spiral winding.

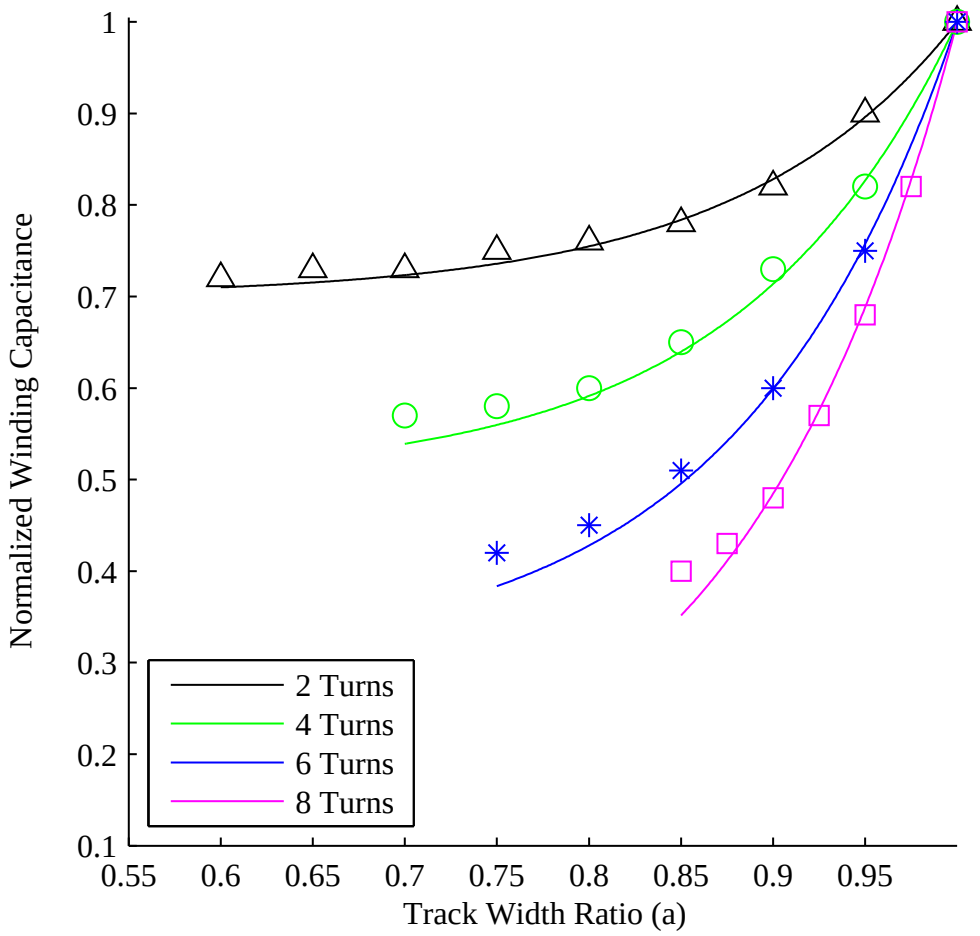

Figure 4.11: Experimental (discrete) vs. predicted (continuous) capacitance values for the inverse TWR planar spiral winding structure.

4.3 Experimental Validation

Multiple panels of planar spiral windings were manufactured in order to confirm the capacitive, resistive, and inductive behaviour and to observe the effect of the proposed technique when the frequency is changed. Fig. 4.10 presents a subset of the investigated windings. The capacitance and resistance of the planar spiral windings with dimensions presented in Table 4.1 were measured with an impedance analyzer, and the results are presented in Figs. 4.11, 4.12, and 4.13. The experimental data closely matched the predicted data, except

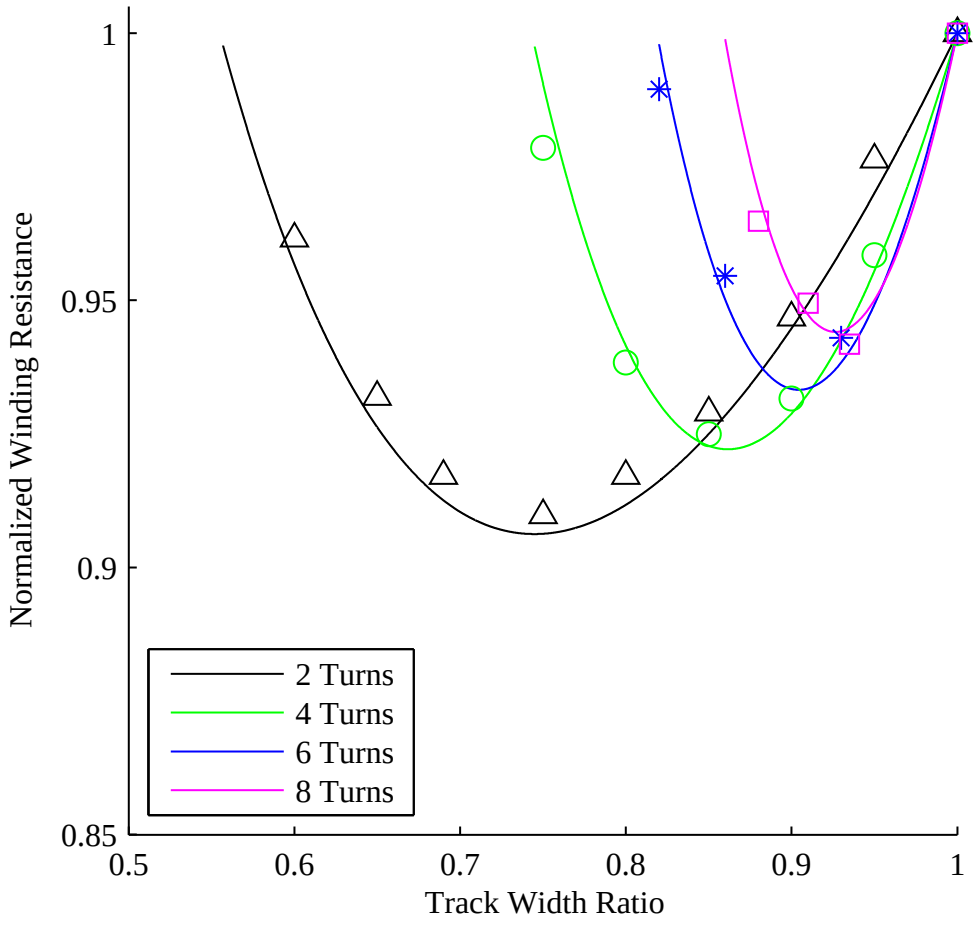

Figure 4.12: Experimental (discrete) vs. predicted (continuous) DC resistance values for the inverse TWR planar spiral winding structure.

for the small amount of capacitance in each case which comes from the overlap induced from connecting the turns, and any stray capacitance from the connections. The trends that can be observed are similar to the proposed models, where the capacitance tends towards an asymptotic value below the initial capacitance while the low frequency resistance drops a small amount and then increases rapidly after a minimum value is reached. The inductance remains constant and then drops off.

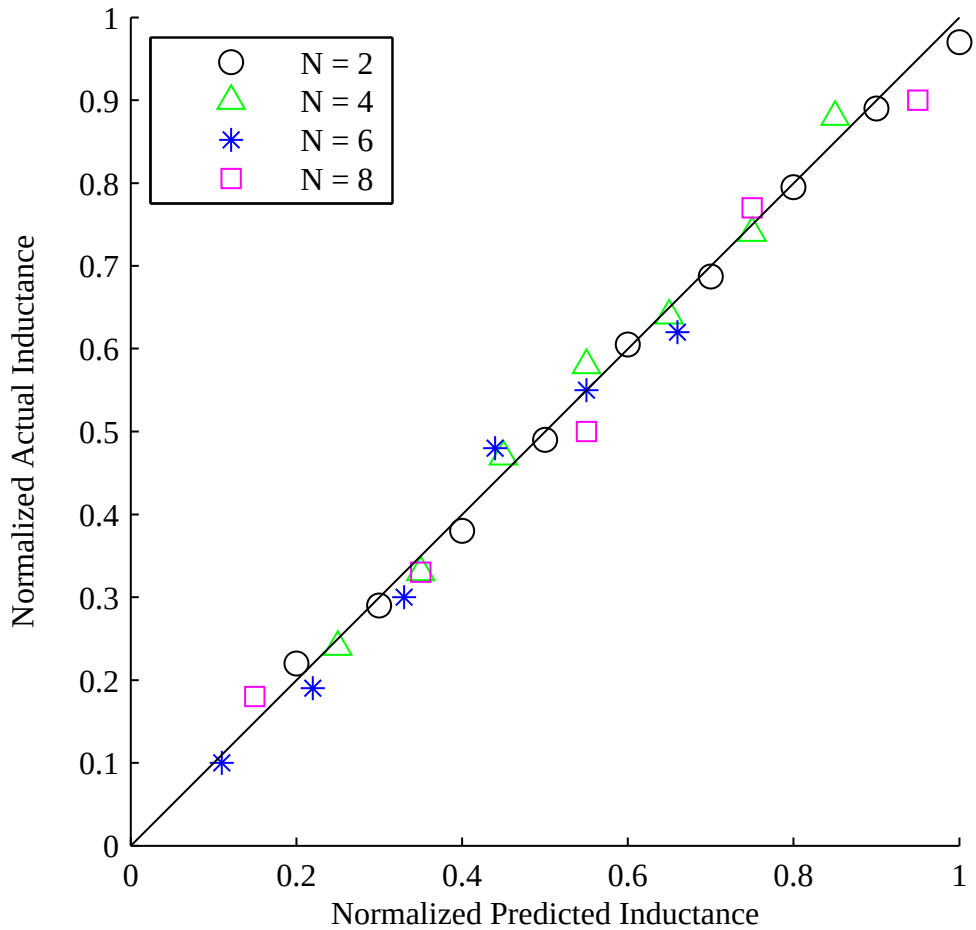

Figure 4.13: Normalized experimental vs. predicted inductance values for the inverse TWR planar spiral winding structure.

4.3.1 Experimental Performance Comparison

A comparative study was performed for a set of 8-turn windings in order to clarify the benefits of employing the proposed planar spiral winding structure with inverse TWR. Three winding cases are considered: the traditional equal-turn-width planar spiral winding, the planar spiral with no turns overlapping, and the proposed planar spiral winding with inverse TWR. An impedance analyzer is employed to measure the impedance (Z) from 500 kHz to 50 MHz in order to observe their inductance (L), capacitance (C), and self-resonant frequency (SRF).

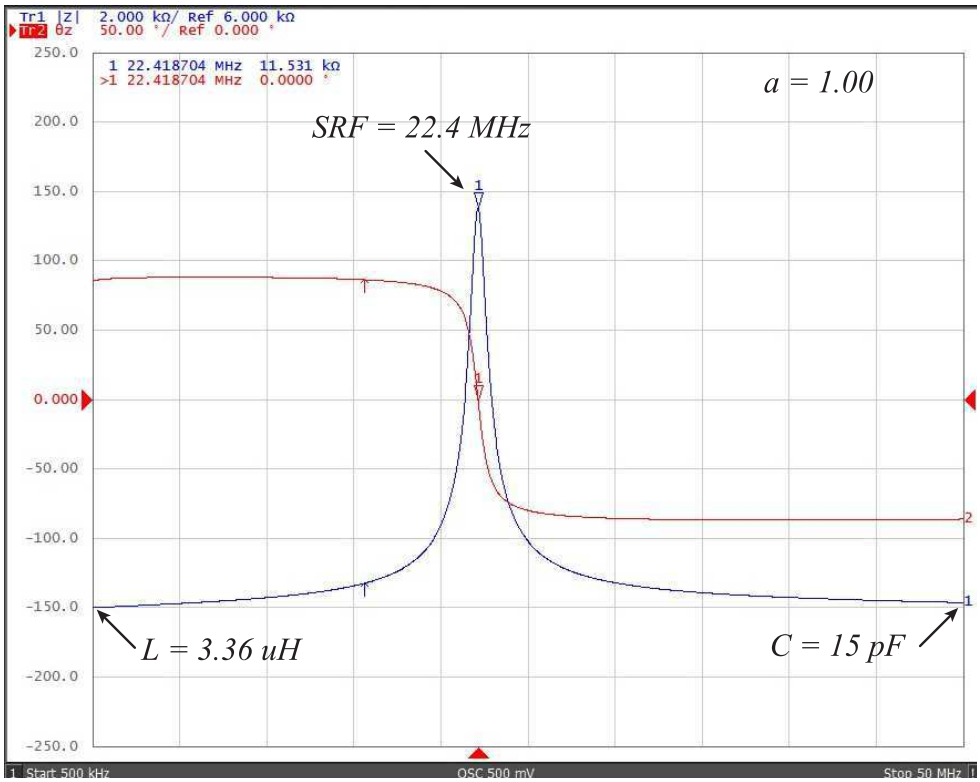

Figure 4.14: Impedance magnitude and angle vs. frequency of the standard planar spiral winding structure. The inductance is measured at low frequency by the rate of change of the impedance, while the capacitance is measured by the rate of change of impedance at high frequency. The SRF confirms the measurements.

The inductance is measured by observing the slope of the impedance at low frequency by the relationship:

$$Z = j\omega L \tag{4.19}$$

and the capacitance is measured by observing the slope of the impedance at high frequency by the relationship:

$$Z = \frac{-1}{j\omega C} \tag{4.20}$$

The values are confirmed through the measurement of the SRF, which is the point at

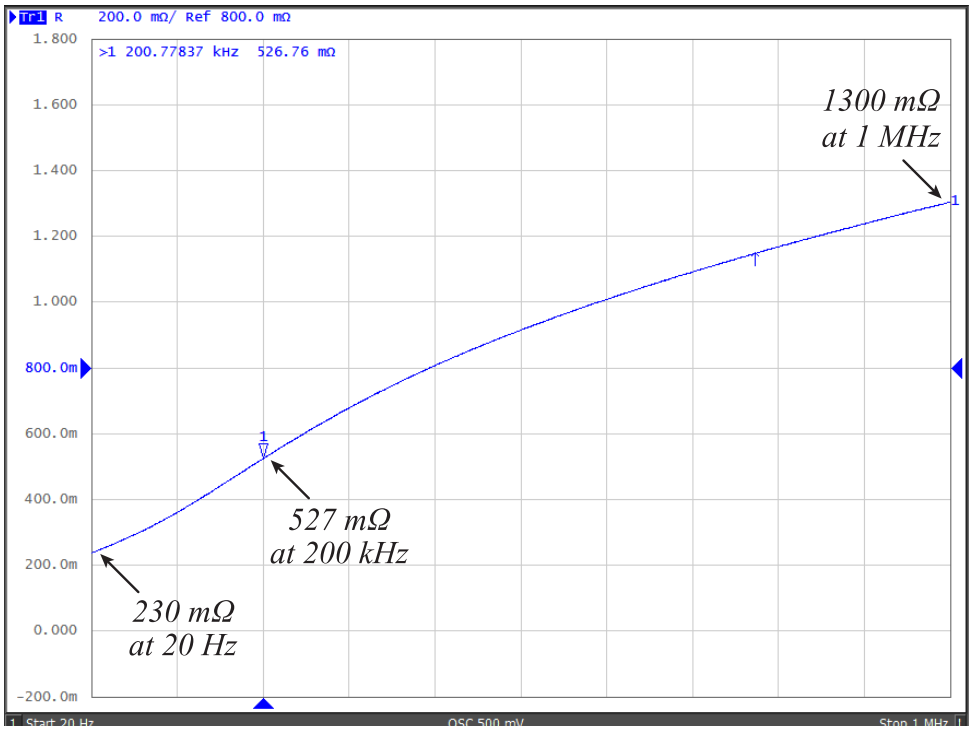

Figure 4.15: AC resistance of the standard planar spiral winding structure.

which the impedance angle is 0° by the relationship:

$$SRF = \frac{1}{2\pi\sqrt{LC}} \tag{4.21}$$

After the capacitance was determined, the resistance of the windings were measured within an operating range from 20 Hz to 1 MHz. The resistances at 20 Hz, 200 kHz, and 1 MHz were noted as comparison points between the three windings.

The impedance profile for the traditional planar spiral winding is presented in Fig. 4.14. In this case all turns are 1.5 mm wide and overlap fully, separated by 0.254 mm spacing. As is expected, this case is the worst case scenario. For a $3.36\mu H$ winding, it has an SRF of only 22.4 MHz, representing a capacitance of 15 pF. This capacitance reduces the working frequency range of the winding, and can cause current spikes when met with rapid changes in

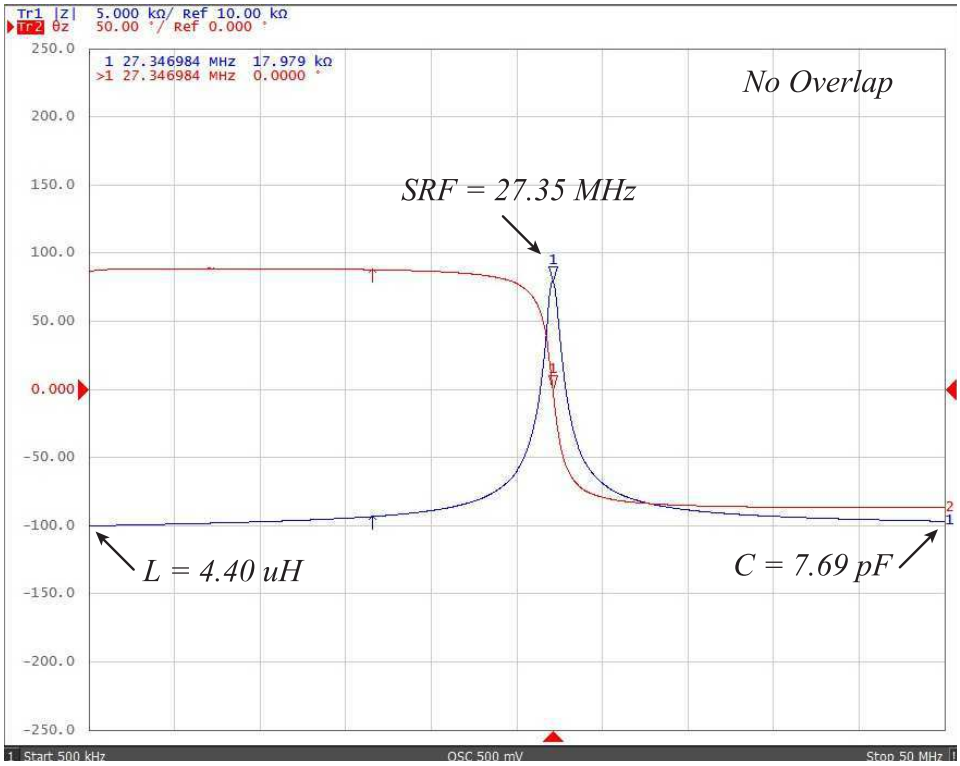

Figure 4.16: Impedance magnitude and angle vs. frequency of the planar spiral winding structure without overlapping conductors. The inductance is measured at low frequency by the rate of change of the impedance, while the capacitance is measured by the rate of change of impedance at high frequency. The SRF confirms the measurements.

voltage, which are characteristic of switch-mode power supplies. The resistive characteristics of the winding are presented in Fig. 4.15. This resistance profile is the standard by which the two options are compared, with 230 $m\Omega$ at 20 Hz, 527 $m\Omega$ at 200 kHz, and 1.3 Ω at 1 MHz.

Employing the same footprint as the traditional case, an 8-turn planar spiral winding with no overlap between turns was manufactured and tested. These turns were only 0.875 mm wide, with 0.875 mm spacing, so the low frequency resistance is predicted to be much higher, while the capacitance should be much lower. The impedance plot for this winding is presented in Fig. 4.16. The SRF has increased, as expected, but only to 27.4 MHz due to a 30%

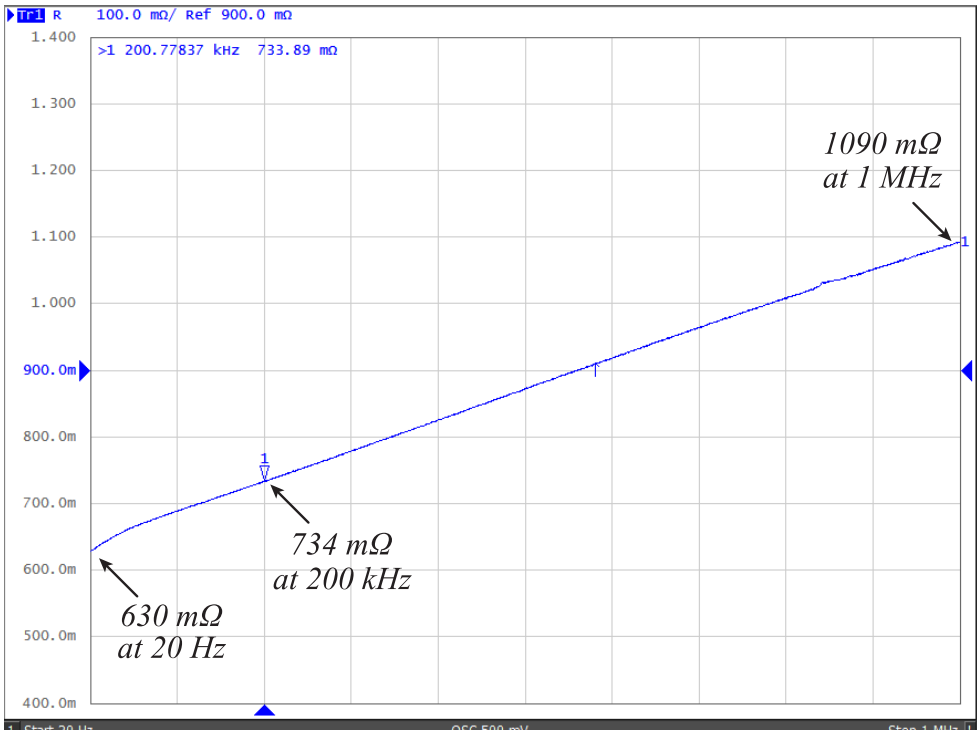

Figure 4.17: AC resistance for the planar spiral winding structure without overlapping conductors.

increase in inductance. The inductive performance of this technique is problematic in many applications, especially resonant techniques in which it will heavily impact the operating frequency. The capacitive performance, though, is exceptional, with a 48% decrease. Some of the remnant capacitance can be attributed to connections between turns, and stray electric field between layers. The resistive profile of this winding is contained in Fig. 4.17. As expected, the low frequency resistive performance is much worse than the traditional case, with an increase of 275% near DC. This performance gets better as the frequency increases though, with only a 40% increase in resistance at 200 kHz and a 16% decrease in resistance at 1 MHz. This improved response at higher frequency can be attributed to the decrease in proximity effect losses due to spacing between conductors. If the increase in inductance can fit within the design specifications, this technique is applicable in some frequencies where the

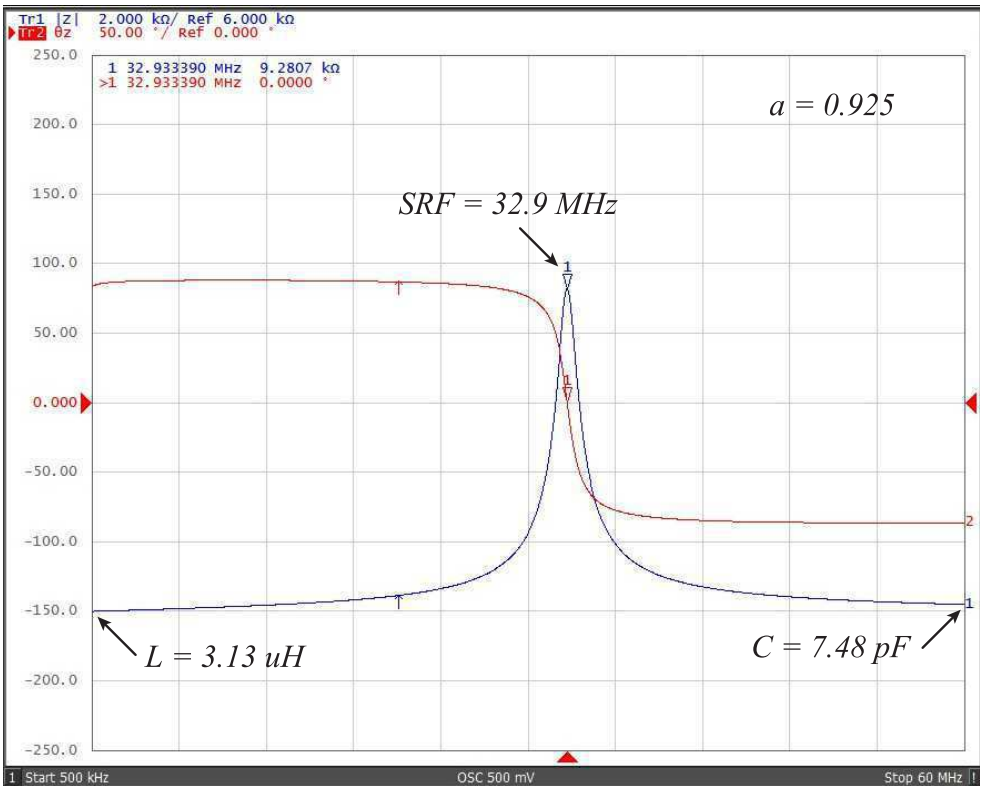

Figure 4.18: Impedance magnitude and angle vs. frequency of the proposed inverse TWR planar winding structure with $a = 0.925$. The inductance is measured at low frequency by the rate of change of the impedance, while the capacitance is measured by the rate of change of impedance at high frequency. The SRF confirms the measurements.

proximity effect is a dominant issue.

The final option for capacitance reduction is the proposed planar spiral winding structure with inverse TWR. The design of this winding is based upon the performance observed in Figs. 4.12 and 4.11. The chosen TWR is $a = 0.925$ as that is where the resistance is the lowest, and is at an adequate reduction in capacitance to compete with the non-overlapping case, roughly 50% of the traditional capacitance. The resulting impedance plot for this winding is included in Fig. 4.18, demonstrating an increase in the SRF to 32.9 MHz, the highest frequency of the 3 tested windings. In addition, the inductance of the winding is only 3.13 μH, within 4% of the traditional planar spiral winding. The capacitance reduced

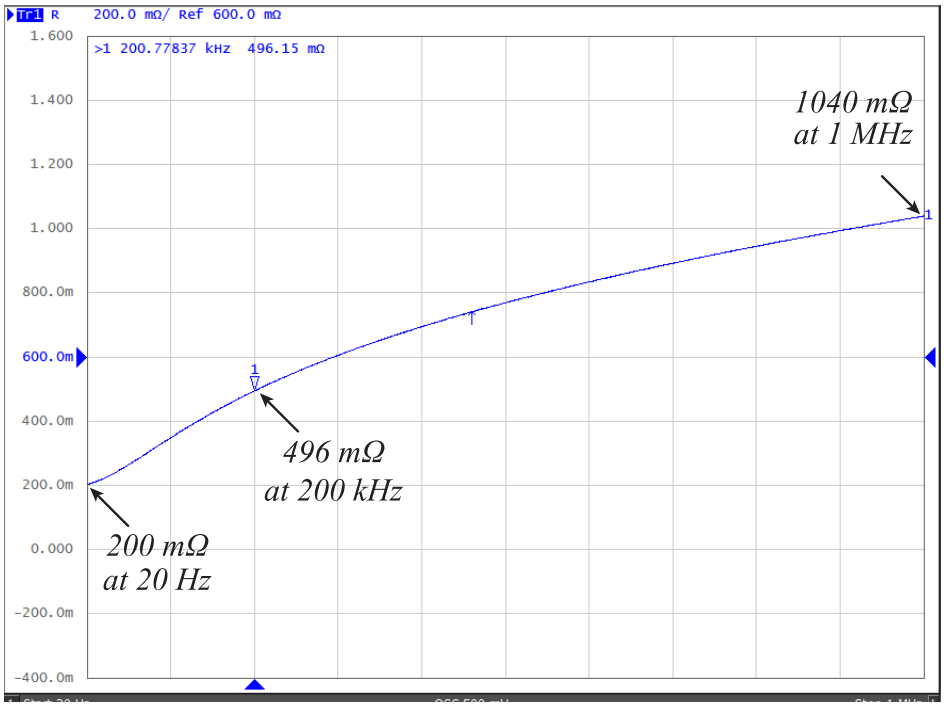

Figure 4.19: AC resistance of the proposed inverse TWR planar winding structure with $a = 0.925$.

by over 50%, down to 7.48 pF. While the capacitance reduction is similar to the winding with removed turns, the applications of this technique are more varied, due to its ability to maintain inductance. The resistive trend for this winding is included in Fig. 4.19. At 20Hz the resistance decreased by 7%, at 200 kHz the decrease is also 7%, but by 1 MHz, the decrease as spread to a 20% reduction in resistance. This performance is better than the case of removed turns at every frequency within the predicted operating range. The added benefit of this technique is that the TWR can be tuned to optimize behaviour at any operating frequency based on the technique proposed in Chapter 3. There are no degrees of freedom, beyond changing the footprint which can improve the technique of removing overlap.

4.4 Summary

This chapter introduced the planar spiral winding with inverse Track-Width-Ratio as a means of improving the capacitance in planar spiral windings. By changing track widths such that the traditional layer had wider turns on the outside of the spiral and the inverted layer had wider turns on the inside of the spiral, the inverse TWR structure increased the amount of non-overlapping copper and reduced the area in the outside of the winding where the highest amount capacitive energy is stored. The analytical model for low frequency resistance from Chapter 2 was modified and included in a model for the voltage of every turn. The inductance model from Chapter 2 confirmed the inductance does not change substantially within the desired design space of the inverse TWR structure. The resistance model was used in finite element simulations to confirm the decrease in capacitance and resistance experienced by employing this technique. It was found that there is an optimal region where TWR can be chosen to decrease resistance to a minimum, the capacitance will be significantly reduced, and the inductance will be largely unchanged.

The capacitance models were then confirmed through experimental measurements, and then a comparative example was performed to highlight the benefits of the proposed technique. Three windings were compared: the traditional planar spiral winding with equal turn widths, the planar spiral winding with no overlapping copper, and a planar spiral winding with inverse TWR that had been optimized for low frequency operation. It was found that the non-overlapping winding decreased the capacitance by 48% but increased the inductance by 30% and the low frequency resistance by 275%. This became better at 1 MHz when a reduction in resistance by 16% was observed. The proposed inverse TWR winding structure reduced the capacitance by over 50% while lowering the resistance by 6% at low frequency up to 20% at 1 MHz. Finally, the inductance was kept within 4% of the traditional case.

Chapter 5

Conclusions

5.1 Conclusions and Contributions

This dissertation explored three important aspects of the use of a Track-Width-Ratio (TWR) within concentric planar spiral winding design: low frequency resistance reduction and inductance prediction, high frequency quality factor improvement, and capacitance reduction. The generalized racetrack planar spiral winding was introduced and was accompanied by a unified dimensional system which could specify the dimensions of a variety of popular winding shapes:

- Circular
- Rectangular
- Octagonal
- Traditional Racetrack

5.1.1 Low Frequency Resistance and Inductance

In Chapter 2, the self and mutual inductances for the generalized racetrack planar spiral winding were modeled based on the work of Greenhouse and Grover. Many panels of planar spiral windings of varying shapes and sizes were employed in simulations and experimental measurements in order to confirm their accuracy. In all cases, the inductance trends suggested

that the inductance of a planar spiral winding decreases exponentially as TWR decreases from unity, and that this decay is more distinct in windings with more turns. In addition, a model for the low-frequency resistance of the generalized racetrack planar spiral winding was developed analytically as a summation of the length-to-width ratio of each turn of the winding. Applying TWR to spiral windings from previous work emphasized its capabilities to reduce low frequency resistance. The resistance trends observed with the use of TWR involved a parabolic decrease in resistance until a minimum is reached, followed by a parabolic increase in resistance as TWR is decreased further. The derivative of the model was found in order to predict the TWR of the lowest resistance.

A design example followed, which demonstrated how to find the best TWR to be employed to maximize the performance of a planar spiral winding. This performance was measured by the ratio of the inductance to the resistance, $\frac{L}{R}$. The design example highlighted that there is a maximum for this ratio, and that it diverges from the case of minimum resistance. The optimized design winding had a TWR of 0.85 and improved $\frac{L}{R}$ by 18%.

5.1.2 High Frequency Resistance and Quality Factor

Chapter 3 introduced the hollow spiral winding with Track-Width-Ratio (TWR) as a technique to improve the Quality Factor (Q) of planar spiral windings at high frequencies. The proposed winding structure involved a two-factor interaction between extending the internal radius of the planar spiral winding in order to make it hollow, and then to apply TWR in order to decrease the width of internal turns of the winding. By doing so, the effects of skin and proximity effect were significantly reduced, improving the overall performance of the planar spiral windings.

This work applied a quadratic approximation of the effect of TWR on high frequency resistance based on normalized finite element simulation data. In order to remove finite element simulations from the model, a design area was chosen and a statistical Design of

Experiments approach was employed to create meta-models of the resistance values. Similar meta-models were created for the inductance, employing the models from Chapter 2. This investigation confirmed that the increase in internal radius can increase the overall inductance of the winding, while TWR can decrease it. This allowed for combinations of these factors to be employed to tune the inductance, rather than decrease inductance as was observed when turns were removed.

From the investigated windings, a specific design example was performed in order to maximize the Q of a circular planar spiral winding for application in a Wireless Power Transfer (WPT) system. The proposed technique was able to improve Q by 100% while tracking a constant inductance. The same winding footprint was employed to study the effect of removing inner turns, which resulted in a 20% reduction in inductance and only a 50% increase in Q. Removing turns fails to have a second degree of freedom to tune the inductance without changing the footprint of the winding. The proposed hollow planar spiral winding with TWR was tested dynamically and compared to the traditional planar spiral winding and the winding with turns removed in a 5 W, 110-200 kHz WPT system. At the rated load, the traditional planar spiral winding had a transmission efficiency of 70%, the winding with removed turns had a transmission efficiency of 80%, while the proposed hollow planar spiral winding with TWR had a transmission efficiency of 90%.

5.1.3 Capacitance Minimization

Chapter 4 introduced the planar spiral winding with inverse TWR as a technique to reduce the parasitic capacitance in planar spiral windings. By changing track widths such that the traditional layer had wider turns on the outside of the spiral and the inverted layer had wider turns on the inside of the spiral, the inverse TWR structure increased the amount of non-overlapping copper and reduced the area of the highest voltage differential between layers, where the highest amount of capacitive energy is stored. A low-frequency voltage

model for each turn was developed in order to simulate the capacitive energy distribution in the proposed structure. This model was used in finite element simulations to confirm the decrease in capacitance and resistance experienced by employing this technique. It was found that there is a TWR-range where the resistance reduces to a minimum and the capacitance will be significantly reduced.

The capacitance models were then confirmed through experimental measurements, and then a comparative example was performed to highlight the benefits of the proposed technique. Three windings were compared: the traditional planar spiral winding with equal turn widths, the planar spiral winding with no overlapping copper, and a planar spiral winding with inverse TWR that had been optimized for low frequency operation. It was found that the non-overlapping winding decreased the capacitance by 48% but increased the inductance by 30% and the low frequency resistance by 275%. This became better at 1 MHz when a reduction in resistance by 16% was observed. The proposed winding structure reduced the capacitance by over 50% while lowering the resistance by 6% at low frequency up to 20% at 1 MHz. Finally, the inductance was kept within 4% of the traditional case.

The concepts introduced in all chapters of this work were thoroughly tested with finite element simulations and experimental measurements employing a high-frequency LCR meter, a high-precision Frequency Response Analyzer, and a high-resolution oscilloscope.

5.1.4 Specific Academic Contributions

The work on low-frequency inductance and resistance modeling culminated in the following publications:

- S. R. Cove, M. Ordonez, "Practical inductance calculation for planar magnetics with track-width-ratio," in *Energy Conversion Congress and Exposition (ECCE)*, 2013, pp. 3733–3737.

- S. R. Cove, M. Ordonez, "Wireless-power-transfer planar spiral winding design applying track width ratio," *IEEE Trans. Ind. Appl.*, vol. 51, no. 3, pp. 2423–2433, May 2015.

These works cover the inductance and resistance prediction, and include a design example which employs the meta-model for high-frequency resistance presented in Chapter 3.

The following publication introduced the hollow planar spiral winding technique and covered the high frequency resistance model, presented the spiral winding design technique, and included the WPT design example:

- S. R. Cove, M. Ordonez, N. Shafiei, J. Zhu, "Improving Wireless Power Transfer Efficiency Using Hollow Windings with Track-Width-Ratio," *IEEE Trans. Power Electron.*, vol. 31, no. 9, pp. 6524–6533, Sept. 2016.

The following publication introduced the inverse TWR structure for capacitance reduction in planar spiral windings:

- S. R. Cove and M. Ordonez, "Low-Capacitance Planar Spiral Windings Employing Inverse Track-Width-Ratio", accepted for publication in *IEEE Energy Conversion Congress and Expo. (ECCE)*, 2016.

In addition to the body of work described above, foundational and complementary work was published which investigated Track-Width-Ratio and Design of Experiments methodology for planar transformers in LLC resonant converters:

- S. R. Cove, M. Ordonez, F. Luchino, J. Quaicoe, "Applying Response Surface Methodology to Small Planar Transformer Winding Design," *IEEE Trans. Ind. Electron.*, vol. 60, no. 2, pp. 483–493, Feb. 2013.

- S. R. Cove, M. Ordonez, F. Luchino, J. Quaicoe, "Integrated magnetic design of small planar transformers for LLC resonant converters," in *Energy Conversion Congress and Exposition* (ECCE), 2011, pp. 1839–1844.

- S. R. Cove, M. Ordonez, F. Luchino, J. Quaicoe, "Applying Response Surface Methodology to planar transformer winding design," in *Energy Conversion Congress and Exposition* (ECCE), 2010 IEEE, 2010, pp. 2182–2187.

Some publications resulted from collaborative research around magnetic design for planar inductors and transformers:

- N. Shafiei, M. Ordonez, S. R. Cove, M. Craciun, C. Botting, "Accurate modeling and design of LLC resonant converter with planar transformers," in *Energy Conversion Congress and Exposition (ECCE), 2015*, pp. 5468–5473.

- J. M. Galvez, M. Ordonez, S. R. Cove, J. Quaicoe, "Accurate modeling and design of LLC resonant converter with planar transformers," in *Canadian Conference on Electrical and Computer Engineering, 2012*, pp. 1–4.

5.2 Future Work

This work opens up many full areas of research which can build upon its findings. Some of the main areas in which multiple Masters and PhD students could be supervised include:

- Investigating the effects of a non-constant ratio of turns: While a constant ratio is easy and convenient for fabrication and design, there is no guarantee that it is the optimal design for every application. The effects of ratios which change quadratically, or exponentially will be investigated to observe the effects on parasitic elements.

- Application of the work in Wireless Power Transfer: While the windings investigated in this work have been proven to be beneficial for low-power Wireless Power Transfer applications, a large investment will be needed to design windings which can work for applications such as electric vehicle battery charging. A 3-D Wireless Power Transfer testbed is currently being developed to provide the necessary conditions to thoroughly test a high-power WPT setup with planar spiral windings employing TWR.

- Investigating the effect of adding a magnetic core: This work investigated coreless windings and focused on the effect of winding design exclusively. The next step in this regard is to add a magnetic core and investigate TWR along with core geometry, core thickness, airgap length, and see if it has a significant impact on parasitic elements and performance. This work would open a wide-range of sub-topics, including applications in resonant power conversion, renewable energy power conversion systems, and high-voltage MOSFET drivers.

- Thermal testing: when presenting track-width changes, the full load current has to pass through the smallest traces. The thermal conditions presented by the smaller tracks has yet to be thoroughly examined and modeled, as it is not clear to what extent the temperature will be impacted. A full thermal model is required with extensive testing in order to define the limits on the technique in terms of the smallest trace possible for a particular load current.

Bibliography

[1] S. R. Cove, "Design methodology for the control of planar transformer parasitics," Master's thesis, Memorial University (MUN), 2011.

[2] S. Cove and M. Ordonez, "Practical inductance calculation for planar magnetics with track-width-ratio," in *Energy Conversion Congress and Exposition (ECCE), 2013 IEEE*, 2013, pp. 3733–3737.

[3] ——, "Wireless-power-transfer planar spiral winding design applying track width ratio," *IEEE Trans. Ind. Appl.*, vol. 51, no. 3, pp. 2423–2433, 2015.

[4] S. Cove, M. Ordonez, N. Shafiei, and J. Zhu, "Improving wireless power transfer efficiency using hollow windings with track-width-ratio," *IEEE Trans. Power Electron.*, to be published, early Access.

[5] S. R. Cove and M. Ordonez, "Low-capacitance planar spiral windings employing inverse track-width-ratio," in *IEEE Energy Conversion Congress and Expo (ECCE)*, 2016, accepted for publication.

[6] E. de Jong, E. de Jong, B. Ferreira, and P. Bauer, "Toward the next level of PCB usage in power electronic converters," *IEEE Trans. Power Electron.*, vol. 23, no. 6, pp. 3151–3163, 2008.

[7] Z. Ouyang, G. Sen, O. Thomsen, and M. Andersen, "Analysis and design of fully in-

tegrated planar magnetics for primary–parallel isolated boost converter," *IEEE Trans. Ind. Electron.*, vol. 60, no. 2, pp. 494–508, 2013.

[8] Z. Ouyang, Z. Zhang, O. Thomsen, and M. Andersen, "Planar-integrated magnetics (pim) module in hybrid bidirectional DC–DC converter for fuel cell application," *IEEE Trans. Power Electron.*, vol. 26, no. 11, pp. 3254–3264, 2011.

[9] P. Shamsi and B. Fahimi, "Design and development of very high frequency resonant DC–DC boost converters," *IEEE Trans. Power Electron.*, vol. 27, no. 8, pp. 3725–3733, 2012.

[10] T. Andersen, C. Zingerli, F. Krismer, J. Kolar, N. Wang, and C. Mathuna, "Modeling and pareto optimization of microfabricated inductors for power supply on chip," *IEEE Trans. Power Electron.*, vol. 28, no. 9, pp. 4422–4430, 2013.

[11] C. Mathúna, N. Wang, S. Kulkarni, and S. Roy, "Review of integrated magnetics for power supply on chip (pwrsoc)," *IEEE Trans. Power Electron.*, vol. 27, no. 11, pp. 4799–4816, 2012.

[12] F. Waldron, R. Foley, J. Slowey, A. Alderman, B. Narveson, and S. Mathuna, "Technology roadmapping for power supply in package (psip) and power supply on chip (pwrsoc)," *IEEE Trans. Power Electron.*, vol. 28, no. 9, pp. 4137–4145, 2013.

[13] B. Choi, J. Nho, H. Cha, T. Ahn, and B. Choi, "Design and implementation of low-profile contactless battery charger using planar printed circuit board windings as energy transfer device," *IEEE Trans. Ind. Electron.*, vol. 51, no. 1, pp. 140–147, 2004.

[14] P. Meyer, P. Germano, M. Markovic, and Y. Perriard, "Design of a contactless energy-transfer system for desktop peripherals," *IEEE Trans. Ind. Appl.*, vol. 47, no. 4, pp. 1643–1651, 2011.

[15] H. Matsumoto, Y. Neba, K. Ishizaka, and R. Itoh, "Model for a three-phase contactless power transfer system," *IEEE Trans. Power Electron.*, vol. 26, no. 9, pp. 2676–2687, 2011.

[16] ——, "Comparison of characteristics on planar contactless power transfer systems," *IEEE Trans. Power Electron.*, vol. 27, no. 6, pp. 2980–2993, 2012.

[17] J. Acero, C. Carretero, I. Lope, R. Alonso, O. Lucia, and J. Burdio, "Analysis of the mutual inductance of planar-lumped inductive power transfer systems," *IEEE Trans. Ind. Electron.*, vol. 60, no. 1, pp. 410–420, 2013.

[18] W. Zhong, X. Liu, and S. Hui, "A novel single-layer winding array and receiver coil structure for contactless battery charging systems with free-positioning and localized charging features," *IEEE Trans. Ind. Electron.*, vol. 58, no. 9, pp. 4136–4144, 2011.

[19] H.-L. Tu, I.-S. Chen, P.-C. Yeh, and H.-K. Chiou, "High performance spiral inductor on deep-trench-mesh silicon substrate," *IEEE Microw. Wireless Compon. Lett.*, vol. 16, no. 12, pp. 654–656, 2006.

[20] Z. Zhang and X. Liao, "Micromachined GaAs MMIC-based spiral inductors with metal shores and patterned ground shields," *IEEE Sensors J.*, vol. 12, no. 6, pp. 1853–1860, 2012.

[21] S. Cheon, M. Yoon, H. Park, and J. Park, "Robust and postless air-suspended high q integrated inductors on silicon," *IEEE Trans. Magn.*, vol. 48, no. 11, pp. 4131–4134, 2012.

[22] G. Gautier, M. Capelle, J. Billoue, F. Cayrel, and P. Poveda, "RF planar inductor electrical performances on n-type porous 4H silicon carbide," *IEEE Electron Device Lett.*, vol. 33, no. 4, pp. 477–479, 2012.

[23] F. W. Grover, *Inductance Calculations*, V. Nostrand, Ed. Dover Publications, 1962.

[24] H. A. Wheeler, "Simple inductance formulas for radio coils," *Proceedings of the Institute of Radio Engineers*, vol. 16, no. 10, pp. 1398–1400, Oct. 1928.

[25] A. Olivei, "Optimized miniature thin-film planar inductors, compatible with integrated circuits," *Materials and Packaging IEEE Transactions on Parts*, vol. 5, no. 2, pp. 71–88, Jun. 1969.

[26] H. G. Dill, "Designing inductors for thin-film applications," *Electronic Design*, 1964.

[27] H. E. Bryan, "Printed inductors and capacitors," *Tele-Tech & Electronic Industries*, p. 68, 1955.

[28] F. E. Terman, *Radio Engineering Handbook*. McGraw-Hill, 1943.

[29] H. Greenhouse, "Design of planar rectangular microelectronic inductors," *IEEE Transactions on Parts, Hybrids, and Packaging*, vol. 10, no. 2, pp. 101–109, 1974.

[30] S. S. Mohan, M. del Mar Hershenson, S. P. Boyd, and T. H. Lee, "Simple accurate expressions for planar spiral inductances," *IEEE Journal of Solid-State Circuits*, vol. 34, no. 10, pp. 1419–1424, Oct. 1999.

[31] W. G. Hurley and M. C. Duffy, "Calculation of self and mutual impedances in planar magnetic structures," *IEEE Transactions on Magnetics*, vol. 31, no. 4, pp. 2416–2422, Jul. 1995.

[32] ——, "Calculation of self- and mutual impedances in planar sandwich inductors," *IEEE Transactions on Magnetics*, vol. 33, no. 3, pp. 2282–2290, May 1997.

[33] W. G. Hurley, M. C. Duffy, S. O'Reilly, and S. C. O'Mathuna, "Impedance formulas

for planar magnetic structures with spiral windings," *IEEE Transactions on Industrial Electronics*, vol. 46, no. 2, pp. 271–278, Apr. 1999.

[34] W. G. Hurley, M. C. Duffy, J. Zhang, I. Lope, B. Kunz, and W. H. Wölfle, "A unified approach to the calculation of self- and mutual-inductance for coaxial coils in air," *IEEE Transactions on Power Electronics*, vol. 30, no. 11, pp. 6155–6162, Nov. 2015.

[35] P. Dowell, "Effects of eddy currents in transformer windings," *Proceedings of the Institution of Electrical Engineers*, vol. 113, no. 8, pp. 1387–1394, 1966.

[36] N. Kutkut, "A simple technique to evaluate winding losses including two-dimensional edge effects," *IEEE Trans. Power Electron.*, vol. 13, no. 5, pp. 950–958, 1998.

[37] T. Demeester and D. De Zutter, "Internal impedance of composite conductors with arbitrary cross section," *IEEE Trans. Electromagn. Compat.*, vol. 51, no. 1, pp. 101–107, 2009.

[38] I. Lope, C. Carretero, J. Acero, R. Alonso, and J. Burdio, "AC power losses model for planar windings with rectangular cross-sectional conductors," *IEEE Trans. Power Electron.*, vol. 29, no. 1, pp. 23–28, 2014.

[39] J. Craninckx and M. Steyaert, "A 1.8-GHz low-phase-noise CMOS VCO using optimized hollow spiral inductors," *IEEE J. Solid-State Circuits*, vol. 32, no. 5, pp. 736–744, 1997.

[40] Y. Su, X. Liu, C. K. Lee, and S. Hui, "On the relationship of quality factor and hollow winding structure of coreless printed spiral winding (CPSW) inductor," *IEEE Trans. Power Electron.*, vol. 27, no. 6, pp. 3050–3056, 2012.

[41] X. Huang, K. Ngo, and G. Bloom, "Design techniques for planar windings with low resistances," in *Applied Power Electronics Conference and Exposition, 1995. APEC '95. Conference Proceedings 1995., Tenth Annual*, no. 0, 1995, pp. 533–539.

[42] H.-M. Hsu and C.-W. Tseng, "Design of on-chip transformer with various coil widths to achieve minimal metal resistance," *IEEE Electron Device Lett.*, vol. 28, no. 11, pp. 1029–1032, 2007.

[43] S. Cove, M. Ordonez, F. Luchino, and J. Quaicoe, "Applying response surface methodology to small planar transformer winding design," *IEEE Trans. Ind. Electron.*, vol. 60, no. 2, pp. 483–493, 2013.

[44] H.-M. Hsu, "Analytical formula for inductance of metal of various widths in spiral inductors," *IEEE Trans. Electron Devices*, vol. 51, no. 8, pp. 1343–1346, 2004.

[45] J. Lopez-Villegas, J. Samitier, C. Cane, P. Losantos, and J. Bausells, "Improvement of the quality factor of RF integrated inductors by layout optimization," *IEEE Trans. Microw. Theory Tech.*, vol. 48, no. 1, pp. 76–83, 2000.

[46] J. Sallan, J. Villa, A. Llombart, and J. Sanz, "Optimal design of ICpt systems applied to electric vehicle battery charge," *IEEE Trans. Ind. Electron.*, vol. 56, no. 6, pp. 2140–2149, 2009.

[47] D. Kurschner, C. Rathge, and U. Jumar, "Design methodology for high efficient inductive power transfer systems with high coil positioning flexibility," *IEEE Trans. Ind. Electron.*, vol. 60, no. 1, pp. 372–381, 2013.

[48] D. Ahn and S. Hong, "A study on magnetic field repeater in wireless power transfer," *IEEE Trans. Ind. Electron.*, vol. 60, no. 1, pp. 360–371, 2013.

[49] W. Zhong, C. K. Lee, and S. Hui, "General analysis on the use of tesla's resonators in domino forms for wireless power transfer," *IEEE Trans. Ind. Electron.*, vol. 60, no. 1, pp. 261–270, 2013.

[50] D. Ahn and S. Hong, "Wireless power transmission with self-regulated output voltage for biomedical implant," *IEEE Trans. Ind. Electron.*, vol. 61, no. 5, pp. 2225–2235, 2014.

[51] A. Zaheer, G. Covic, and D. Kacprzak, "A bipolar pad in a 10-kHz 300-W distributed IPt system for agv applications," *IEEE Trans. Ind. Electron.*, vol. 61, no. 7, pp. 3288–3301, 2014.

[52] Z. Ouyang and M. Andersen, "Overview of planar magnetic technology—fundamental properties," *IEEE Trans. Power Electron.*, vol. 29, no. 9, pp. 4888–4900, 2014.

[53] P. Chan, C. Lee, and S. Hui, "Stray capacitance calculation of coreless planar transformers including fringing effects," *Electronics Letters*, vol. 43, no. 23, 2007.

[54] Z. Ouyang, O. Thomsen, and M. Andersen, "Optimal design and tradeoff analysis of planar transformer in high-power DC–DC converters," *IEEE Trans. Ind. Electron.*, vol. 59, no. 7, pp. 2800–2810, 2012.

[55] J. Lu and F. Dawson, "Characterizations of high frequency planar transformer with a novel comb-shaped shield," *IEEE Trans. Magn.*, vol. 47, no. 10, pp. 4493–4496, 2011.

[56] C. Lee, Y. Su, and S. Hui, "Printed spiral winding inductor with wide frequency bandwidth," *IEEE Trans. Power Electron.*, vol. 26, no. 10, pp. 2936–2945, 2011.

[57] M. Pahlevaninezhad, P. Das, J. Drobnik, P. Jain, A. Bakhshai, and G. Moschopoulos, "A novel winding layout strategy for planar transformer applicable to high frequency high power DC-dc converters," in *Energy Conversion Congress and Exposition (ECCE), 2011 IEEE*, 2011, pp. 3786–3791.

[58] M. Pahlevaninezhad, D. Hamza, and P. Jain, "An improved layout strategy for common-mode EMI suppression applicable to high-frequency planar transformers in high-power

DC/dc converters used for electric vehicles," *IEEE Trans. Power Electron.*, vol. 29, no. 3, pp. 1211–1228, 2014.

[59] R. Rong, D. A. Lowther, Z. Malik, H. Su, J. Nelder, and R. Spence, "Applying response surface methodology in the design and optimization of electromagnetic devices," *IEEE Transactions on Magnetics*, vol. 33, no. 2, pp. 1916–1919, Mar. 1997.

[60] D. K. Hong, K.-C. Lee, B. C. Woo, and D.-H. Koo, "Optimum design of electromagnet in magnetic levitation system for contactless delivery application using response surface methodology," in *Electrical Machines, 2008. ICEM 2008. 18th International Conference on*, Sep. 2008, pp. 1–6.

[61] H. G. Cheon, D. S. Kwag, J. H. Choi, C. H. Min, T. S. Park, H. H. Kim, and S. H. Kim, "Insulation design and experimental results for transmission class hts transformer with composite winding," *IEEE Transactions on Applied Superconductivity*, vol. 18, no. 2, pp. 648–651, Jun. 2008.

[62] D. C. Montgomery, *Design and Analysis of Experiments*. John Wiley and Sons, 2001.

[63] R. Chen, J. D. van Wyk, S. Wang, and W. G. Odendaal, "Improving the characteristics of integrated EMI filters by embedded conductive layers," *IEEE Transactions on Power Electronics*, vol. 20, no. 3, pp. 611–619, May 2005.

[64] H. J. Kim, Y. J. Kim, and J. R. Kim, "An integrated LTCC inductor embedding nizn ferrite," *IEEE Transactions on Magnetics*, vol. 42, no. 10, pp. 2840–2842, Oct. 2006.

[65] Unauthored, "System description: Wireless power transfer," Wireless Power Consortium, Tech. Rep., 2013.